SAPIENZA
UNIVERSITÀ DI ROMA

MULTICHANNEL PASSIVE RADAR SYSTEMS:
SIGNAL PROCESSING TECHNIQUES AND DESIGN STRATEGIES

by

Francesca FILIPPINI

A thesis submitted in partial fulfilment of the requirements for the
Degree of Doctor of Philosophy
in Information and Communications Technologies
Curriculum in Radar and Remote Sensing

Sapienza University of Rome

February 2020

Thesis Supervisor

Prof. Fabiola Colone
Department of Information Engineering,
Electronics and Telecommunication

This thesis was evaluated by the two following external referees:

Maria Sabrina Greco, Professor, University of Pisa, Italy
Hugh Griffiths, Professor, University College London, United Kingdom

The time and effort of the external referees in evaluating this thesis,
as well as their valuable and constructive suggestions,
are very much appreciated and greatly acknowledged.

A mia sorella Monica

Abstract

Passive Coherent Location (PCL) system is one of the most rapidly developing technology in the radar field and significant progress has been made in recent years. However, some aspects that are not under the control of the radar designer still prevent PCL technology from reaching its point of maturity. The goal of this thesis is to address this issue by resorting to the exploitation of information diversity conveyed by multiple receiving channels.

The main novelties that this research has led to can be identified in two main areas, one concerning the exploitation of polarization diversity for target detection, the other regarding the exploitation of spatial and frequency diversity for target localization purposes. Although the ideas underlying the main achievements reported in this work arise from the need to overcome PCL systems limitations, the research performed to reach this goal has led to achievements that have a broad scope of application, not limited to passive radar systems, which increases the scientific value of this work.

In the first part of this thesis, we deal with the problem of target detection in coherent radar systems exploiting **polarimetric diversity**. We build upon the demonstrated benefits that a suitable use of signals collected by differently polarized antennas can lead to, and we present a new polarimetric adaptive target detection scheme. To this aim, we resort to a parametric approach and we model the disturbance affecting the data as a multi-channel AR process. First, we show the effectiveness of the proposed strategy via an extensive simulated analysis, then we carry out a performance assessment under spectral model mismatch conditions, and finally we demonstrate its validity against real data, collected by both active and passive radar systems.

In the second part of this thesis, we address the problem of target direction of arrival (DoA) estimation in systems that jointly exploit **spatial and frequency diversity**. We derive a reliable performance characterization of a multi-carrier maximum likelihood DoA estimator in the threshold region. The capability of predicting the performance of the considered estimator in low signal-to-noise ratio scenarios is a powerful tool that can also be used to select the best performing receiving system layout, given a number of constraints. The experimental results obtained using configurations selected according to this criterion show that a suitable exploitation of spatial and frequency diversity allows to both extend the angular sector where the target DoA can be unambiguously estimated and improve the estimation accuracy.

Acknowledgment

First and foremost, I would like to express my sincere gratitude to my mentor and guide Prof. Fabiola Colone, for sharing her immense knowledge with me, for her unwavering support and encouragement over this entire journey. The enthusiasm she has for research was contagious and motivational for me and I am grateful for having worked with her during these years.

My special thanks to the entire RRSN research group at Sapienza, for creating the most pleasant working environment. Thanks for the fun time we spent together, for the stimulating discussions, for the moral support before the deadlines, for the sleepless nights spent practicing and for the loads of laughs.

A huge thank you to my friends, for always being there for me during the good and the bad. You mean everything to me.

Thank you, Jorge for all the love, support, understanding and endless patience.

A special thanks to my family. Mom and dad, you are the most outstanding inspiration to me. Words cannot express how grateful I am to you for the unfailing faith, support, and love you have provided me with throughout my entire life.

To my sister, who left me too soon facing this scary world alone.
This dissertation, as my whole life, is dedicated to you.

The following papers were published as a result of this PhD research

Journal Papers

J1. **Filippini F.**, Colone F., Cristallini D. and Bournaka G., "Experimental results of polarimetric detection schemes for DVB-T-based passive radar," in *IET Radar, Sonar & Navigation*, vol. 11, no. 6, pp. 883-891, 6 2017.

J2. **Filippini F.**, Colone F. and De Maio A., "Threshold Region Performance of Multi-Carrier Maximum Likelihood Direction of Arrival Estimator," in *IEEE Transactions on Aerospace and Electronic Systems*, vol. 55, no. 6, pp. 3517-3530, 2019.

J3. Colone F. and **Filippini F.**, "Auto-Regressive model based polarimetric adaptive detection scheme. Part I: Theoretical derivation and performance analysis," submitted to *IEEE Transactions on Aerospace and Electronic Systems*, August 2019.

J4. Colone F. and **Filippini F.**, "Auto-Regressive model based polarimetric adaptive detection scheme. Part II: Performance assessment under spectral model mismatch," submitted to *IEEE Transactions on Aerospace and Electronic Systems*, August 2019.

Conference Papers

C1. **Filippini F.**, Colone F., Cristallini D. and Bournaka G., "Preliminary experimental results of polarimetric detection schemes for DVB-T based passive radar," *2017 IEEE Radar Conference (RadarConf)*, Seattle, WA, 2017, pp. 0383-0388.

C2. **Filippini F.** and Colone F., "A practical approach to polarimetric adaptive target detection in passive radar," *International Conference on Radar Systems (Radar 2017)*, Belfast, 2017, pp. 1-6.

C3. Martelli T., **Filippini F.**, Pignol F., Colone F. and Cardinali R., "Computationally effective range migration compensation in PCL systems for maritime surveillance," *2018 IEEE Radar Conference (RadarConf18)*, Oklahoma City, OK, 2018, pp. 1406-1411.

C4. **Filippini F.**, Martelli T., Colone F. and Cardinali R., "Target DoA estimation in passive radar using non-uniform linear arrays and multiple frequency channels," *2018 IEEE Radar Conference (RadarConf18)*, Oklahoma City, OK, 2018, pp. 1290-1295.

C5. **Filippini F.**, Martelli T., Colone F. and Cardinali R., "Exploiting long coherent integration times in DVB-T based passive radar systems," *2019 IEEE Radar Conference (RadarConf)*, Boston, MA, USA, 2019, pp. 1-6.

C6. **Filippini F.** and Colone F., "Polarimetric detection scheme for passive radar based on a 2D Auto-Regressive disturbance model," *International Radar Conference (RADAR2019)*, Toulon, 2019

C7. Martelli T., **Filippini F.** and Colone F., " Tackling the different target dynamics issues in counter drone operations using passive radar", accepted to *IEEE 2020 International Radar Conference*, Washington DC, USA, 2020

C8. Cabrera O., Bongioanni C., **Filippini F.**, Sarabakha O., Colone F. and Lombardo P., "Detecting drones and human beings with DVB-S based COTS passive radar for short-range surveillance," accepted to *IEEE 2020 International Radar Conference*, Washington DC, USA, 2020

Honours and Awards

Some results of this PhD research have been awarded of the following recognitions:

2019 Best Paper Award at *2019 International Radar Conference (RADAR 2019),* Toulon, France, for paper C6.

2018 Premium Award for Best Paper in *IET Radar, Sonar & Navigation*, for paper J1.

2018 Second Best Student Paper Award at *2018 IEEE Radar Conference (RadarConf18),* Oklahoma City, OK, US for paper C4.

2017 Best Paper Award at *2017 GTTI Italian Workshop on Radar and Remote Sensing*, for paper "Exploiting polarimetric diversity in passive radar: recent advances and applications, by Filippini F. and Colone F.

Contents

List of Figures ..... **ix**

List of Tables ..... **xii**

Nomenclature ..... **xiii**

List of Acronyms ..... **xv**

1 Introduction **1**

1.1 Background 1
1.1.1 Passive Coherent Location systems principles 1
1.1.2 Basic PCL processing 3
1.1.3 Motivation 4
1.2 Goal of the Thesis and Innovative Contributions 5
1.2.1 Exploitation of polarization diversity for target detection 5
1.2.2 Exploitation of spatial and frequency diversity for target localization 6
1.3 Outline of the Thesis 7

Part I Exploitation of polarization diversity for target detection **9**

2 Locally adaptive polarimetric target detection **10**

2.1 Background and Motivation 10
2.2 Multi-polarimetric DVB-T based PCL signal processing 11
2.3 Polarimetric detection schemes 12
2.3.1 Polarimetric Non-Coherent Integration 13
2.3.2 Polarimetric locally adaptive Generalized Likelihood Ratio Test 14
2.4 Experimental validation against DVB-T based PCL data 15
2.4.1 Acquisition campaign 15
2.4.1.1 DVB-T based passive radar setup 16
2.4.1.2 Adopted methodology 17
2.4.2 Results 19
2.4.2.1 Results obtained without disturbance cancellation at each channel 19

2.4.2.2 Results obtained after disturbance cancellation at each channel 22
2.5 Summary 25

3 Polarimetric adaptive target detector based on a multi-channel AR model: Derivation and Performance Analysis 27

3.1 Fully adaptive polarimetric detectors 27
3.2 AR model based Polarimetric Adaptive Detector 30
3.2.1 Multi-channel Auto-regressive Model 30
3.2.2 AR model based Polarimetric Matched Filter 32
3.2.3 Adaptive implementation 34
3.3 Asymptotic Performance 35
3.3.1 False alarm probability 36
3.3.2 Detection Probability 36
3.4 Numerical Results 38
3.5 Summary 47

4 Polarimetric adaptive target detector based on a multi-channel AR model: Performance Assessment under Mismatched Spectral Model 49

4.1 Theoretical asymptotic performance under disturbance model mismatch 49
4.1.1 False alarm probability 51
4.1.2 Detection probability 53
4.2 Asymptotic performance analysis against simulated data 54
4.3 Modified AR model based Polarimetric Adaptive Matched Filter 60
4.4 Numerical Results 63
4.5 Summary 68

5 Polarimetric adaptive target detector based on a multi-channel AR model: Experimental Validation 69

5.1 Performance assessment against real active radar data 69
5.2 Performance assessment against real PCL data 73
5.2.1 Acquisition campaign 76
5.2.2 Results 77
5.3 Sub-optimal Modified Polarimetric AR based AMF 80
5.3.1 Results 81
5.4 Summary 84

Part II Exploitation of frequency and spatial diversity for target localization 85

6 Target DoA estimation exploiting spatial and frequency diversity: Threshold region performance characterization 86

6.1 Background and Motivation 86
6.2 Signal model and Multi-Carrier ML DoA estimator 88
6.3 Approximation of the MSE and probability of outlier 90
6.4 Evaluation of the Pairwise Error Probabilities under CMA 93
6.4.1 Theoretical Derivation 93
6.4.2 Simulation Results 96
6.5 Evaluation of the Pairwise Error Probabilities under UMA 100
6.5.1 Theoretical Derivation 100
6.5.2 Simulation Results 103
6.6 Simulation Results: MSE Approximation 103
6.7 Summary 107

7 Target DoA estimation exploiting spatial and frequency diversity: Experimental Validation 109

7.1 Multi-frequency ML DoA estimation for DVB-T based PCL system 109
7.2 Acquisition campaigns and adopted methodology 111
7.3 Experimental Results 114
7.3.1 Test campaign #1: Aircraft surveillance 114
7.3.2 Test campaign #2: Drone surveillance 117
7.4 Summary 120

8 Conclusion and future work 121

8.1 Results and novelties 121
8.2 Future Outlook 123

Appendices 125

Appendix A Derivation of the AR model based polarimetric detector 126
Appendix B ML Parameter Estimation for Pol-AR-AMF 127
Appendix C PDF of **z0** under the H_0 hypothesis 129
Appendix D Derivation of the asymptotic Pol-AR-AMF Pd for fluctuating target 131
Appendix E Approximation of the asymptotic Pol-AR-AMF Pd for non-fluctuating target 134

Bibliography 136

List of Figures

Figure 1.1: Sketch of the PCL geometry 2
Figure 1.2: Sketch of the basic PCL processing scheme 4
Figure 2.1: Sketch of the acquisition geometry 15
Figure 2.2: Sketch of PARASOL system: (a) Antenna unit (b) Data and signal processing unit 17
Figure 2.3: Cooperative targets: (a) Delphin aircraft (b) One of the speedboats 17
Figure 2.4: Detection results without applying any cancellation stage for $Pfa = 10^{-6}$ and different detection schemes : (a) single-pol H, (b) single-pol V (c) P- NCI (d) P-GLRT 20
Figure 2.5: Detection results, after applying a 2-stage ECA-CD algorithm for $Pfa = 10^{-6}$ and dfferent detection schemes: (a) single-pol H, (b) single-pol V (c) P- NCI (d) P-GLRT 22
Figure 2.6: Range-velocity maps for single-pol H before thresholding: (a) without a 2-stage ECA-CD (b) after a 2-stage ECA-CD 24
Figure 2.7: Correct detections in the bistatic velocity-time domain for $Pfa = 10^{-6}$ with: (a) single-pol H after a 2-stages ECA-CD (b) single-pol V after a 2-stages ECA-CD (c) P-GLRT without any prior cancellation stage, (d) P-GLRT after a 2-stages ECA-CD 25
Figure 3.1: Power spectra of a L-channel $AR(3)$ process 39
Figure 3.2: Actual Pfa versus P when $Pfa = 10^{-3}$ for (a) different polarimetric channels and (b) different pulses 40
Figure 3.3: Pd versus SCR for $M = 32$, Swerling 0 target model and different polarimetric channels: (a) $L = 1$ (HH), (b) $L = 3$ (HH, VV, HV) 41
Figure 3.4: Pd versus SCR for $M = 32$, Swerling I target model and different polarimetric channels: (a) $L = 1$ (HH), (b) $L = 3$ (HH, VV, HV) 42
Figure 3.5: Pd versus SCR for $L = 2$ (HH, VV) and different pulses: (a) $M = 16$, (b) $M = 32$, (c) $M = 64$ 45

Figure 3.6: *Pd* versus SCR for $L = 2$ (HH, VV), $M = 32$ and $\rho t = 0.99$.....46
Figure 3.7: Pd for SCR = – 35 dB, $Pfa = 10-3$, $L = 2$ (HH, VV), $M = 32$: (a) Pd for Pol-AR-MF as a function of fd and ρt.....47
Figure 4.1: *Pfa* versus threshold for different values of Q for: (a) case study A, (b) case study B.....55
Figure 4.2: *Pd* versus SCR for *Pfa* = $10-3$, Swerling 0 target model and (a) case A, (b) case B.....57
Figure 4.3: *Pd* versus SCR for *Pfa* = $10-3$, Swerling I target model and (a) case A, (b) case B.....58
Figure 4.4: Performance evaluation for case study B with $\varrho = 0.93$ at $fd = 0.28$: (a) *Pfa* versus threshold for different values of Q, (b) *Pd* versus SCR for Swerling I target model for *Pfa* = $10-3$.....60
Figure 4.5: Measured *Pfa* versus nominal *Pfa* for $M = 32$, $L = 3$ (HH,VV,HV), different Q values and different training data size.....64
Figure 4.6: *Pd* vs SCR for the Mod-Pol-AR-AMF against a Swerling I target model in 66
Figure 4.7: SCR loss versus Q for differrent detection schemes against a Swerling I target model in (a) case study A, and (b) case study B.....67
Figure 5.1: Clutter power spectra at *starea4* data file.....70
Figure 5.2: Range – Doppler maps after using the Mod-Pol-AR-AMF with P = 32 and.....71
Figure 5.3: Measured *Pfa* versus nominal *Pfa* for $M = 32$, $L = 3$ (HH,VV,HV), different Q values and different training data.....72
Figure 5.4: *Pd* versus SCR with *Pfa* = 10^{-3}, M = 32 with different polarimetric channels for Q = 4.....73
Figure 5.5: *Pd* for SCR = -20 dB, *Pfa* = 10^{-3}, L = 2 (HH, VV), M = 32: (a) *Pd* for Mod-Pol-AR-AMF (P = 128) as a function of fd and ρt (b) *Pd* versus fd for ρt = 0 (continuous lines) and $\rho t = 0.99$ (dashed lines).....74
Figure 5.6: Sketch of the Mod-Pol-AR-AMF for PCL systems.....75
Figure 5.7: Sketch of the acquisition campaign geometry.....76
Figure 5.8: Acquisition Campaign equipment:.....76
Figure 5.9: Raw PCL detections over 50 consecutive datafiles using: (a) single-pol H and (b) single-pol V.....78
Figure 5.10: Raw PCL detections over 50 consecutive datafiles using: (a) P-GLRT and (b) Mod-Pol-AR-AMF with $Q = 3$.....79
Figure 5.11: Sketch of the Sub-optimal Mod-Pol-AR-AMF for PCL systems.....81
Figure 5.12: Empirical ROC curves for different detection schemes, using: (a) FMch1 (b) FMch2 (c) FMch3 (d) FMch4.....82
Figure 6.1: Qualitate behavior of the MSE versus the SNR for nonlinear DoA estimation. 87

Figure 6.2: Results for $N = 1$ and $K = 3$ ($d = [0 \;\; 2 \;\; 6.8]\,\lambda_1$) : (a) Theoretical MF beampattern (b) Pairwise error probability for a selected sidelobe for different SNR versus M. 97
Figure 6.3: Theoretical MF beampattern $Vtheo(u)$ for three-element array $d = [0 \;\; 2 \;\; 6.8]\,\lambda_1$ exploiting one or three frequency channels....98
Figure 6.4: Probability of outlier under CMA for a three-element array $d = [0 \;\; 2 \;\; 6.8]\,\lambda_1$ for different case studies, reported in Table 6.1. 100
Figure 6.5: Probability of outlier under UMA for a three elements array $d = [0 \;\; 2 \;\; 6.8]$ λ_1 for different case studies, reported in Table 6.1....104
Figure 6.6: MSE approximation under CMA for a three-element array $d = [0 \;\; 2 \;\; 6.8]\,\lambda_1$ for different case studies, reported in Table 6.1....106
Figure 6.7: MSE approximation under CMA for different four-element arrays and one snapshot from each of three frequency channels. The considered case studies are reported in Table 6.2....106
Figure 6.8: MSE approximation under UMA for different case studies reported in Table 6.1 and Table 6.2. 108
Figure 7.1: Processing scheme for a PCL system exploiting multiple frequency channels..110
Figure 7.2: Acquisition geometries during test campaigns #1 & #2 111
Figure 7.3: Enlarged view of the acquisition geometry during test campaign #2 112
Figure 7.4: Drones employed cooperative targets during test campaign #2 112
Figure 7.5: DoA estimation performance for test campaign #1 under CMA (a) Probability of outlier (b) MSE....114
Figure 7.6: DoA estimation performance for test campaign #2 under CMA (a) Probability of outlier (b) MSE....114
Figure 7.7: Test campaign #1: Localization results for 34 consecutive data files using (a) SF with $f1$ and $K = 2$, (b) MF with $K = 2$, (c) SF with $f1$ and $K = 3$, (d) MF with $K = 3$. 115
Figure 7.8: Dataset A: Localization results for 50 consecutive data files using (a) SF with $f0$ and $K = 2$, (b) MF with $K = 2$, (c) SF with $f0$ and $K = 3$, (d) MF with $K = 3$. 117
Figure 7.9: Dataset B: Localization results for 50 consecutive data files using (a) SF with $f0$ and $K = 2$, (b) MF with $K = 2$, (c) SF with $f0$ and $K = 3$, (d) MF with $K = 3$. 119

List of Tables

Table 2.1 Main parameters of DVB-T transmitter in Kiel....16
Table 2.2 Delphin aircraft technical details....18
Table 2.3 Number of correct detections with different polarimetric detection schemes and *Pfa* values in the absence of a prior cancellation stage....21
Table 2.4 Number of correct detections with different polarimetric detection schemes and *Pfa* values after the application of a 2-stage ECA-CD. 23
Table 4.1 Summary of defined quantities....51
Table 5.1 Collected FM radio channels....77
Table 5.2 Number of correct detections over the entire dataset, out of 9632 target occurrenciess, with measured $Pfa = 10^{-4}$....84
Table 6.1 Case studies A-E 99
Table 6.2 Case studies F-I....107
Table 7.1 Details of the data sets collected during the performed tests campaigns. 113
Table 7.2 Test campaign #1: Target detections and ambiguous plots 116
Table 7.3 Test campaign #2 : Target detections over 50 consecutive datafiles....120
Table 7.4 Test campaign #2 : Ambiguous plots over 50 consecutive datafiles....120

Nomenclature

H_0	Null (or target absent) hypothesis
H_1	Alternate (or target present) hypothesis
P_{fa}	False alarm probability
P_d	Detection probability
$\mathbf{x}$	Boldface and lower-case letter denotes vector
$\mathbf{X}$	Boldface and upper-case letter denotes matrix
x	Letter in normal font denotes a scalar
x_i	i-th component of vector $\mathbf{x}$
$\mathbf{X}_{ij}$	(i, j)-th element of matrix $\mathbf{X}$
$\mathbf{I}_N$	$N \times N$ identity matrix
$\mathbf{I}_{N \times M}$	$N \times M$ identity matrix
$\mathbf{0}_N$	$N \times N$ null matrix
$\mathbf{0}_{N \times M}$	$N \times M$ null matrix
j	The imaginary unit
$\widehat{(\cdot)}$	Estimate of $(\cdot)$
$(\cdot)^T$	Transpose of $(\cdot)$
$(\cdot)^*$	Conjugate of $(\cdot)$
$(\cdot)^H$	Hermitian (or conjugate transpose) of $(\cdot)$
$\lvert \cdot \rvert$	Determinant for matrices; Modulus for scalars
exp $(\cdot)$	Exponential function
log $(\cdot)$	Logarithm of $(\cdot)$ relative to base 10
ln $(\cdot)$	Natural logarithm of $(\cdot)$
$\mathrm{Pr}\{\cdot\}$	Probability
$E\{\cdot\}$	Statistical expectation
$\mathrm{tr}(\cdot)$	Trace of $(\cdot)$
rank $(\cdot)$	Rank of $(\cdot)$
$\Re(\cdot)$, $\Im(\cdot)$	Real and Imaginary part of $(\cdot)$

$\mathcal{CN}(\boldsymbol{\nu}, \mathbf{N})$	Complex Gaussian distribution with mean vector $\boldsymbol{\nu}$ and covariance matrix $\mathbf{N}$.
$\chi^2_N(\nu)$	Non-centrally Chi-squared distribution with N degrees of freedom and noncentrality parameter ν
AR $(Q-1)$	Auto-regressive process of order $(Q-1)$
$\Gamma(\cdot)$	Gamma function
$\mathrm{u}(\cdot)$	Unit step function
$\otimes$	Kronecker product
L	Number of available polarimetric channels
N	Number of available frequency channels
K	Number of available spatial channels

List of Acronyms

ADS–B	**A**utomatic **D**ependent **S**urveillance – **B**roadcast
AMF	**A**daptive **M**atched **F**ilter
AR	**A**uto – **R**egressive
CA	**C**ell **A**verage
CAF	**C**ross **A**mbiguity **F**unction
CCF	**C**ross-**C**orrelation **F**unction
CDF	**C**umulative **D**istribution **F**unction
CFAR	**C**onstant **F**alse **A**larm **R**ate
CMA	**C**onditional **M**odel **A**ssumption
CPI	**C**oherent **P**rocessing **I**nterval
CRB	**C**ramér – **R**ao lower **B**ound
CUT	**C**ell **U**nder **T**est
CW	**C**ontinuous **W**ave
DoA	**D**irection **o**f **A**rrival
DVB-S	**D**igital Video **B**roadcasting – **S**atellite
DVB-T	**D**igital **V**ideo **B**roadcasting – **T**errestrial
ECA	**E**xtensive **C**ancellation **A**lgorithm
ECA-CD	**E**xtensive **C**ancellation **A**lgorithm by **C**arrier and **D**oppler shift
ECA-S	**E**xtensive **C**ancellation **A**lgorithm - **S**liding
ERP	**E**quivalent **R**adiated **P**ower
FM	**F**requency **M**odulation
GLRT	**G**eneralized **L**ikelihood **R**atio **T**est
GPS	**G**lobal **P**ositioning **S**ystem
IID	**I**ndependent and **I**dentically **D**istributed
IO	**I**lluminator of **O**pportunity
MC	**M**onte **C**arlo
MIMO	**M**ultiple **I**nput **M**ultiple **O**utput

ML	**M**aximum **L**ikelihood
Mod-Pol-AR-AMF	**M**odified **P**olarimetric **A**uto – **R**egressive based **A**daptive **M**atched **F**ilter
MSE	**M**ean **S**quare **E**rror
NCI	**N**on-**C**oherent **I**ntegration
NULA	**N**on-**U**niform **L**inear **A**rray
OFDM	**O**rthogonal **F**requency **D**ivision **M**ultiplexing
OHGR	**O**sborne **H**ead **G**unnery **R**ange
PBR	**P**assive **B**istatic **R**adar
PCL	**P**assive **C**oherent **L**ocation
PDF	**P**robability **D**ensity **F**unction
Po	**P**robability of **O**utlier
Pol-AR-AMF	**P**olarimetric **A**uto – **R**egressive based **A**daptive **M**atched **F**ilter
Pol-AR-MF	**P**olarimetric **A**uto – **R**egressive based **M**atched **F**ilter
PRF	**P**ulse **R**epetition **F**requency
QAM	**Q**uadrature **A**mplitude **M**odulation
RCS	**R**adar **C**ross **S**ection
ROC	**R**eceiver **O**perating **C**haracteristic
RX	**R**eceiver
SCR	**S**ignal to **C**lutter power **R**atio
SINR	**S**ignal to **I**nterference-plus-**N**oise power **R**atio
SNR	**S**ignal to **N**oise power **R**atio
SP	**S**addle **P**oint
STAP	**S**pace – **T**ime **A**daptive **P**rocessing
TDOA	**T**ime **D**ifference **O**d **A**rrival
TX	**T**ransmitter
UAV	**U**nmanned **A**erial **V**ehicle
UHF	**U**ltra – **H**igh **F**requency
ULA	**U**niform **L**inear **A**rray
UMA	**U**nconditional **M**odel **A**ssumption

Chapter 1
Introduction

This Chapter introduces the main topics addressed in this work and gives an overview of what has been done. After a brief illustration of passive radar principles, the objective of this thesis is explained. Then, the innovative contributions made by this dissertation are detailed, and finally the outline of this thesis is reported.

1.1 Background

This Section focuses on the principles of passive radar systems and provides the motivation for this PhD project. Note that the purpose of this Section is by no means to be exhaustive, but to provide the background necessary to understand the motivation for the advancement developed and explored in this work. For a complete and detailed discussion on this topic, the interested reader is referred to the relevant literature, see e.g. [7],[40]-[43], [50],[51],[66],[104],[105],[120] and the references therein.

1.1.1 Passive Coherent Location systems principles

A Passive Bistatic Radar (PBR or Passive Coherent Location – PCL) system is a receive-only radar system that does not transmit electromagnetic energy on its own, instead it exploits signals emitted by sources of opportunity to perform target detection, localization and possibly imaging [40]. Such sources are usually referred to as Illuminators of Opportunity (IOs) and they can be communication systems, broadcast systems for public utility, other radar systems and so on.

A typical PCL system geometry is sketched in Figure 1.1. In general, two receiving channels are required, referred to as *reference* and *surveillance* channels. Since the transmitted waveform is unknown, the reference antenna is pointed toward the IO to collect a copy of the direct signal, as clean as possible. The surveillance antenna, on the other hand, is steered toward the area to be monitored to collect the reflections from targets.

The goal of PCL systems is to estimate the bistatic range and the bistatic velocity of a target [41]. To this aim, the sensor measures the time difference of arrival (TDOA) between the direct signal and the reflected echo and the bistatic range measurement R_B is retrieved, as follows

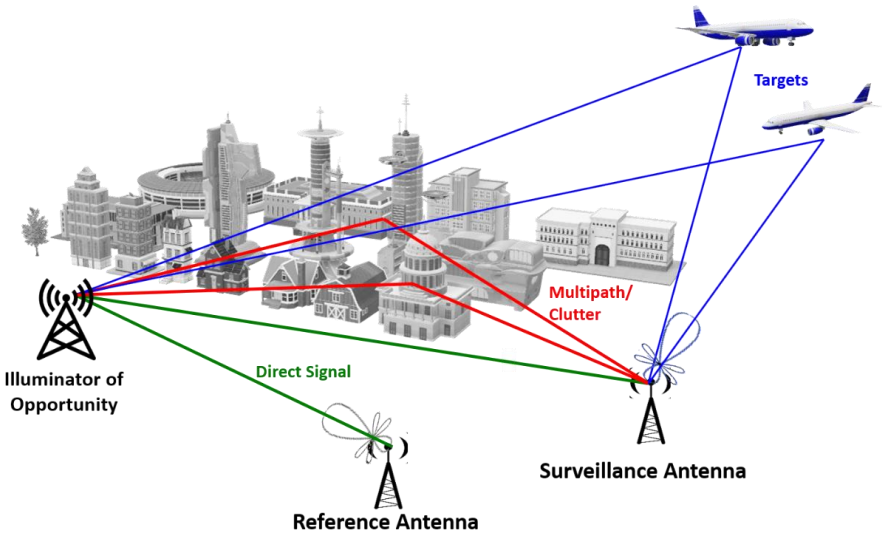

Figure 1.1: Sketch of the PCL geometry

$$R_B = R_T + R_R - B_L \tag{1.1}$$

where R_T and R_R define the ranges from target to transmitter (TX) and from target to receiver (RX), while B_L is referred to as *baseline* and represents the distance between the TX and RX. The bistatic range measurement locates the target on an ellipsoid, usually referred to as iso-bistatic range ellipsoid, that has the TX and the RX located at its foci and whose width is given by

$$\Delta R_B = c_0 \left[2\cos(\beta/2) \cdot B_W\right]^{-1} \tag{1.2}$$

where c_0 denotes the speed of light, B_W represents the bandwidth of the exploited signal and β is the bistatic angle between the directions from target to RX and TX. ΔR_B, usually called bistatic range resolution, defines the minimum separation that would allow two point-like scatterers to be distinguished.

Finally, a PBR can estimate the target bistatic Doppler frequency, defined as the rate of change of the bistatic range over time, i.e. $f_d = \frac{1}{\lambda}\frac{\partial}{\partial t}\left[R_T(t) + R_R(t)\right]$.

In the case where only the target is moving, while the TX and the RX are stationary the sough quantity is defined as

$$f_d = 2\,\frac{V}{\lambda}\cos(\delta)\cos(\beta/2) \tag{1.3}$$

denoting λ as the wavelength of the exploited signal, V as the target velocity and δ as the bistatic angle referred to the bistatic bisector. Note that the bistatic Doppler frequency will be equal to zero for targets moving along the baseline between TX and RX and for all targets moving along the bistatic iso-range, i.e. when R_B remains constant over time.

Finally, a Doppler resolution Δf_d is defined and it is roughly equal to the reciprocal of the coherent processing interval (CPI)

$$\Delta f_d = 1/CPI \tag{1.4}$$

1.1.2 Basic PCL processing

A block diagram of the basic signal processing steps foreseen in a PCL system is shown in Figure 1.2 and detailed in the following.

Disturbance Cancellation. Observing the geometry in Figure 1.1, it is evident that along with target echoes, the surveillance channel also receives a fraction of the direct signal emitted by the IO as well as strong clutter and multipath contributions. Therefore, the purpose of the first processing stage, referred to as disturbance cancellation stage, is to prevent such undesired contributions from masking low power target echoes. To this aim, several algorithms have been studied and developed, among which the Extensive Cancellation Algorithm (ECA), proposed in [22]. The latter is based on subtracting the undesired interference signal, estimated by summing up delayed and weighted replicas of the reference signal, from the surveillance signal.

Range-Doppler map evaluation. After the disturbance cancellation stage, the key step in the PBR processing chain is the bistatic range-Doppler map evaluation. It is based on the evaluation of the two-dimensional (2D) cross-correlation function (CCF) between the echo signals and different possible Doppler modulated replicas of the direct signal. This stage requires the highest computational load in the processing scheme and, depending on the application, it might also require a very large amount of data to be managed and complex operation to be performed real-time. Therefore, efficient implementations of the range-Doppler map evaluation have also been devised [66].

Target detection. As in all radar systems, the target detection stage is a decision process based on a comparison between a given cell under test (CUT) and a threshold, opportunely selected in order to guarantee a desired false alarm probability (*Pfa*). The most common solution is to use a varying threshold that adapts itself to the local disturbance characteristics in order to guarantee a constant false alarm rate (CFAR).

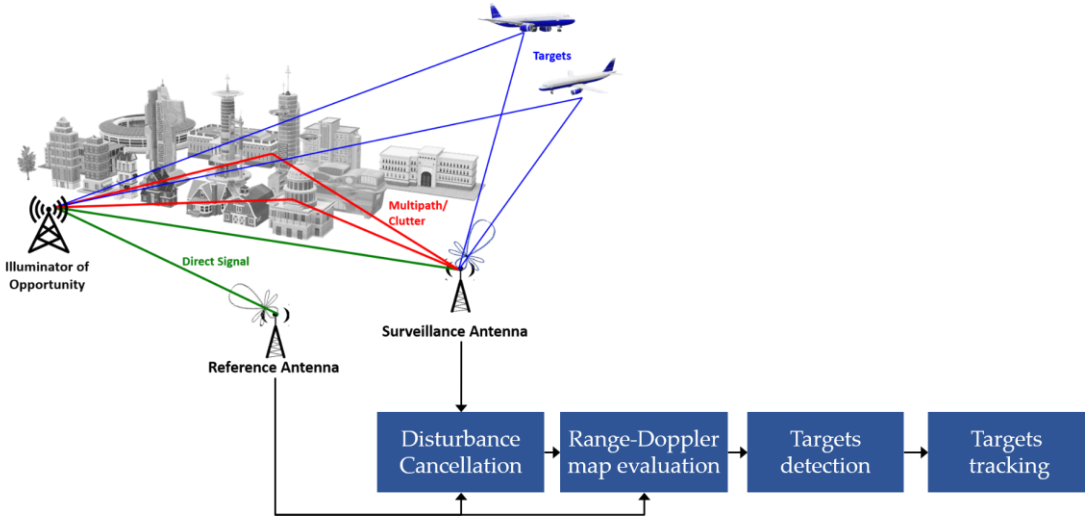

Figure 1.2: Sketch of the basic PCL processing scheme

Target tracking. Target detections collected from multiple consecutive CPIs can be further processed to produce tracks and reduce the resulting number of false alarms. Target tracking can be performed either in the bistatic range-Doppler domain or in the Cartesian plane, if possible.

1.1.3 Motivation

Due to the lack of *ad hoc* transmissions, PCL systems offer several advantages. First, their operability does not require dedicated spectrum allocation and the need to design, implement and manage only the receiving part requires a low cost of construction and maintenance. Moreover, the exploitation of existing signals, the low vulnerability to electronic countermeasures due to the intrinsically bistatic geometry and the low-cost and compact size of the employed receivers enable covert operations, making such systems extremely appealing for military purposes. Furthermore, thanks to both their small size and lack of electromagnetic pollution, PCL sensors have a reduced impact on the environment and can be employed in areas where conventional radars could not be deployed, e.g. coastal or urban areas. Thanks to all the benefits it offers, PCL technology has received a significant renewed interest inside the worldwide scientific community in the last two decades. As a result of the emerging development of passive radars, they are reaching a stage of maturity and the first commercial PCL systems have started to appear in the marked for various defence and civil applications.

However, despite the effectiveness of the processing techniques devised for the purpose and the significant progress that has been made, the performance of a PCL sensor might still be strongly limited. It is well known that the main limitations of PBR stem from the lack of control over the transmitted waveform structure and the strong direct signal and multipath

interferences. For these reasons, advanced signal processing strategies must be developed to increase the reliability and the overall capabilities of PCL systems. In this thesis a significant focus will be devoted to deriving different advanced solutions that aim at improving the target detection performance as well as the target localization capability.

1.2 Goal of the Thesis and Innovative Contributions

The goal of this thesis is to address the main limitations of PCL technology and to derive advanced signal processing strategies, based on the exploitation of the information diversity conveyed by multiple receiving channels.

The main innovative contributions made by this thesis can be divided in two broad areas, that will constitute Part I and Part II of this work and are briefly detailed in the following.

Although the ideas underlying the main achievements reported in this work arise from the need to overcome PCL systems limitations, the field of application of the devised signal processing techniques, analytical performance characterizations and design strategies is not limited to passive radars. This aspect increases the scientific value of the results obtained.

1.2.1 Exploitation of polarization diversity for target detection

The first part of this dissertation deals with the joint exploitation of signals collected by different polarimetric channels to enhance the target detection performance.

Polarization diversity has been widely employed to improve radar systems performance and, in recent years, suitable strategies to exploit this additional information have been proved to be able to enhance the target detection capability also in PCL systems. Therefore, the first part of this work starts with demonstrating the benefits of exploiting polarization diversity in PCL systems.

Following the promising results obtained using Frequency Modulation (FM) radio signals, suitable strategies that exploit the polarimetric information are considered and a performance assessment against Digital Video Broadcasting - Terrestrial (DVB-T) based PCL data is carried out.

Then, we derive a new parametric adaptive detection scheme that also exploits the temporal information to counteract the disturbance thus further increasing the target detection capability. Several detectors that exploit a set of polarimetric-temporal (or polarimetric-temporal-spatial) observations have been conceived and extensively studied in the literature. However, these approaches are based on the availability of a large amount of target-free training data that allow to estimate and invert the unknown disturbance covariance matrix. This requirement becomes an issue in applications where the number of adaptive degrees of freedom is large, as well as in heterogeneous environment where the available secondary data are not representative of the disturbance in the cell under test. This is the case of PCL systems that typically use long CPIs, i.e. very high number of temporal

samples, to attain desired levels of signal-to-noise ratio (SNR). We address this issue by restoring to a parametric approach.

In this framework, the following main contributions are made by this work:

- A performance assessment of locally adaptive detection schemes that exploit the polarization diversity to increase the target detection performance of DVB-T based PCL systems.
- The derivation of a novel polarimetric adaptive detection strategy based on a multi-channel auto-regressive (AR) model for the disturbance.
- A complete theoretical characterization of the asymptotic performance of the derived detection scheme, using two different target fluctuation models, namely Swerling 0 and Swerling I.
- A performance assessment of the proposed detection approach via numerical analysis, also including the case of disturbance components with different spectral characteristics.
- The introduction of an appropriate modification to the derived detector to make it robust to typical spectral model mismatches.
- An experimental performance assessment against two different datasets. First, being the field of application of the derived solution not limited to PCL systems, we use data collected by means of an active radar. Then, we use data collected by means of a FM radio-based PCL system.
- The derivation of a sub-optimal implementation of the derived polarimetric detection scheme for it to be performed with a reduced computational burden.

1.2.2 Exploitation of spatial and frequency diversity for target localization

Direction of Arrival (DoA) estimation of narrow-band signals is a key problem in sensor array signal with a variety of application fields, such as radar, sonar, mobile communications, etc. However, most studies published over the years addressed the problem of characterizing the performance of DoA estimators under asymptotic assumptions, where asymptotic generally refers to either a high number of samples or high SNR regime. Nevertheless, in many practical applications, such as PCL systems, such conditions are unlikely to be continuously guaranteed. In fact, it is not unlikely that these systems operate in the low SNR regime, where accurate angular localization might represent a challenging task. This is especially true when a limited number of receiving sensors is employed in order to limit the system complexity.

Therefore, the second part of this work deals with target DoA estimation for system that jointly exploit signals received at multiple carrier frequencies, as a mean to mitigate the

problem of angular ambiguities in arrays employing a limited number of channels.

In this framework, the following main contributions are made by this work:

- A reliable theoretical performance characterization of a multi-carrier maximum likelihood (ML) DoA estimator in the threshold region, i.e. in low SNR regime. We separately treat the case of deterministic and stochastic signal model and we derive approximations of the mean square error (MSE) and probability of outlier in both cases.
- An extensive simulated analysis to prove the tightness of the derived expressions and to characterize the benefits stemming from exploitation of signals emitted at multiple carriers.
- The demonstration of the benefits of the multi-carrier approach via an experimental validation against real data collected with Leonardo S.p.A. using AULOS DVB-T based PCL system for both aircraft and drone surveillance.

1.3 Outline of the Thesis

The remainder of this thesis is organized as follows.

Chapter 2 shows the benefits of exploiting the polarimetric information in PCL systems using DVB-T signals. Two different strategies are considered and compared, originally devised for FM radio-based PCL systems and we show their effectiveness against DVB-T based PCL data collected by Fraunhofer FHR.

Chapter 3 deals with the problem of target detection in coherent radar systems exploiting polarimetric diversity. By modelling the disturbance affecting the data as a multi-channel AR, a new polarimetric adaptive detector is derived, which aims at improving the target detection capability while relaxing the requirements on the training data size and the computational burden with respect to existing solutions. A complete theoretical characterization of the asymptotic performance of the derived detector is provided, using two different target fluctuation models. The effectiveness of the proposed approach is shown against simulated data, in comparison with alternative existing solutions.

Chapter 4 reports the performance assessment of the detection scheme derived in Chapter 3 is extended, by means of theoretical and simulated analyses, to include the case of disturbance components with diverse spectral characteristics. Consequently, an appropriate modification is introduced to the detection scheme to make it robust to typical spectral mismatches occurring in practical situations. Finally, the effectiveness of the resulting detection scheme is proved against both simulated and experimental data.

Chapter 5 demonstrates the effectiveness of the polarimetric adaptive detection scheme introduced in Chapter 3 and Chapter 4 against real data. Specifically, two different set of experimental data are used, one collected by means of an active radar and the other collected using a FM radio-based PCL system. Some reasonable approximations are introduced in order to reduce the computational burden required by the direct implementation of the derived detector and enable an extensive analysis over the entire dataset. Chapter 5 concludes Part I of this thesis.

Chapter 6 presents the performance characterization of a DoA estimator in the low SNR region. The case of a sensor array simultaneously collecting signals emitted at multiple carrier frequencies by a single source is considered. A ML approach is used as a reference method for DoA estimation and its accuracy is characterized in terms of MSE.

In **Chapter 7**, the benefits of the joint exploitation of spatial and frequency diversity for target DoA estimation are demonstrated via an experimental validation against real data collected with Leonardo S.p.A. using AULOS DVB-T based PCL system for both aircraft and unmanned aerial vehicle (UAV) surveillance. Chapter 7 concludes Part II of this thesis.

Chapter 8 summarizes the main results of this study and provides an outlook for further work.

Mathematical details are reported in the Appendices.

Part I
Exploitation of polarization diversity for target detection

Chapter 2
Locally adaptive polarimetric target detection

The purpose of this Chapter is to investigate the possibility of exploiting the polarimetric information diversity in PCL system that use DVB-T signals. To this end, suitable polarimetric detection strategies are considered, that were devised for FM-radio based PCL. The performance analysis is carried out against real data collected the passive radar sensor PARASOL from Fraunhofer Institute FHR. In Section 2.1, the main stages of a basic DVB-T based passive radar signal processing scheme is summarized and in Section 2.3 the polarimetric detection schemes that will be compared are described. Section 2.4 reports the results experimental validation, including the acquisition campaign and the employed data set description. Finally, some conclusion remarks are drawn in Section 2.5.

2.1 Background and Motivation

Following the consideration that target echoes typically show a random polarization, it was observed that the use of a fixed polarization on receive might result in a significant SNR degradation [16],[24]. It can therefore be expected that a proper combination of the signals received at differently polarized antennas might yield a detection performance improvement for the resulting system. Possible solutions along this line have been investigated in [16],[18]. A very preliminary polarimetric processing scheme was firstly investigated in [16] where a simple non-coherent integration (NCI) of the results obtained at orthogonal polarized surveillance antennas was proposed for FM radio-based PCL. However, the authors in [18] proved that, besides the expected improvement due to NCI of target echoes received on multiple channels, the polarization diversity might be fruitfully exploited to reject the disturbance contributions that still limit the achievable performance (e.g. cancellation residuals or interfering signals). To this purpose, a locally adaptive detection scheme was derived by resorting to a generalized likelihood ratio test (GLRT) [60] approach, able to adaptively exploit the polarimetric differences between the target and the competing disturbance to improve the target discrimination capability.

The effectiveness of the polarimetric approaches proposed in [16],[18] was extensively demonstrated for an FM radio-based PCL system. Specifically, the conceived schemes were shown to be able to mitigate also the effect of co-channel and adjacent-channel interferences arising from the typical spectrum management for FM radio broadcast transmissions (i.e. frequency reuse, broad spectrum roll-off of FM radio signals, etc.).

The successful and promising results obtained in the FM radio band have been the strong motivation behind the investigation of the potential benefits that the use of polarization diversity could yield also in DVB-T based PCL systems. This work was carried out in collaboration with the colleagues of Fraunhofer FHR.

2.2 Multi-polarimetric DVB-T based PCL signal processing

The signals collected by different polarimetric channels separately undergo the first two main processing stages, namely the disturbance cancellation and the range-velocity maps evaluation stage. Then, the target detection is performed by exploiting the output of a single channel or by jointly processing the outputs of multiple channels, as described in Section 2.3.

Direct signal reconstruction. In the case of DVB-T signal as IO, due to the digital coding of orthogonal frequency division multiplexing (OFDM), it is possible to decode the transmitted reference signal. Hence there is no need for a dedicated reference channel. In fact, digitally coded illuminators allow the receiver to reconstruct the transmitted signal by demodulating and re-modulating the received signal, according to the DVB-T standard. This operation consists of three main steps: (i) synchronization to the transmitter, (ii) demodulation and decoding of the synchronized signal, (iii) remodulation of the decoded signal. The output of such processing would be a cleaned replica of the direct signal, free of multipath echoes [95], which may be used as reference signal for the following stages. The direct signal reconstruction approach is a valuable solution for reducing the number of receiving channels in a PCL, but it requires a small bit error rate in the decoding of the bit stream, which indirectly calls for enough SNR for the direct signal. The bit error rate can be in principle reduced by implementing the error correction codes foreseen in the DVB-T standard.

Disturbance cancellation. The Extensive Cancellation Algorithm - Carrier and Doppler shift (ECA-CD [94]) has been used in order to effectively reduce the clutter contribution due to multipath. Specifically, in this work a multi-stage ECA approach has been applied. This means, the ECA filter is applied to the Doppler bin that collects the most interference power. Subsequently, the process is repeated on the output of the first ECA stage. In addition, the ECA filter is applied in the range frequency domain (that is, ECA-C) to account for different

multipath/interference that may occur within the spectrum of the DVB-T signal. The further enhancement from ECA-C to ECA-CD expands the clutter subspace in the Doppler domain. This is done by adding replicas of the reference signal shifted by fractions of the Doppler resolution bin (typical values are Doppler frequencies $f_{ECA-CD} = \pm 0.75$Hz). Further details can be found in [94].

Bistatic range-velocity map evaluation. The evaluation of the bistatic range-velocity map is the key step of each PCL processing [66]. It is well known that its purpose is to recognise weak target contributions in the surveillance signal, delayed and Doppler shifted. In the present implementation, the range-velocity map is calculated based on the periodic structure of the DVB-T signal. Namely, for each DVB-T OFDM symbol the synchronization to the transmitter, decoding and remodulation of the DVB-T symbol is performed. Then, always at DVB-T symbol level, the reconstructed clean replica of the transmitted symbol is cross-correlated with the corresponding surveillance signal. This cross-correlation implements the so-called reciprocal filter [96], which equalizes the sub-carriers power over the DVB-T spectrum, and it performs a range compression of the single DVB-T symbol. It is easy to show that the reciprocal filter leads to a flat spectrum before final range inverse Fourier transform, thus minimizing spurious peaks in the resulting map. After that, the range compressed DVB-T symbols are juxtaposed in the slow-time (i.e. in the coherent integration time interval) and finally a discrete Fourier transform is performed to synthesize the Doppler dimension that can be then easily mapped into a corresponding velocity axis. The output of this stage is a bistatic range-velocity map in which targets' echoes and disturbance sources are included. The latter ones may include, besides thermal noise, cancellation residuals and interferences. These contributions might severely affect each map by increasing its background level, thus limiting the detection of targets' echoes. For instance, for a FM radio-based PCL system it has been shown that the disturbance level may be enhanced up to 15-20 dB above the nominal system noise level [18]. Moreover, this effect might significantly vary with time and with the adopted surveillance antenna polarization.

2.3 Polarimetric detection schemes

In a conventional single-pol operation, i.e. if $L = 1$, once the bistatic range-velocity map has been evaluated, a Cell Average-CFAR (CA-CFAR) threshold can be applied to detect targets with a given probability of false alarm. In contrast, when multiple receiving channels are connected to differently polarized surveillance antennas, various approaches can be considered to jointly exploit the outputs of the L polarimetric channels, according to the assumptions that are made on the disturbance statistical properties. The two considered detection schemes are described in the following Sections.

2.3.1 Polarimetric Non-Coherent Integration

Let us consider the bistatic range-velocity maps obtained at the L polarimetric surveillance channels, say $\chi_l[r, v]$, $l = 0, \ldots, L-1$. For a given CUT at range bin r_0 and velocity bin v_0, the results of the L channels are collected in a complex vector $\boldsymbol{\chi}_0 = [\chi_0[r_0, v_0], \ldots, \chi_{L-1}[r_0, v_0]]^T$. In the following, we assume that target echoes at the L polarimetric channels have unknown complex amplitudes, i.e. $\boldsymbol{\chi}_0 = \mathbf{s}_0 = [\alpha_0 \ldots \alpha_{L-1}]^T$ in the absence of interference, where α_l is the unknown complex amplitude of the target at the l-th polarimetric channel.

Let us make the simplifying assumption that the interference affecting different channels is statistically independent and identically distributed (i.i.d). In addition, let us assume $\boldsymbol{\chi}_0$ to follow a complex normal distribution with zero mean vector under the H_0 hypothesis (target absent) and mean vector $\mathbf{s}_0$ under hypothesis H_1 (target present) and covariance matrix $\sigma_d^2 \mathbf{I}_L$, being σ_d^2 the interference power on the single polarimetric channel, i.e. $\boldsymbol{\chi}_0|_{H_\varrho} \sim \mathcal{CN}(\varrho \mathbf{s}_0, \sigma_d^2 \mathbf{I}_L)$, with $\varrho = 0,1$. The assumption of a Gaussian distributed disturbance affecting each map is widely adopted in the technical literature especially when dealing with low resolution radar systems. In particular, recent studies have shown that it is a quite accurate assumption to describe clutter echoes in passive radar based on DVB-T signals, even in coastal scenarios [28]-[29]. Moreover, we observe that a Gaussian distributed background is here assumed to properly describe the overall disturbance contributions that typically include both clutter echoes and interference from other transmitters. Under these hypotheses, a quite effective approach to enhance the signal-to-interference-plus-noise ratio (SINR) on the target is to resort to a non-coherent integration NCI across the polarimetric channels [16]. Specifically, the outputs obtained at the L polarimetric channels are incoherently summed after square law detector:

$$\|\boldsymbol{\chi}_0\|^2 = \sum_{l=0}^{L-1} |\chi_l[r_0, v_0]|^2 \tag{2.1}$$

Then, assuming that the interference is (locally) homogeneous on the integrated range-velocity map, a CA-CFAR detection scheme is adopted to detect the target presence. To this purpose, we define a set $I_{[r_0,v_0]}$ of P indices that identify range-velocity bins surrounding the CUT ($\|\boldsymbol{\chi}_t\|^2$, $p \in I_{[r_0,v_0]}, |I_{[r_0,v_0]}| = P$). The average intensity estimated over these P secondary bins is used to scale the result of (2.1), before thresholding:

$$\frac{\|\boldsymbol{\chi}_0\|^2}{\sum_{t \in I_{[r_0,v_0]}} \|\boldsymbol{\chi}_t\|^2} \underset{H_0}{\overset{H_1}{\gtrless}} \eta_{P-NCI} \tag{2.2}$$

This detection scheme will be referred to as the P-NCI. The threshold η_{P-NCI} can be found by numerically inverting the following expression of the theoretical false alarm probability *Pfa* [16]

$$P_{fa} = \sum_{l=0}^{L-1} \binom{PL+l-1}{l} \left(\frac{\eta}{PL}\right)^{l} \left(1+\frac{\eta}{PL}\right)^{-PL-l} \tag{2.3}$$

where the integration stage over multiple receiving channels has been properly taken into account [19]. The advantages of the P-NCI scheme are mainly due to the target echo enhancement resulting from the NCI of its contribution on different channels. In addition, some benefits are provided by the capability to average the severe interference in bad polarimetric channels with that appearing in the good ones, thus reducing its impact on the final performance. However, when an NCI scheme is adopted, the capability to control the actual false alarm rate is often jeopardized. This reveals the weakness of the hypothesis we have made concerning the statistical independence of the disturbance affecting different polarimetric channels. For the above reasons, an alternative technique must be introduced, aiming at fruitfully exploiting the polarization diversity to reject the disturbance contributions that might limit the achievable detection performance.

2.3.2 Polarimetric locally adaptive Generalized Likelihood Ratio Test

By admitting that the disturbance limiting the target detection is mainly related to external sources (e.g. clutter cancellation residuals, co-/adjacent-channel interferences, etc.), such disturbance cannot be assumed uncorrelated between different polarimetric channels. Moreover, based on the assumption that the target polarimetric characteristics might be very different from the disturbance, a novel adaptive detection scheme can be derived, aiming at exploiting the polarimetric differences and at improving the target discrimination capability.

To this purpose, complex vector $\boldsymbol{\chi_0}$, collecting as before the L polarimetric channels outputs at the CUT, is assumed to follow a complex normal distribution with mean vector $\varrho\mathbf{s}_0$ under the H_ϱ hypothesis ($\varrho = 0,1$) and covariance matrix $\mathbf{D}$, i.e. $\boldsymbol{\chi_0}|_{H_\varrho} \sim \mathcal{CN}(\varrho\mathbf{s_0}, \mathbf{D})$. In addition, a set of P secondary vectors, $\boldsymbol{\chi_p}$, $p = 1, \ldots, P$, are available, containing the output of the L maps at range-velocity locations adjacent to the CUT, i.e. $\boldsymbol{\chi_p} = \left[\chi_0[r_P, v_p] \ldots \chi_{L-1}[r_p, v_p]\right]^T$. They are assumed to be i.i.d with the same statistic of $\boldsymbol{\chi_0}$ under the H_0 hypothesis. By resorting to the GLRT approach [60], the detection test [18] is obtained:

$$\boldsymbol{\chi_0}^H \widehat{\mathbf{D}}^{-1} \boldsymbol{\chi_0} \underset{H_0}{\overset{H_1}{\gtrless}} \eta_{P-GLRT} \tag{2.4}$$

where $\widehat{\mathbf{D}} = \sum_{p=1}^{P} \boldsymbol{\chi_p}\, \boldsymbol{\chi_p}^H$ is the sample covariance matrix and η_{P-GLRT} is the threshold.

The detector in (2.4) will be referred to as P-GLRT. The threshold can be properly selected according to the theoretical expression of the *Pfa* in [18]:

$$P_{fa} = \frac{(1-\kappa)^{P-L+1}}{\Gamma(P-L+1)} \sum_{l=0}^{L-1} \frac{\Gamma(P-l)}{\Gamma(L-l)} \kappa^{L-l+1} \tag{2.5}$$

being $\eta = P\frac{\kappa}{(1-\kappa)}$. As is apparent from (2.4) the P-GLRT approach can be interpreted as the cascade of a whitening transformation followed by the NCI of the whitened output. Therefore, it still benefits from the integration of target echoes across different polarimetric channels. However, differently from P-NCI, it has the additional capability to reject the disturbance contributions (i.e. cancellation residuals or co-/adjacent- channel interfering transmissions) limiting the PCL performance.

2.4 Experimental validation against DVB-T based PCL data

In this Section a performance assessment is carried out on experimental data. First, the acquisition campaign carried out by Fraunhofer FHR and the employed data set are described. Then, the experimental results are reported.

2.4.1 Acquisition campaign

The experimental dataset used for the performance assessment has been collected during a field trial conducted on September 24, 2014, in Eckernförde, Germany. A map of the area where the experimental campaign took place is reported in Figure 2.1.

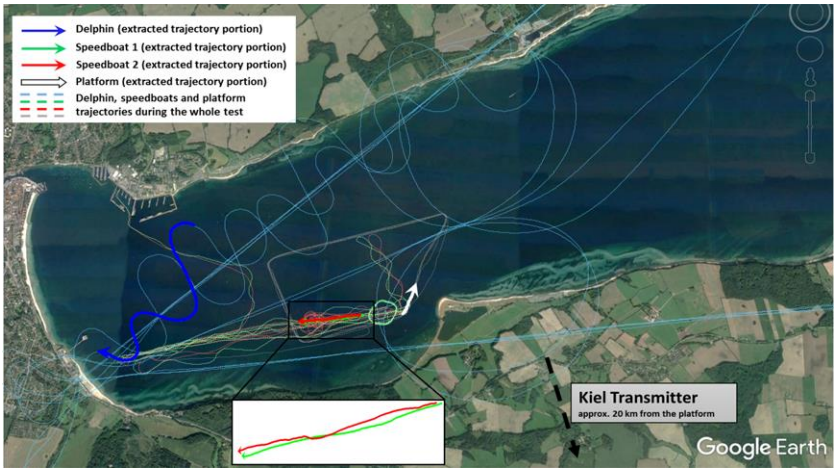

Figure 2.1: Sketch of the acquisition geometry

Table 2.1
Main parameters of DVB-T transmitter in Kiel

Position (WGS-84)	10°60'6.2''E, 54°18'2.3''N
Modulation	16-QAM
Site Elevation [m] / Antenna Height [m]	38/ 219
Frequency [MHz]	666
ERP [kW]	47
Transmitted polarization	Horizontal
Position (WGS-84)	10°60'6.2''E 54°18'2.3''N

It also sketches the adopted acquisition geometry and the paths of the moving objects employed. Specifically, their trajectories during the whole test are represented in dotted lines, while the portions of the trajectories exploited in this work are represented in bold continuous lines.

2.4.1.1 DVB-T based passive radar setup

The exploited IO is located in Kiel (approximately 20 km away from the receiver site) and broadcasts DVB-T signals in a single frequency network. It is working in 8k transmission mode, with 6817 OFDM carriers employed, in a 16-QAM scheme and a guard interval of 1/4. We used the DVB-T signal broadcasted at 666 MHz. Further details about the transmitter of opportunity are listed in Table 2.1.

The experimental PCL system PARASOL [49] developed at Fraunhofer FHR was employed. It consists of two parallel receiving channels, the receiver front-end and the data and signal processing unit (see Figure 2.2). Pre-processing of the data includes synchronization to the transmitter, demodulation/remodulation of the DVB-T signal, and range compression through reciprocal filter as briefly discussed in Section 2.2 (see also [81]). For the purpose of our analysis, the two available channels were connected to two cross-polarized antennas. In particular two linearly polarized log-periodic antennas have been used, manufactured by Schwarzbeck, with a gain of 7dBi in the frequency band under test during the trials (see more specifications in Figure 2.2(a)). The antennas were spaced approximately one meter apart1 and rotated by 90 degrees one to the other, to collect the horizontally and vertically polarized versions of the received echoes.

[1] An antenna spacing of approximately one meter has been proven to adequately limit antenna coupling effects for these specific antennas at this range of operating frequencies in preliminary anechoic chamber measurements.

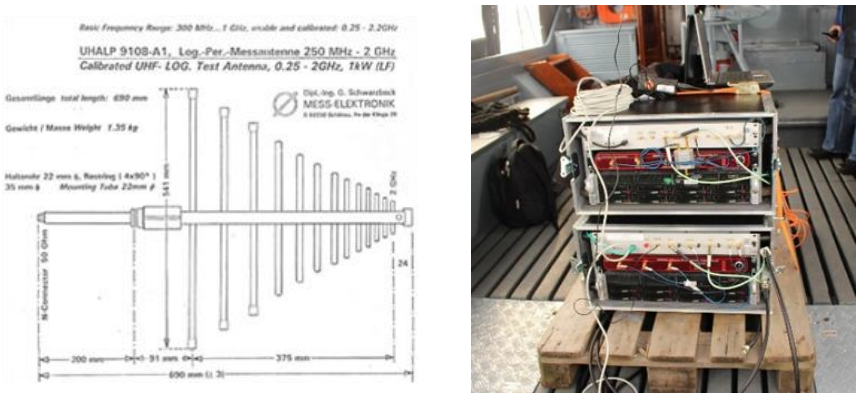

(a) (b)

Figure 2.2: Sketch of PARASOL system:
(a) Antenna unit (b) Data and signal processing unit

(a) (b)

Figure 2.3: Cooperative targets: (a) Delphin aircraft (b) One of the speedboats

The system PARASOL was mounted on a moving platform (namely a military boat about 15 meters long), describing a trapezoidal loop in the fjord, as shown in dotted grey in Figure 2.1. However, during the acquisition period reported in the following, it approximately moved on a rectilinear trajectory covering a global distance of 500m (see the bold white portion of the trajectory in Figure 2.1).

2.4.1.2 Adopted methodology

The results are reported for 168 consecutive data files, for a total acquisition duration of approximately 96 seconds. All the available data files have been processed according to the basic DVB-T based PCL processing scheme described in Section 2.1. Then the polarimetric detections schemes illustrated in Section 2.3 have been applied and their results are compared to those obtained with a single-polarization (shortened to single-pol in the following) operation using either the Vertical (V) or the Horizontal (H) polarimetric channel separately.

Being interested in the detection capability provided by different approaches, the attention is focused on the results obtained against a few cooperative targets. Specifically, one ultra-light aircraft and two identical speedboats have been employed as cooperative targets.

Table 2.2
Delphin aircraft technical details

Motor	Rotax 912 ULS
Art	4-Zylinder Boxer
Revolutions Per Minute (RPM)	5800
Tank capacity	120 liter
Service ceiling	3000 m
Top speed	260 km/h
Cruise speed	180 km/h
Stall speed	65 km/h
Empty weight	295 kg

Table 2.2 shows some technical details of the aircraft Delphin (see Figure 2.3(a)) from Fraunhofer FHR. The true trajectory of Delphin during the whole test is reported in Figure 2.1 (in dotted light blue) as provided by the Global Positioning System (GPS) receiver on-board. The availability of truth-data for the cooperative targets allowed us to evaluate the performance of the PCL system, in terms of number of correct detections. We recall that the bold continuous portion of the trajectory in Figure 2.1 corresponds to the considered acquisition interval. The speedboats are two identical 7m long rubber boats (see Figure 2.3 (b)), equipped with GPS receivers. Their true trajectories are reported in Figure 2.1 in green and red, respectively. Since the two speedboats navigated very close to each other during the whole test, their trajectories largely overlap.

During the considered acquisition period (see the zoom in Figure 2.1), they describe half period displaced sinusoids around a common rectilinear trajectory, moving away from the receiver platform.

Based on the *a priori* knowledge of the bistatic geometry, the available target true trajectories are projected onto the bistatic range-velocity plane. This allows a direct comparison with the plots provided by the PCL sensor. See for example Figure 2.4 where the bistatic trajectories of Delphin and of the two speedboats are reported as blue, red, and green continuous lines, respectively. Therefore, a given PCL plot obtained at a specific data file is declared to be a "correct detection" when it appears at the expected bistatic range-velocity location occupied by one of the cooperative targets at the considered time instant. To make the procedure robust to the inaccuracies of both the PCL measurements and the GPS data projection onto the bistatic plane, proper confidence intervals in range (± 100 m) and velocity (± 3 m/s) have been defined for the described association stage. With this counting procedure, reasonably accurate estimates of the detection rate can be obtained because, when the false alarm rate is kept sufficiently low, it is very unlikely to include false plots within the correct detections.

2.4.2 Results

By recalling the processing scheme depicted in Section 2.2, two sets of results are reported in the following sub-Sections. Specifically, in Section 2.4.2.1 the possibility of removing the disturbance cancellation stage separately performed at each polarimetric channel has been considered. Subsequently, in Section 2.4.2.2 the detection performance analysis has been repeated, after the application of the disturbance cancellation scheme illustrated in Section 2.2.

2.4.2.1 Results obtained without disturbance cancellation at each channel

The considered experimental test is representative of a short-range surveillance application against both aerial and maritime targets. In such conditions the capability to limit the computational load required to attain given performance might be a key point as it in principle enables a real time operation and, consequently, fast reaction times. To this purpose, we considered the possibility of avoiding a dedicated disturbance cancellation stage to be separately applied at each receiving channel. This turns out to be a challenging condition in which the considered polarimetric schemes could be interestingly tested. In fact, in the absence of a preliminary cancellation stage, the detection of potential targets competes with the high-power direct signal and multipath returns that spread over the range-velocity maps. Therefore, we report the detection results obtained when skipping the disturbance cancellation block in Section 2.2 The two remaining processing stages (direct signal reconstruction and bistatic range-velocity map evaluation) have been regularly applied against the received data.

Four different approaches have been employed at the target detection stage: (i) single-pol operation using the horizontally polarized channel only (single-pol H), (ii) single-pol operation using the vertically polarized channel only (single-pol V), (iii) P-NCI, and (iv) P- GLRT.

In Figure 2.4 we report on the bistatic plane the raw detection results obtained after each approach, compared to the GPS based trajectories available for the three cooperative targets. Specifically, the relative bistatic range axis represents the path transmitter-target-receiver, minus the baseline, while the bistatic velocity represents the absolute sum of the radial velocities of all moving objects. In fact, the returns from stationary clutter appears slightly Doppler shifted. The raw detections collected for the 168 consecutive data files, are reported as brown plots in a common plane. The temporal information is mapped in brown graduating shades, starting from the darkest one (see colorbars in Figure 2.4 and in Figure 2.5).

For all the considered detection schemes, the threshold has been set in order to obtain a nominal $Pfa = 10^{6}$. Correspondingly, for each approach, we report in Table 2.3 the number of correct detections provided against the three cooperative targets. For the detailed explanation of the counting procedure, please refer to Section 2.4.1.2. In Table 2.3, also the results obtained with different setting of the nominal Pfa are reported for an extended performance comparison.

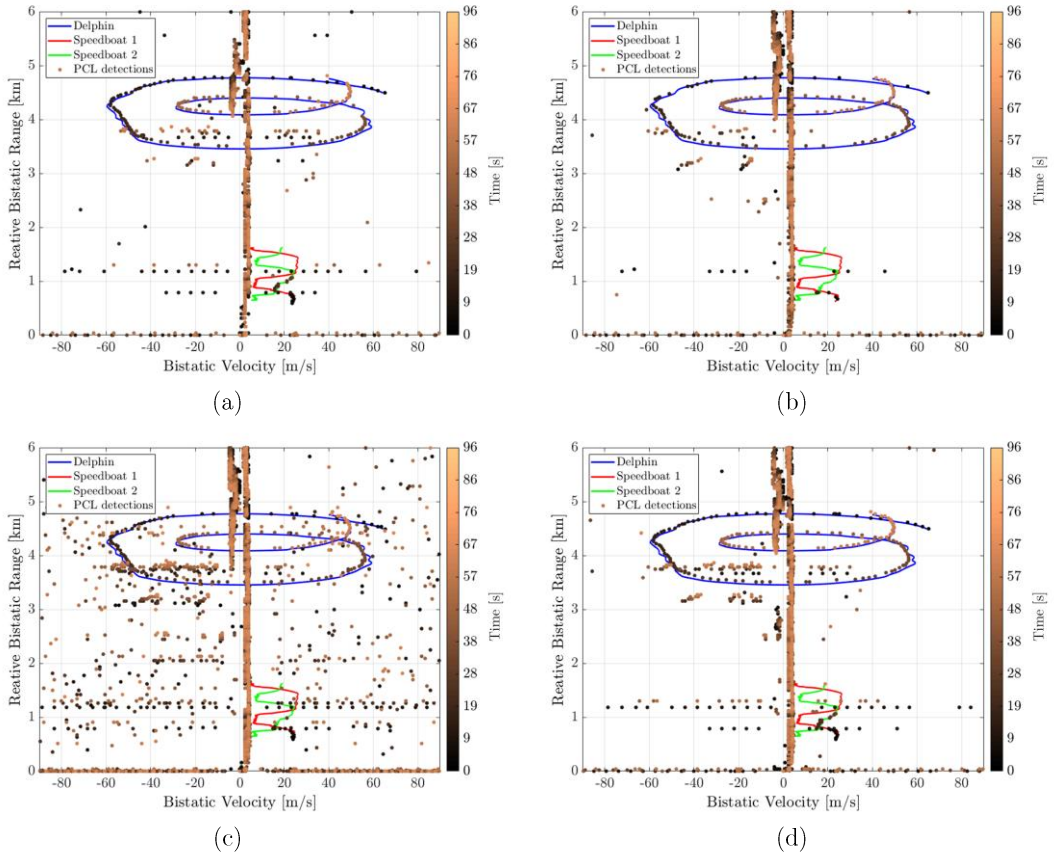

Figure 2.4: Detection results without applying any cancellation stage for $Pfa = 10^6$ and different detection schemes : (a) single-pol H, (b) single-pol V (c) P- NCI (d) P-GLRT

Based on the results in Figure 2.4 and Table 2.3, the following considerations are in order:

- The use of a single-pol operation leads to quite different results depending on the polarization of the employed antenna. This is well in line with the results in [16], [24]. Specifically, for this dataset we can say that, on average, the single-pol H yields better results in terms of number of correct detections against all the three targets considered. Incidentally, we recall that the exploited IO uses horizontal polarization. Nevertheless, this trend is not stable, and it may change with time. Namely, the single-pol V occasionally provides correct detections at scans where the single-pol H experiences a missed detection (see e.g. the Delphin tracks portion between 4-4.2 km and 40-60 m/s in Figure 2.4 (a) and (b)). This can be explained by observing that the targets' echoes typically show a random polarization due to the reflection of the transmitted signal on the complex structures of the targets.
- A P-NCI approach (Figure 2.4(c)) only allows to slightly increase the number of correct detections against the aerial target Delphin with respect to the best performing single-pol channel.

Table 2.3
Number of correct detections with different polarimetric detection schemes and Pfa values in the absence of a prior cancellation stage.

	Delphin				Speedboat 1				Speedboat 2			
Pfa	single pol H	single pol V	P-NCI	P-GLRT	single pol H	single pol V	P-NCI	P-GLRT	single pol H	single pol V	P-NCI	P-GLRT
10^{-5}	134	121	142	149	14	3	14	17	19	4	5	22
10^{-6}	131	114	140	145	11	3	10	13	16	2	4	21
10^{-7}	130	107	134	142	10	1	8	11	14	1	4	16
10^{-8}	127	97	131	142	7	0	6	10	9	1	4	10

Furthermore, the advantage gets smaller as the Pfa decreases and this shows that, despite the target echoes integration, the resulting SINR did not improve because of a corresponding increase in the interference background level. Similarly, the P-NCI fails in enhancing the detection capability against the small maritime targets. For instance, for Speedboat 2, the performance of the P-NCI is much more comparable with that provided by the worst single-pol channel. In addition, it is worth noticing that a considerably higher number of false alarms appears in the considered range-velocity area. The inability to provide an effective control of the false alarm rate can be mostly attributed to the weakness of the hypothesis of statistical independence of the disturbance affecting the L different range-velocity maps. This especially applies to the case study under consideration since, in the absence of a prior disturbance cancellation stage, the observed interference is mainly due to the direct signal from the transmitter and its multipath replicas.

- The P-GLRT detection scheme (Figure 2.4(d)) yields the best performance thanks to its capability to adaptively reject the disturbance contribution based on the polarimetric information. Specifically, the P-GLRT allows to increase the number of correct detections with respect to both the best performing single-pol channel and the P-NCI, for all the three cooperative targets included in the analysis. This represents a clear advantage as it enhances the continuity of the obtained plot sequences that potentially simplifies a subsequent track initiation stage. Also, compared to P-NCI, P-GLRT allows to effectively control the false alarm rate. It is worth noticing that the plots formations outside the target trajectories are rarely due to the homogeneous background. They are rather due to the sidelobes of high power zero-Doppler contributions (severe multipath and/or interfering transmitters) or, eventually, to other targets of opportunity.

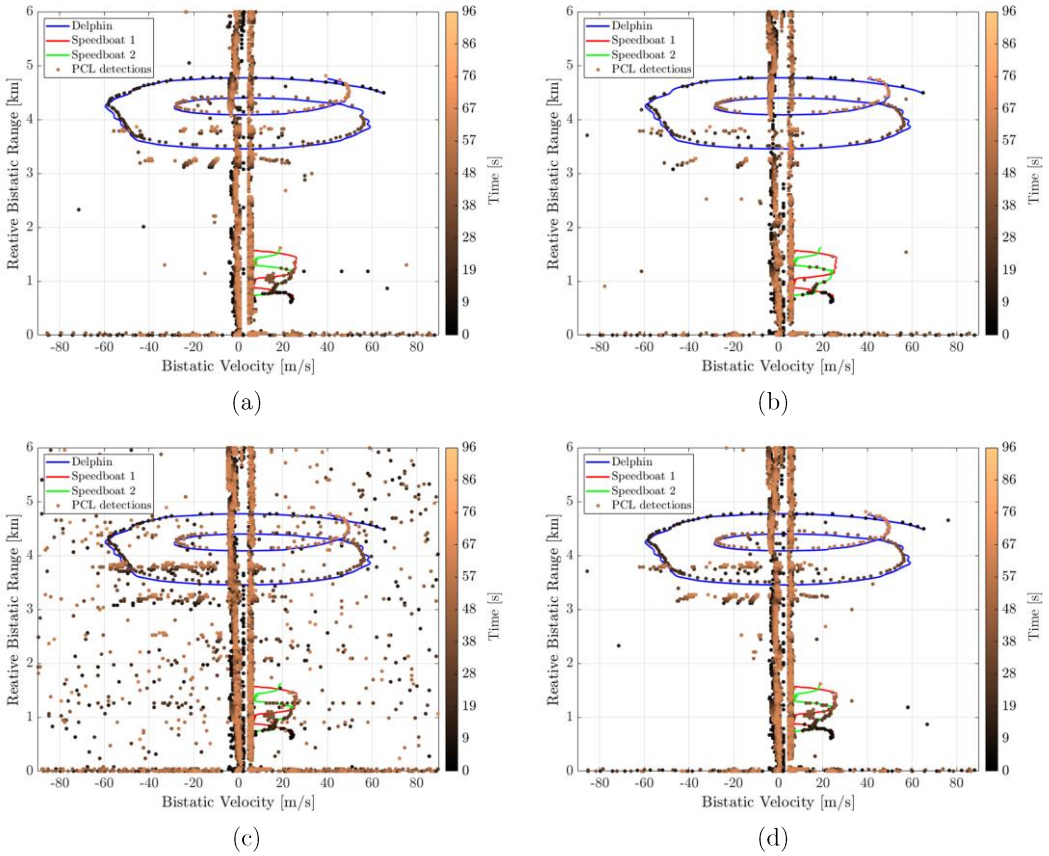

Figure 2.5: Detection results, after applying a 2-stage ECA-CD algorithm for $Pfa = 10^{-6}$ and dfferent detection schemes: (a) single-pol H, (b) single-pol V (c) P- NCI (d) P-GLRT

2.4.2.2 Results obtained after disturbance cancellation at each channel

Results analogous to those reported in Figure 2.4 and Table 2.3 are shown in Figure 2.5 and Table 2.4 when including the disturbance cancellation stage in the basic processing chain of the DVB-T based PCL system. Specifically, the disturbance cancellation has been implemented according to the ECA-CD approach.

Two stages of the algorithm were enough to mitigate the limited clutter Doppler spread mainly caused by the receiver platform slow motion. As is apparent, all the considered polarimetric detection schemes benefit from the prior cancellation stage separately applied at each polarimetric channel and thus provide improved performance with respect to the corresponding results discussed in Section 2.4.2.1. This is particularly evident for the speedboats' tracks that were almost entirely hidden behind the strong stationary disturbance, when not removed in a prior stage. This is quite apparent in Figure 2.6 that reports the range-velocity maps obtained for the single-pol H at a given scan. Specifically, in Figure 2.6 (a-b) the results are reported before and after applying a 2-stages ECA-CD, respectively.

Table 2.4
Number of correct detections with different polarimetric detection schemes and P_{fa} values after the application of a 2-stage ECA-CD.

	Delphin				Speedboat 1				Speedboat 2			
P_{fa}	single pol H	single pol V	P-NCI	P-GLRT	single pol H	single pol V	P-NCI	P-GLRT	single pol H	single pol V	P-NCI	P-GLRT
10^{-5}	143	125	144	152	36	17	32	42	56	25	46	59
10^{-6}	141	117	144	150	26	11	27	37	50	20	40	56
10^{-7}	137	109	139	149	24	7	25	31	46	18	38	51
10^{-8}	135	103	137	148	16	7	18	24	42	16	33	45

While Delphin appears as a strong peak in both cases (see the circles at approximately 4.4 km), the stationary disturbance severely masks the weak echoes of the speedboats that, at this scan, are located at approximately 0.6 km.

After the removal of the disturbance contributions around the zero Doppler, the speedboats yield isolated peaks that can be successfully detected against the low power level background. Therefore, when collecting the results at consecutive scans, a greater number of correct detections are obtained after the application of the ECA-CD with all the considered polarimetric schemes. Also, some of the undesired plots formations that were present in Figure 2.4 have been correctly removed in Figure 2.5 as they were probably originated by stationary disturbance contributions. Despite this overall improvement, the comparative analysis presented in sub-Section 2.4.2.1 among the different polarimetric detection schemes is entirely confirmed here. Specifically, the P-NCI still suffers from a limited capability of controlling the false alarm rate. In fact, even after the ECA-CD application, the presence of cancellation residuals of other sources of externally generated interference might jeopardize the hypothesis of uncorrelated disturbance contributions at the available polarimetric channels. The P-GLRT still offers the best results after the stationary disturbance has been strongly reduced. This underlines that, when avoiding the prior cancellation stage, the P-GLRT scheme has the potential to mitigate the strongest interference contribution caused by the direct signal and its multipath replicas.

On the other hand, when these contributions have been largely reduced by a dedicated processing stage, the P-GLRT approach still allows to enhance the resulting performance by counteracting possible cancellation residuals or other interference sources. In this regard, we report in Figure 2.7 the direct comparison of the results obtained with the single-pol operation (both H and V) after the 2-stage ECA-CD (see Figure 2.7 (a-b)) with the results of the P-GLRT either in the absence or after a prior cancellation stage (see Figure 2.7 (c-d)).

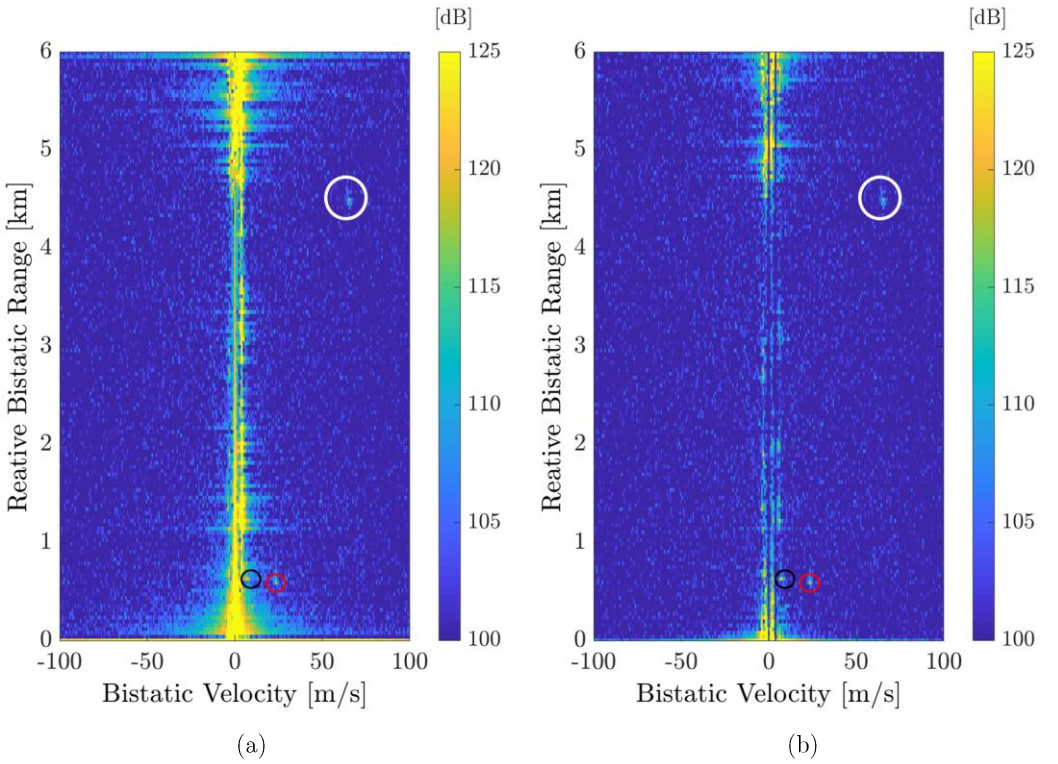

Figure 2.6: Range-velocity maps for single-pol H before thresholding: (a) without a 2-stage ECA-CD (b) after a 2-stage ECA-CD

In this case, the attention is focused on the correct detections only, so that the sequence of corresponding velocity measurements (black dots) is compared to the bistatic velocity tracks of the cooperative targets as a function of time. These figures allow to appreciate the continuity and the accuracy of the information provided by the PCL system employing different processing schemes. Incidentally, we observe that true target trajectories fluctuate due to the rough velocity estimation obtained via a differentiation of the range information provided by the GPS.

Based also on the comparison of the numerical results reported in Table 2.3 and Table 2.4, we observe that when the P-GLRT scheme is applied without any prior cancellation stage (Figure 2.7 (c)), it provides better detection performance against the aerial target than the single-pol channels after the application of a 2-stage ECA-CD. The advantage is tremendous with respect to the worst performing single-pol solution (i.e. single-pol V in Figure 2.7 (b)).

In such a case, the polarimetric adaptive approach operating on the range-velocity map may constitute a valid alternative to the application of a cancellation stage in the signal domain. Clearly, the same conclusion cannot be drawn with reference to the small maritime targets as, in that case, the cancellation stage is strictly required for them to be detected with a reasonable detection probability. In such conditions, the additional disturbance rejection capability intrinsically provided by the P-GLRT might be a critical point.

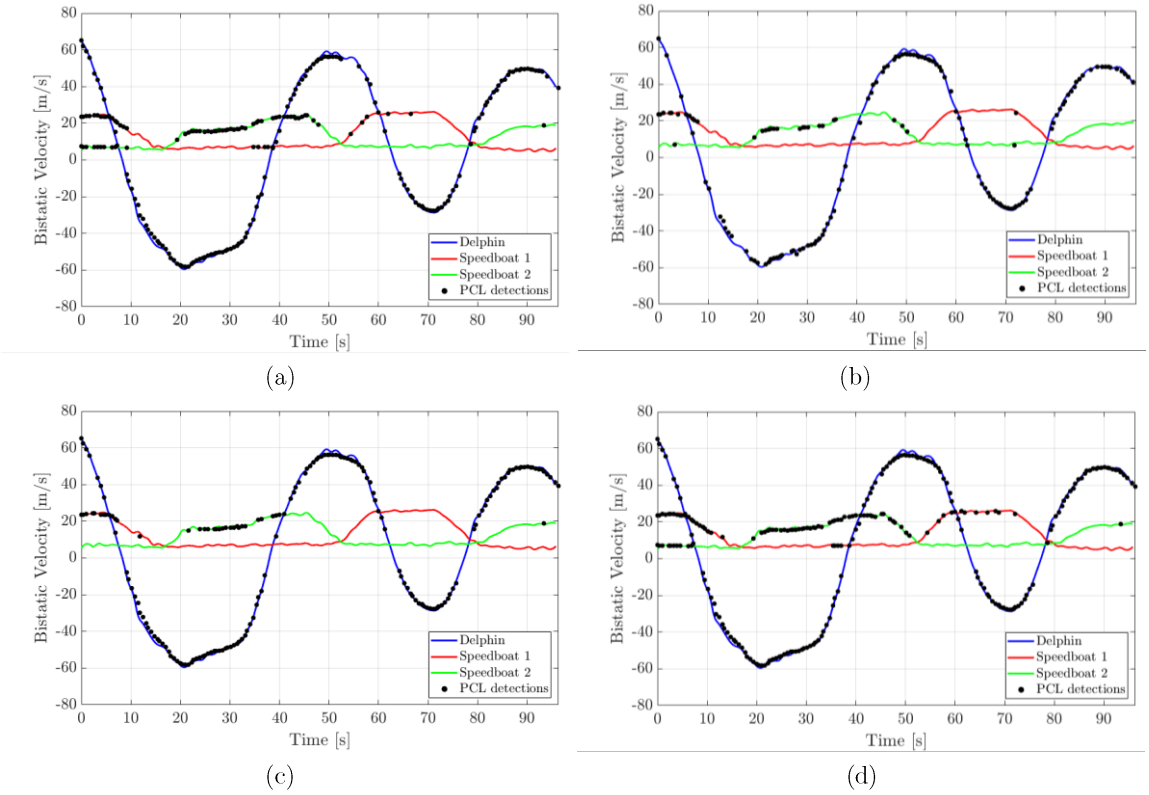

Figure 2.7: Correct detections in the bistatic velocity-time domain for $Pfa = 10^6$ with: (a) single-pol H after a 2-stages ECA-CD (b) single-pol V after a 2-stages ECA-CD (c) P-GLRT without any prior cancellation stage, (d) P-GLRT after a 2-stages ECA-CD

Comparing Table 2.3 and Table 2.4 it is apparent that the P-GLRT allows to increase the number of correct detections with respect to the best single-pol channel. For instance, with $Pfa = 10^6$, an increase of 42% and 12% is observed against Speedboat 1 and Speedboat 2, respectively.

If compared to the worst performing single-pol channel, the number of correct detections against the maritime targets is always more than tripled for Speedboat 1 and more than doubled for Speedboat 2. The advantage of the P-GLRT is even more apparent if we observe that, in practical cases, it is difficult to identify an effective way of a priori establishing the best antenna polarization to be employed.

2.5 Summary

In this Chapter, the feasibility of a polarimetric operation is considered for passive radar exploiting DVB-T transmitters as IOs. The results obtained using experimental data sets including cooperative targets allowed to prove the effectiveness of the locally adaptive approach to jointly exploit the information provided by two cross-polarized surveillance

antennas. In particular, we showed that the considered P-GLRT detection scheme is able to effectively exploit the polarimetric information to reject the disturbance thus leading to a remarkable target detection improvement.

However, the considered detection strategy exploits the polarimetric information after the entire basic PCL processing has been separately applied to the signals collected by differently polarized antennas. Therefore, building upon this promising results, we aim at deriving a novel polarimetric target detection scheme in the next Chapters.

Chapter 3
Polarimetric adaptive target detector based on a multi-channel AR model: Derivation and Performance Analysis

In this Chapter, we deal with the problem of target detection in coherent radar systems exploiting polarimetric diversity. We resort to a parametric approach and we model the disturbance affecting the data as a multi-channel AR process. Following this model, a new polarimetric adaptive detector is derived, which aims at improving the target detection capability while relaxing the requirements on the training data size and the computational burden with respect to existing solutions. A complete theoretical characterization of the asymptotic performance of the derived detector is provided, using two different target fluctuation models. The effectiveness of the proposed approach is shown against simulated data, in comparison with alternative existing solutions.

In Section 3.1 prior work on polarimetric adaptive detector is detailed. The proposed AR model based polarimetric adaptive detection scheme is derived in Section 3.2. The asymptotic performance of the proposed detector are illustrated in Section 3.3 while an extensive numerical analysis is reported in Section 3.4 to assess the performance of the derived detection strategy. Finally, concluding remarks are given in Section 3.5 while mathematical details are reported in Appendices A-D.

3.1 Fully adaptive polarimetric detectors

Let us consider a polarimetric radar system that collects signals from L polarimetric channels. These are typically obtained by exploiting multiple receiving channels connected to differently polarized antenna elements. A quite typical case is attained by exploiting two linearly cross-polarized antennas, making $L = 2$ polarimetric channels available. The number of equivalent polarimetric channels can be further increased if the transmitter is able to emit signals using different polarizations. For instance, by alternatively transmitting bursts of radar pulses at the two linear polarizations (H and V) and simultaneously collecting the corresponding back-scattered echoes at both polarizations, a maximum of $L = 4$ polarimetric

channels can be obtained in a pulse radar, namely HH, VV, HV and VH channels. Assuming reciprocity between HV and VH returns [76], the number of independent channels is $L = 3$.

In general, we arrange in a L–dimensional vector $\mathbf{x_0}(m)$ the samples collected at the L available polarimetric channels at the m-th temporal observation:

$$\mathbf{x_0}(m) = \left[x_0^{(0)}(m) \dots x_0^{(1)}(m) \dots x_0^{(L-1)}(m)\right]^T \tag{3.1}$$

In this work, temporal observations might refer to consecutive pulses emitted by a pulse radar transmitter; in this case the samples are extracted at a given range cell after an appropriate range compression stage, e.g. matched filter. Alternatively, they might refer to samples of the backscattered echo signal for a continuous wave radar transmission. The subscript '0' in (3.1) refers to primary data, namely the data in which the detection of a target echo is sought. In fact, $\mathbf{x_0}(m)$ is the sum of a useful target component $\mathbf{s}(m)$ and a vector $\mathbf{d}(m)$ collecting the disturbance contributions, which might include clutter and noise:

$$\mathbf{x_0}(m) = \varrho\mathbf{s}(m) + \mathbf{d}(m) \tag{3.2}$$

being $\varrho = 0$ under the null hypothesis H_0 (target absent) and $\varrho = 1$ under the alternate H_1 hypothesis (target present).

We arrange M consecutive temporal observations in a $LM\times1$ vector

$$\mathbf{x_0} = [\mathbf{x}_0^H(0)\ \mathbf{x}_0^H(1) \dots \mathbf{x}_0^H(M-1)]^H \tag{3.3}$$

Following (3.2), it can be decomposed as $\mathbf{x_0} = \varrho\mathbf{s} + \mathbf{d}$, where $\mathbf{s}$ and $\mathbf{d}$ are arranged as $\mathbf{x_0}$. Specifically, the target component can be written as:

$$\mathbf{s} = \mathbf{t} \otimes \boldsymbol{\alpha} \tag{3.4}$$

where

- $\mathbf{t}$ is the vector of expected temporal returns for a unit amplitude target echo. It is assumed known at the receiver; however, its definition depends on the employed radar system. For an active radar system exploiting a coherent train of M pulses, $\mathbf{t}$ is typically referred to as the temporal steering vector and it is given by $\mathbf{t} = \left[1, e^{-j2\pi f_d}, \dots, e^{-j2\pi(M-1)f_d}\right]^H$, being f_d the target Doppler frequency normalized to the pulse repetition frequency (PRF). In contrast, when a continuous wave (CW) radar is considered and the temporal observations represent consecutive samples of the backscattered echo, $\mathbf{t}$ might include a M-samples fragment of the transmitted signal.
- $\boldsymbol{\alpha} = [\alpha_0, \dots, \alpha_{L-1}]^T$ contains the unknown complex target amplitudes at the different polarimetric channels. As is apparent, a partially structured model is assumed for the

target. In fact, its returns are assumed to be known up to an unknown amplitude in the temporal domain, namely at the l-th polarimetric channel, $l = 0, \ldots, L-1$, they are obtained as $\boldsymbol{\alpha}_l \mathbf{t}$, with known $\mathbf{t}$. In contrast, target returns involve unknown nonlinear parameters in the polarimetric domain, being the target echoes at a given time instant provided by $\mathrm{t}_m \boldsymbol{\alpha}$, $m = 0, \ldots, M-1$, with unknown $\boldsymbol{\alpha}$.

Vector $\mathbf{x_0}$ is typically modelled as a complex Gaussian random vector with covariance matrix $\mathbf{M}$, zero mean vector under the null hypothesis H_0 and mean vector $\mathbf{s}$ under the alternate hypothesis H_1, i.e. $\mathbf{x_0}|_{H_\varrho} \sim \mathcal{CN}(\varrho\mathbf{s},\mathbf{M})$.

The $LM \times LM$ covariance matrix $\mathbf{M}$ encodes the polarimetric and spectral characteristics of the disturbance affecting the received vector and it has a block structure:

$$\mathbf{M} = \begin{bmatrix} \mathbf{M}_{0,0} & \cdots & \mathbf{M}_{0,M-1} \\ \vdots & \ddots & \vdots \\ \mathbf{M}_{M-1,0} & \cdots & \mathbf{M}_{M-1,M-1} \end{bmatrix} \tag{3.5}$$

where the generic $L \times L$ block $\mathbf{M}_{m,p}$ is the cross-covariance matrix of the polarimetric vectors extracted at times m and p, namely $\mathbf{M}_{m,p} = \{\mathbf{x_0}(m)\mathbf{x_0}^H(p)|H_0\}$.
As is well known, under these hypotheses and assuming the covariance matrix $\mathbf{M}$ known, the optimum detection test, referred to as the polarimetric matched filter (Pol-MF), is obtained as [26]

$$T_{Pol\text{-}MF} = \mathbf{x_0}^H \mathbf{M}^{-1}\mathbf{T}[\mathbf{T}^H\mathbf{M}^{-1}\mathbf{T}]^{-1}\mathbf{T}^H\mathbf{M}^{-1}\mathbf{x_0} \underset{H_0}{\overset{H_1}{\gtrless}} \eta_{MF} \tag{3.6}$$

where η_{MF} is the detection threshold and $\mathbf{T} = \mathbf{t} \otimes \mathbf{I}_L$.

However, adaptive approaches must be considered to obtain a practical receiver for real radar scenarios where the covariance matrix is unknown. To this end, along with the primary data $\mathbf{x_0}$, the authors in [26] and [82] assume a set of P vectors $\mathbf{x}_p$, $p = 1, \ldots, P$, to be available, referred to as secondary (or training) data. They are assumed target-free, independent and identically distributed (i.i.d), sharing the same statistic of $\mathbf{x_0}$ under the H_0 hypothesis.

Two different adaptive detection schemes can be obtained by resorting to either a two-stage GLRT strategy or a plain GLRT approach. Specifically, in the former case, the detection test is obtained by substituting in (3.5) the ML estimate of the covariance matrix based upon P secondary data, namely $\widehat{\mathbf{M}} = \frac{1}{P}\sum_{p=1}^{P} \mathbf{x}_p \mathbf{x}_p^H$, thus writing [26]:

$$T_{Pol\text{-}AMF} = \mathbf{x_0}^H \widehat{\mathbf{M}}^{-1}\mathbf{T}\left[\mathbf{T}^H\widehat{\mathbf{M}}^{-1}\mathbf{T}\right]^{-1}\mathbf{T}^H\widehat{\mathbf{M}}^{-1}\mathbf{x_0} \underset{H_0}{\overset{H_1}{\gtrless}} \eta_{AMF} \tag{3.7}$$

where η_{AMF} is a properly modified detection threshold. This will be referred in the following as the polarimetric adaptive matched filter (Pol-AMF).
Alternatively, by resorting to the plain GLRT approach, the polarimetric GLRT (Pol-GLRT) has been derived in [82] and [83] as

$$T_{Pol\text{-}GLRT} = \frac{\mathbf{x}_0^H \widehat{\mathbf{M}}^{-1}\mathbf{T}\left[\mathbf{T}^H \widehat{\mathbf{M}}^{-1}\mathbf{T}\right]^{-1}\mathbf{T}^H \widehat{\mathbf{M}}^{-1}\mathbf{x}_0}{P + \mathbf{x}_0^H \widehat{\mathbf{M}}^{-1}\mathbf{x}_0} = \frac{T_{Pol-AMF}}{P + \mathbf{x}_0^H \widehat{\mathbf{M}}^{-1}\mathbf{x}_0} \underset{H_0}{\overset{H_1}{\gtrless}} \eta_{GLRT} \tag{3.8}$$

η_{GLRT} being the detection threshold that guarantees the desired false alarm probability.

As it is apparent, the above detectors adaptively exploit all the available degrees of freedom to perform the whitening of the data $\mathbf{x_0}$ in both the polarimetric and temporal domains. While being theoretically optimum under the assumption of *a priori* known disturbance characteristics, this approach might be computationally intensive and might suffer of significant adaptivity loss in practical cases, especially when a limited number of training data is made available. As is well known, a number of secondary data $P \geq 2ML$ is required for the aforementioned adaptive detectors to yield limited adaptivity loss. This could result in severe limitations when L and M are large, as it may be difficult to obtain the required amount of training data with the desired characteristics (target-free and i.i.d).

To overcome these issues, in the next Section we exploit a parametric method to develop a new polarimetric adaptive detector by modelling the disturbance as a multi-channels AR process.

3.2 AR model based Polarimetric Adaptive Detector

One effective way to reduce the computational load and training data size requirements is to model the disturbance as a multi-channel AR process and exploit it for the development of the target detection test. This approach has been effectively applied in several radar applications including STAP and other array processing applications. Here this approach is employed to the considered polarimetric radar where the multi-channel system is intended to capture the polarimetric information from both the target and the competing disturbance. Specifically, the adopted disturbance model is described in sub-Section 3.2.1. This is then exploited in sub-Section 3.2.2 to derive the GLRT detection test based on primary data only, namely by assuming known the disturbance parameters. Finally, the AR–based adaptive detection test is presented in sub-Section 3.2.3, based on the result in 3.2.2 and a two-stage GLRT approach.

3.2.1 Multi-channel Auto-regressive Model

We model the disturbance as a L–channel AR process of known order $Q - 1$, denoted as

AR $(Q-1)$ and exploit it for signal detection. Accordingly, the vector random process $\mathbf{d}(m)$ satisfies the following relation [99]:

$$\mathbf{d}(m) = \sum_{q=1}^{Q-1} \mathbf{A}^H(q)\mathbf{d}(m-q) + \mathbf{w}(m) \tag{3.9}$$

where $\{\mathbf{A}(q)\}_{q=1}^{Q-1}$ are complex-valued $L \times L$ matrix parameters encoding the regression coefficients at different polarimetric channels, and $\mathbf{w}(m) \sim \mathcal{CN}(\mathbf{0},\mathbf{R})$ is the driving white noise sequence, $\mathbf{R}$ being the $L \times L$ polarimetric covariance matrix. Note that the single-channel AR model has been widely adopted in radar signal processing. For instance, different authors demonstrated that it can be used to reasonably approximate the spectral characteristics of different types of clutter [38],[48],[59],[86],[112], e.g. sea, ground, atmospheric. In this work, we extend this model by also considering the existing correlation between the available polarimetric channels. The model in (3.9) will be used in this paper for the theoretical derivation of an appropriate detector. Then, its suitability in practical applications will be verified in Chapter 4 and Chapter 5 against both simulated and experimental data. Based on this model, the approximate (actually conditional) probability density function (pdf) of the data [15],[57],[58],[97] under the H_0 hypothesis can be written as:

$$\begin{aligned} f_0\left(\mathbf{x}_0 \middle| \mathbf{R}, \{\mathbf{A}(q)\}_{q=1}^{Q-1}\right) &= (\pi^L |\mathbf{R}|)^{-(M-Q+1)} \\ &\times \exp\left\{ -\sum_{m=Q}^{M} \left[\mathbf{x}_0(m) - \sum_{q=1}^{Q-1} \mathbf{A}^H(q)\, \mathbf{x}_0(m-q) \right] \mathbf{R}^{-1} \left[\mathbf{x}_0(m) \right.\right. \\ &\left.\left. - \sum_{q=1}^{Q-1} \mathbf{A}^H(q)\, \mathbf{x}_0(m-q) \right]^H \right\} \end{aligned} \tag{3.10}$$

We note that the conditional pdf in (3.10) well approximates the actual pdf of the data for the large-sample case [15],[58]. Therefore, as in [102], we use (3.10) in the following to derive the sought detector and to perform the ML estimation of the AR parameters. A similar expression can be provided under H_1, by replacing each instance of $\mathbf{x}_0(m)$ with $\mathbf{x}_0(m) - \mathbf{s}(m)$. To simplify the notation, we arrange the matrix parameters of the AR$(Q-1)$ process in a $L(Q-1) \times L$ matrix $\mathbf{A} = [\mathbf{A}^H(Q-1)\ \mathbf{A}^H(Q-2)\ \ldots\ \mathbf{A}^H(1)]^H$. In addition, we define the vectors $\tilde{\mathbf{x}}_0(m) = [\mathbf{x}_0^H(m)\ \mathbf{x}_0^H(m+1) \ldots \mathbf{x}_0^H(m+Q-1)]^H$, $m = 0, \ldots, M-Q$, which collect Q consecutive snapshots of the data starting from the m-th sample. Finally, we arrange these vectors into matrix $\mathbf{X}_0(LQ \times L\ (M-Q-1))$

$$\mathbf{X}_0 = [\tilde{\mathbf{x}}_0(0)\ \tilde{\mathbf{x}}_0(1)\ \ldots\ \tilde{\mathbf{x}}_0(M-Q)] \tag{3.11}$$

The same definitions are extended to the target components, yielding the following matrix structures:

$$\mathbf{S} = [\tilde{\mathbf{s}}(0)\ \tilde{\mathbf{s}}(1)\ \dots\ \tilde{\mathbf{s}}(M-Q)] \tag{3.12}$$

$$\tilde{\mathbf{s}}(m) = [\mathbf{s}^H(m)\ \ \mathbf{s}^H(m+1) \dots \mathbf{s}^H(m+Q-1)]^H = \tilde{\mathbf{t}}(m) \otimes \boldsymbol{\alpha} \tag{3.13}$$

where $\tilde{\mathbf{t}}(m)$ collects a Q-dimensional sub-vector of the temporal steering vector starting from the m-th sample. Consequently, the likelihood of the data under hypothesis H_ϱ ($\varrho = 0,1$) can be rewritten as:

$$\begin{aligned} f_\gamma(\mathbf{X}_0|\ \gamma\boldsymbol{\alpha}, \mathbf{R}, \mathbf{A}) = (\pi^L|\mathbf{R}|)^{-(M-Q+1)} \\ \times \exp\{-\mathrm{tr}[(\mathbf{X}_0 - \gamma\mathbf{S})^H \mathbf{P}\ (\mathbf{X}_0 - \gamma\mathbf{S})]\} \end{aligned} \tag{3.14}$$

Where $\mathbf{P} = \mathbf{H}^H\mathbf{R}^{-1}\mathbf{H}$, $\mathbf{H} = [-\mathbf{A}^H \quad \mathbf{I}_L]$, and tr $(\cdot)$ denotes the trace of the matrix.

3.2.2 AR model based Polarimetric Matched Filter

We derive the polarimetric adaptive detector by resorting to a two-step GLRT design criterion. Specifically, in this Section we assume that the parameters of the AR $(Q-1)$ model, say **R** and **A,** are known, and we derive the GLRT detection test based on primary data. Then, in the next sub-Section, a fully adaptive detector is obtained by replacing the unknown matrices with their ML estimates.

The test statistic of the GLRT based solely on primary data is given by:

$$\frac{\max_{\boldsymbol{\alpha}}\{f_1(\mathbf{X}_0|\ \boldsymbol{\alpha}, \mathbf{R}, \mathbf{A})\}}{f_0(\mathbf{X}_0|\mathbf{R}, \mathbf{A})} \underset{H_0}{\overset{H_1}{\gtrless}} \eta_0 \tag{3.15}$$

where η_0 is the detection threshold.

By maximizing the numerator over $\boldsymbol{\alpha}$ and after some algebraic manipulations (see Appendix A), we obtain the following test statistic:

$$\begin{aligned} T_{Pol-AR-MF} = 2 \sum_{m=0}^{M-Q} \tilde{\mathbf{x}}_0^H(m)\ \mathbf{P}\ \boldsymbol{\Sigma}(m) \left[\sum_{m=0}^{M-Q} \boldsymbol{\Sigma}^H(m)\mathbf{P}\ \boldsymbol{\Sigma}(m)\right]^{-1} \\ \times \sum_{m=0}^{M-Q} \boldsymbol{\Sigma}^H(m)\ \mathbf{P}\ \tilde{\mathbf{x}}_0(m) \underset{H_0}{\overset{H_1}{\gtrless}} \eta_{AR-MF} \end{aligned} \tag{3.16}$$

where $\boldsymbol{\Sigma}(m) = \tilde{\mathbf{t}}(m) \otimes \mathbf{I}_L$. The detection scheme in (3.16) will be referred to in the following as the polarimetric AR model based matched filter (Pol-AR-MF).

The test statistic above can be interpreted by defining the matrices $\mathbf{W} = \sum_{m=0}^{M-Q} \boldsymbol{\Sigma}^H(m)\mathbf{P}\boldsymbol{\Sigma}(m)$ and $\mathbf{V}(m) = \mathbf{P}\boldsymbol{\Sigma}(m)$, $m = 0, \ldots, M-Q$, which allows us to rewrite (3.16) as:

$$T_{Pol-AR-MF} = 2 \sum_{m=0}^{M-Q} \tilde{\mathbf{x}}_0^H(m)\, \mathbf{V}(m)\, \mathbf{W}^{-1} \sum_{m=0}^{M-Q} \mathbf{V}^H(m)\, \tilde{\mathbf{x}}_0(m) \underset{H_0}{\overset{H_1}{\gtrless}} \eta_{AR-MF} \tag{3.17}$$

We observe that $\mathbf{V}(m)$ ($LQ \times L$) includes the filter coefficients to be applied at the m-th sub-CPI to obtain the temporally whitened sequence of L–dimensional vectors $\mathbf{y}_0(m) = \mathbf{V}^H(m)\tilde{\mathbf{x}}_0(m)$, $m = 0, \ldots, M-Q$. The summation across consecutive samples provides the coherent integration of target echoes in time domain, which yields $\mathbf{z}_0 = \sqrt{2}\sum_{m=0}^{M-Q} \mathbf{y}_0(m)$. Notice that, assuming a block based implementation of the detection scheme, the exploitation of an order $Q-1$ for the AR model implies a loss of $Q-1$ samples on the sequence $\mathbf{y}_0(m)$ namely the summation is limited to $M-Q+1$ samples. This might be responsible of limited loss as observed in the results reported in Section 3.4. However, other implementations are possible based on lattice filters operating across the slow time.

Finally, the test statistic is evaluated as $T_{Pol\text{-}AR\text{-}MF} = \mathbf{z}_0{}^H \mathbf{W}^{-1} \mathbf{z}_0$ that encodes the polarimetric whitening followed by the non-coherent integration of target echoes across the polarimetric channels. This is a direct consequence of the partially unstructured model adopted for the target component (see (3.4) and subsequent positions).

Notice that, if $\mathbf{t}$ represents the temporal steering vector, namely the vector that encodes the target echo phase shifts across consecutive radar pulses, we can rework and simplify the expression in (3.17). To this purpose, we observe that $\tilde{\mathbf{t}}(m) = e^{j2\pi f_d m}\, \tilde{\mathbf{t}}(0)$ and, consequently, we can write:

$$\begin{aligned} T_{Pol-AR-MF} = 2 &\sum_{m=0}^{M-Q} e^{j2\pi f_d m}\, \tilde{\mathbf{x}}_0^H(m)\mathbf{V}(0)\, \mathbf{W}^{-1} \\ &\times \sum_{m=0}^{M-Q} e^{-j2\pi f_d m}\, \mathbf{V}^H(0)\tilde{\mathbf{x}}_0(m) \underset{H_0}{\overset{H_1}{\gtrless}} \eta_{AR-MF} \end{aligned} \tag{3.18}$$

where $\mathbf{W} = (M-Q+1)\, \boldsymbol{\Sigma}^H(0)\mathbf{P}\boldsymbol{\Sigma}(0)$. Therefore, in this case, a constant filter can be applied to obtain the whitened sequence $\mathbf{y}_0'(m) = \mathbf{V}^H(0)\tilde{\mathbf{x}}_0(m)$, provided that the phase shift across consecutive sub-CPIs is compensated for before coherent integration. The above simplification also allows an alternative implementation of the temporal whitening stage as

the filtering by matrix $\mathbf{V}(0)$ and the summation could be performed in reverse order to limit the computational burden.

As a last remark, we notice that the test statistic in (3.17) can be expressed as a quadratic form in $\mathbf{x_0}$ as:

$$T_{Pol-AR-MF} = \mathbf{x}_0^H \mathbf{B}\,\mathbf{C}\,\mathbf{C}^H\mathbf{B}^H\mathbf{x}_0 \underset{H_0}{\overset{H_1}{\gtrless}} \eta_{AR-MF} \tag{3.19}$$

where

$$\mathbf{B} = [\mathbf{B}_0\,\mathbf{B}_1\,\ldots\,\mathbf{B}_{M-Q}]$$

$$\text{with } \mathbf{B}_m = \begin{bmatrix} \mathbf{0}_{Lm\times L} \\ \mathbf{V}(m) \\ \mathbf{0}_{L(M-Q-m)\times L} \end{bmatrix} \quad m = 0, \ldots, M-Q \tag{3.20}$$

$$\mathbf{C} = \sqrt{2}(\mathbf{1}_{M-Q+1\times 1} \otimes \mathbf{W}^{-\frac{1}{2}}) \tag{3.21}$$

Under the assumptions adopted in (3.18), the blocks of matrix $\mathbf{B}$ are shifted versions of the first block, being the shift by L elements row-wise, whereas $\mathbf{C} = \sqrt{2}(\bar{\mathbf{t}} \otimes \mathbf{W}^{-\frac{1}{2}})$ where $\bar{\mathbf{t}}$ includes the first $M-Q+1$ elements of the steering vector $\mathbf{t}$.

3.2.3 Adaptive implementation

To make the derived detector fully adaptive, matrix $\mathbf{P}$, and hence matrices $\mathbf{A}$ and $\mathbf{R}$, must be replaced with their ML estimates. These are obtained from the secondary data $\mathbf{x}_p$, $p = 1, \ldots, P$, for which the same assumption adopted in Section 3.1 hold (i.i.d. and target free). Specifically, in this case we assume that the disturbance in the secondary data follows an AR $(Q-1)$ model with same parameters of the disturbance affecting the primary data. By applying the same reordering strategy as for $\mathbf{X}_0$ (see (3.11)) to the secondary data vectors, we obtain P matrices $\mathbf{X}_p$, $p = 1, \ldots, P$, that are then collected in a larger matrix $\overline{\mathbf{X}} = [\mathbf{X}_1 \ldots \mathbf{X}_P]$ of dimensions $QL\times P(M-Q+1)$. The joint likelihood of the secondary data is then written as:

$$f_0(\overline{\mathbf{X}}|\,\mathbf{R},\mathbf{A}) = (\pi^L|\mathbf{R}|)^{-P(M-Q+1)} \exp\{-\text{tr}(\overline{\mathbf{X}}^H\mathbf{P}\overline{\mathbf{X}})\} \tag{3.22}$$

Based on (3.22), proper approximation of the ML estimates of $\mathbf{A}$ and $\mathbf{R}$ are readily obtained as (see Appendix B):

$$\widehat{\mathbf{A}} = \widehat{\mathbf{Q}}_{00}^{-1}\widehat{\mathbf{Q}}_{01} \tag{3.23}$$

and

$$\widehat{\mathbf{R}} = \frac{1}{P(M-Q+1)}\left(\widehat{\mathbf{Q}}_{11} - \widehat{\mathbf{Q}}_{01}^{H}\widehat{\mathbf{Q}}_{00}^{-1}\widehat{\mathbf{Q}}_{01}\right) \tag{3.24}$$

where $\widehat{\mathbf{Q}}_{00}$ $(L(Q-1) \times L(Q-1))$, $\widehat{\mathbf{Q}}_{01}$ $(L(Q-1)\times L)$, $\widehat{\mathbf{Q}}_{11}$ $(L\times L)$ are blocks of the following matrix:

$$\widehat{\mathbf{Q}} = \overline{\mathbf{X}}\,\overline{\mathbf{X}}^{H} = \begin{bmatrix} \widehat{\mathbf{Q}}_{00} & \widehat{\mathbf{Q}}_{01} \\ \widehat{\mathbf{Q}}_{01}^{H} & \widehat{\mathbf{Q}}_{11} \end{bmatrix} \tag{3.25}$$

Notice that a similar result was obtained in several works, e.g. [32],[62],[102], since this is independent of the adopted model for the target components.

We observe that the $LQ\times LQ$ matrix $\widehat{\mathbf{Q}}$ represents an estimate of the disturbance covariance matrix within a sub-CPI, namely any $LQ\times LQ$ block on the main diagonal of matrix $\mathbf{M}$. This benefits from a joint average over secondary data and consecutive (overlapped) sub-CPIs within the CPI:

$$\widehat{\mathbf{Q}} = \sum_{p=1}^{P}\sum_{m=0}^{M-Q} \tilde{\mathbf{x}}_p(m)\tilde{\mathbf{x}}_p^{H}(m) \tag{3.26}$$

The need for a smaller number of parameters to be estimated and the possibility to improve the estimation stage based on consecutive temporal observations formed within the CPI allow to limit the adaptivity loss compared to the detection schemes in Section 3.1 [26],[82].

By using (3.23) and (3.24) in (3.16), we obtain the test statistic for the polarimetric AR model based adaptive matched filter (Pol-AR-AMF) as

$$\begin{aligned} T_{Pol-AR-AMF} = 2 &\sum_{m=0}^{M-Q} \tilde{\mathbf{x}}_0^{H}(m)\,\widehat{\mathbf{P}}\,\boldsymbol{\Sigma}(m) \left[\sum_{m=0}^{M-Q} \boldsymbol{\Sigma}^{H}(m)\widehat{\mathbf{P}}\,\boldsymbol{\Sigma}(m)\right]^{-1} \\ &\times \sum_{m=0}^{M-Q} \boldsymbol{\Sigma}^{H}(m)\,\widehat{\mathbf{P}}\,\tilde{\mathbf{x}}_0(m) \underset{H_0}{\overset{H_1}{\gtrless}} \eta_{AR-AMF} \end{aligned} \tag{3.27}$$

being $\widehat{\mathbf{P}} = \widehat{\mathbf{H}}^{H}\widehat{\mathbf{R}}^{-1}\widehat{\mathbf{H}}$ and $\widehat{\mathbf{H}} = [-\widehat{\mathbf{A}}^{H} \quad \mathbf{I}_L]$. Similarly, the adaptive versions of the test statistics in (3.18)-(3.19) can be easily obtained.

3.3 Asymptotic Performance

In this Section, we derive the asymptotic performance achievable with the proposed detector, i.e. under the assumption that $\widehat{\mathbf{A}}$ and $\widehat{\mathbf{R}}$ are asymptotic estimates obtained from an infinite number of secondary data. Basically, we neglect the adaptivity loss due to the estimate fluctuations and, provided that the pdf in (3.10) correctly approximates the actual pdf of the

data for the large-sample case, we assume that the asymptotic ML estimates of $\mathbf{A}$ and $\mathbf{R}$ coincide with the actual values of the AR parameters. This analysis is useful since it might be representative of the performance of its adaptive version for large number of training data.

3.3.1 False alarm probability

Let us consider the test statistic in (3.19) and define the L-dimensional vector $\check{\mathbf{z}}_0 = \mathbf{C}^H\mathbf{B}^H\mathbf{x}_0$, namely $\check{\mathbf{z}}_0$ represents the data after both polarimetric and temporal whitening, which then undergoes the non-coherent integration across the polarimetric channels and the test statistic in (3.19) can be written as $T_{Pol-AR-MF} = \|\check{\mathbf{z}}_0\|^2$.

If the input disturbance process exactly matches the AR $(Q - 1)$ model exploited for the derivation of the proposed detector, the filtering of data $\mathbf{x}_0$ via matrices $\mathbf{B}$ and $\mathbf{C}$, based on asymptotic estimates of the relevant parameters included therein, provides a perfect whitening in both the polarimetric and the temporal domain. Under the H_0 hypothesis, $\check{\mathbf{z}}_0$ is a complex Gaussian random vector with zero-mean and covariance matrix $2\mathbf{I}_L$, i.e. $\check{\mathbf{z}}_0|_{H_0} \sim \mathcal{CN}(\mathbf{0}_{L\times 1},\ 2\mathbf{I}_L)$. See Appendix C for demonstration. Therefore, the asymptotic distribution of the test statistic of the adaptive detector is given by

$$T_{Pol-AR-AMF} \xrightarrow{asymp.} T_{Pol-AR-MF} \sim \chi^2_{2L}(0) \tag{3.28}$$

where $\chi^2_{2L}(0)$ denotes the central Chi-squared distribution with $2L$ degrees of freedom. Correspondingly, we can write the asymptotic false alarm probability Pfa as

$$P_{fa} = \sum_{l=0}^{L-1} \frac{\eta^l}{2^l\,\Gamma(L-l)} e^{-\frac{\eta}{2}} \tag{3.29}$$

where $\Gamma(\cdot)$ is the Gamma function and η is the threshold that guarantees the desired Pfa. Eq. (3.29) gives an exact threshold η_{AR-MF} for the clairvoyant detector in (3.19) whereas, as the number P of secondary data increases, it provides a good approximation of the threshold η_{AR-AMF} to be adopted for the adaptive detector in (3.27).

The asymptotic distribution of $T_{Pol-AR-AMF}$ under H_0 is independent of the unknown parameters. Consequently, the Pfa in (3.29) depends only on the test threshold and the number of polarimetric channels, which are design parameters. It is then evident that the proposed detector asymptotically exhibits the CFAR property.

3.3.2 Detection Probability

A. Non-fluctuating target model (Swerling 0)

For a non-fluctuating target model, namely a Swerling 0 target [109], and assuming know the disturbance parameters, vector $\check{\mathbf{z}}_0$ under hypothesis H_0 is a complex Gaussian random vector,

with mean vector $\boldsymbol{\upsilon} = \mathbf{C}^H\mathbf{B}^H\mathbf{s}$ and covariance matrix $2\mathbf{I}_L$, i.e. $\check{\mathbf{z}}_0|_{H_1} \sim \mathcal{CN}(\boldsymbol{\upsilon}, 2\mathbf{I}_L)$, and the asymptotic distribution of the test statistic is given by

$$T_{Pol-AR-AMF} \xrightarrow{asymp.} T_{Pol-AR-MF} \sim \chi^2_{2L}(\varsigma) \tag{3.30}$$

where $\chi^2_{2L}(\varsigma)$ denotes the noncentral Chi-squared distribution with $2L$ degrees of freedom and noncentrality parameter $\varsigma = \sum_{l=0}^{L-1}|\upsilon_l|^2 = \|\boldsymbol{\upsilon}\|^2$. From (3.30), we can write the asymptotic detection probability Pd expression using the Marcum Q-function, as follows

$$P_d = Q_L\left(\sqrt{\varsigma}, \sqrt{\eta}\right) = \int_{\sqrt{\eta}}^{\infty} x\left(\frac{x}{\sqrt{\varsigma}}\right)^{L-1} \exp\left(-\frac{x^2+\varsigma}{2}\right) I_{L-1}\left(\sqrt{\varsigma}x\right) dx \tag{3.31}$$

$I_{L-1}\left(\sqrt{\varsigma}x\right)$ being the modified Bessel function of order $L-1$.

Eqs. (3.31) and (3.29) extend the results in [56] that were obtained for the case of a structured model for the space-time target components. That model basically yields a coherent summation over the whitened sequences and, in turn, results in a $\chi^2_2(\varrho\varsigma)$ asymptotic distribution for the test statistic under $H_\varrho\,(\varrho = 0,1)$.

B. Fluctuating target model (Swerling I)

Assuming a Swerling I model for the target [109], namely considering a target complex amplitude distributed as a zero-mean Gaussian random variable with covariance matrix $\mathbf{M}_t = E\{\boldsymbol{\alpha}\boldsymbol{\alpha}^H\}$, vector $\check{\mathbf{z}}_0$ turns into a complex Gaussian random variable with zero-mean vector and covariance matrix $\mathbf{D}_0 = 2\mathbf{I}_L + \mathbf{C}^H\mathbf{B}^H(\mathbf{t}\mathbf{t}^H \otimes \mathbf{M}_t)\mathbf{B}\mathbf{C}$.

Therefore, in this case, we look for a closed form expression for the asymptotic $Pd \triangleq \text{Prob}\{\|\check{\mathbf{z}}_0\|^2 > \eta \,|H_1\}$, with $\check{\mathbf{z}}_0|_{H_1} \sim \mathcal{CN}(\mathbf{0}_{L\times 1}, \mathbf{D}_0)$.

To this purpose we can use some recent results from the theory of indefinite quadratic forms in Gaussian random variables [4]. To this end, let $\gamma_0 \ldots \gamma_{R-1}$ denote the $R \leq L$ distinct non-zero eigenvalues of $\mathbf{D}_0$, each with multiplicity μ_r, $r = 0, \ldots, R-1$.

Following the approach in [4] we can write the Pd expression as follows (see Appendix D for the derivation):

$$P_d = \sum_{r=0}^{R-1}\sum_{k=0}^{\mu_r-1} \frac{-e^{-\frac{\eta}{\gamma_r}}\eta^k}{\Gamma(k+1)}\delta_{k,r} \tag{3.32}$$

where η is the threshold, and the coefficients $\delta_{k,r}$ definition is detailed in eq. (D.3) of Appendix D. The expression above takes simplified forms for the special cases of either a

unique eigenvalue (γ_0) with multiplicity L or L distinct eigenvalues. Specifically, in the former case we obtain

$$P_d = \sum_{l=0}^{L-1} \frac{\eta^l}{\gamma_0^l \, \Gamma(l+1)} e^{-\frac{\eta}{\gamma_0}} \tag{3.33}$$

which corresponds to a Gamma distributed test statistic, i.e.

$$T_{Pol-AR-AMF} \xrightarrow{asymp.} T_{Pol-AR-MF} \sim \Gamma(L, \gamma_0) \tag{3.34}$$

whereas, in the case of L distinct eigenvalues, we have

$$P_d = \sum_{l=0}^{L-1} \frac{\gamma_l^{L-1}}{\prod_{\substack{i=0 \\ i \neq l}}^{L-1} (\gamma_l - \gamma_i)} \, \mathrm{e}^{-\frac{\eta}{\gamma_l}} \tag{3.35}$$

which yields, for the test statistic, the following asymptotic pdf:

$$T_{Pol-AR-AMF} \xrightarrow{asymp.} T_{Pol-AR-MF} \sim \sum_{l=0}^{L-1} \frac{\gamma_l^{L-2}}{\prod_{\substack{i=0 \\ i \neq l}}^{L-1} (\gamma_l - \gamma_i)} \, \mathrm{e}^{-\frac{\eta}{\gamma_l}} \tag{3.36}$$

3.4 Numerical Results

In this Section, we investigate the performance of the proposed detector via numerical examples. To this aim, we generate the disturbance signal as a L–channel AR $(Q-1)$ process and matrices $\mathbf{A}$ and $\mathbf{R}$ and we carry out Monte Carlo (MC) simulations with proper number of trials. We consider an order $Q - 1 = 3$ for the AR process with $L = 3$ (HH, VV, HV) polarimetric channels.

The AR$(Q-1)$ parameters $\mathbf{A}$ and $\mathbf{R}$ are set so that the auto- and cross- spectra of the available channels are those reported in Figure 3.1 [54]. Specifically, Figure 3.1 shows that, in the considered example, the disturbance at channels HH and VV has identical spectral characteristics and equal power level, i.e. $\sigma_{d,HH}^2 = \sigma_{d,VV}^2 = \sigma_d^2$, deliberately set to $\sigma_d^2 = 1$. The cross-spectrum between the HH and VV channels reveals a good correlation between the corresponding signals yielding a correlation coefficient equal to $\rho_{HH/VV} = 0.9$. The disturbance affecting the HV channel is generated with power level 20dB lower than in HH and VV, i.e. $\sigma_{d,HV}^2 = 0.01\sigma_d^2$. Moreover, the cross-polarized components are assumed independent from the co-polarized ones, i.e. $\rho_{HV/HH} = \rho_{HV/VV} = 0$ thus resulting in null cross-spectra. In Figure 3.2 we study the capability of controlling the *Pfa* as a function of the number of training data.

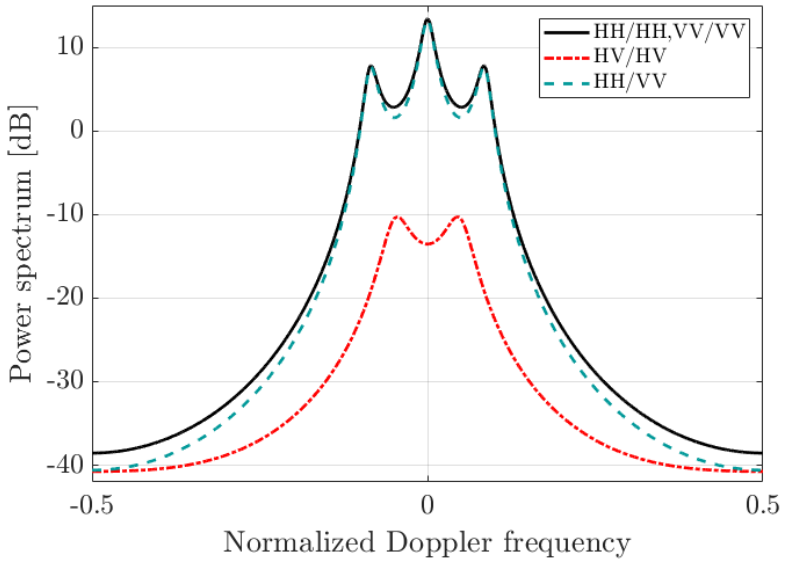

Figure 3.1: Power spectra of a L-channel $AR(3)$ process

Specifically, we report the actual Pfa obtained for the Pol-AR-AMF with 10^6 MC trials by selecting a desired $Pfa = 10^{-3}$ and setting the threshold according to the asymptotic Pfa in (3.29). Specifically, the results are reported for different numbers L of polarimetric channels in Figure 3.2(a) whereas in Figure 3.2(b) we compare the curves obtained for different numbers M of temporal observations as provided by a coherent train of pulses (an active pulse radar system is assumed in the reported examples).

By observing Figure 3.2 the following considerations are in order:

- In all considered cases, the actual Pfa tends to the nominal false alarm used to set the threshold ($Pfa = 10^{-3}$) as the number P of secondary data increases. This on one hand confirms the correctness of the asymptotic expression in (3.29) and on the other hand demonstrates that the detection threshold obtained from (3.29) could be exploited in practice when the number of secondary data is sufficiently high. When this condition does not hold, adaptivity loss prevails, which yields a false alarm rate higher than the desired value.
- By keeping the number of pulses constant ($M = 32$ in Figure 3.2 (a)), the higher the number of polarimetric channels is the higher is the number of training data required to have acceptable adaptivity loss. This is because a bigger ($QL \times QL$) matrix must be estimated, being $Q = 4$ in the considered case study.
- However, we observe that, in this case, a number P of training data equal to QL is typically sufficient to guarantee the 'asymptotic' condition since the matrix estimation benefits from the average performed across the temporal observations within the CPI.

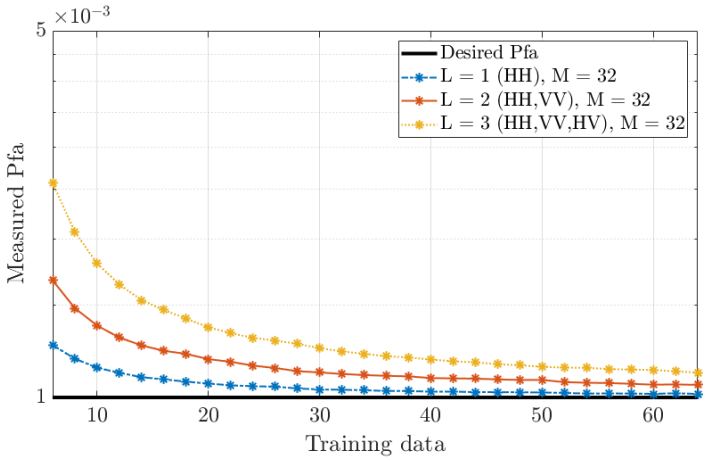

(a)

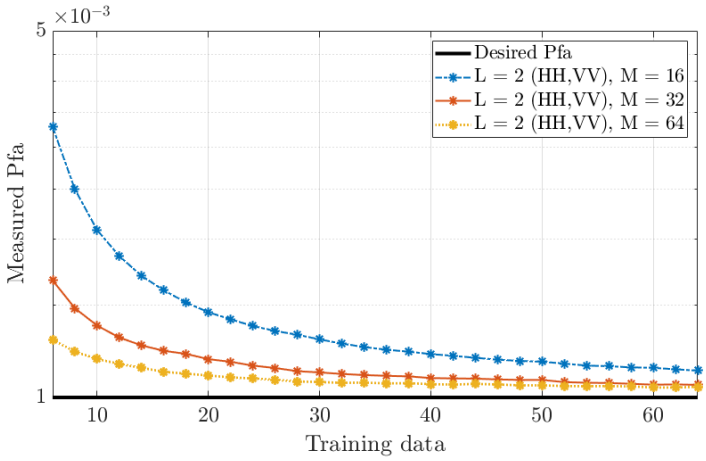

(b)

Figure 3.2: Actual Pfa versus P when $Pfa = 10^{3}$ for (a) different polarimetric channels and (b) different pulses

- The consideration above is confirmed in Figure 3.2(b) where we kept the number of polarimetric channels constant ($L = 2$), while comparing the results obtained for different values of M. In fact, as the number of pulses increases, the training data required to have a good false alarm rate control decrease. This is because a higher number of consecutive temporal observations is available to estimate the same number of unknown parameters.

The detection performance of the proposed detector is analysed in Figure 3.3 and Figure 3.4, by comparison with the Pol-GLRT [82],[83] in (3.8) and the Pol-AMF [26] in (3.7). First, a Swerling 0 target model is assumed in Figure 3.3. Accordingly, the target complex amplitudes are deterministic and, in the considered case study, are set as $\boldsymbol{\alpha} = a_t\begin{bmatrix}1 & e^{j\Delta\phi_{HH/VV}} & \sqrt{\xi_t}e^{j\Delta\phi_{HH/HV}}\end{bmatrix}^T$, where $\xi_t = 0.1$, $\Delta\phi_{HH/VV} = \pi/4$, and $\Delta\phi_{HH/HV} = \pi/2$. The results are reported as a function of the signal-to-clutter ratio (SCR) at the first polarimetric channel, i.e. SCR $= |a_t|^2/\sigma_d^2$.

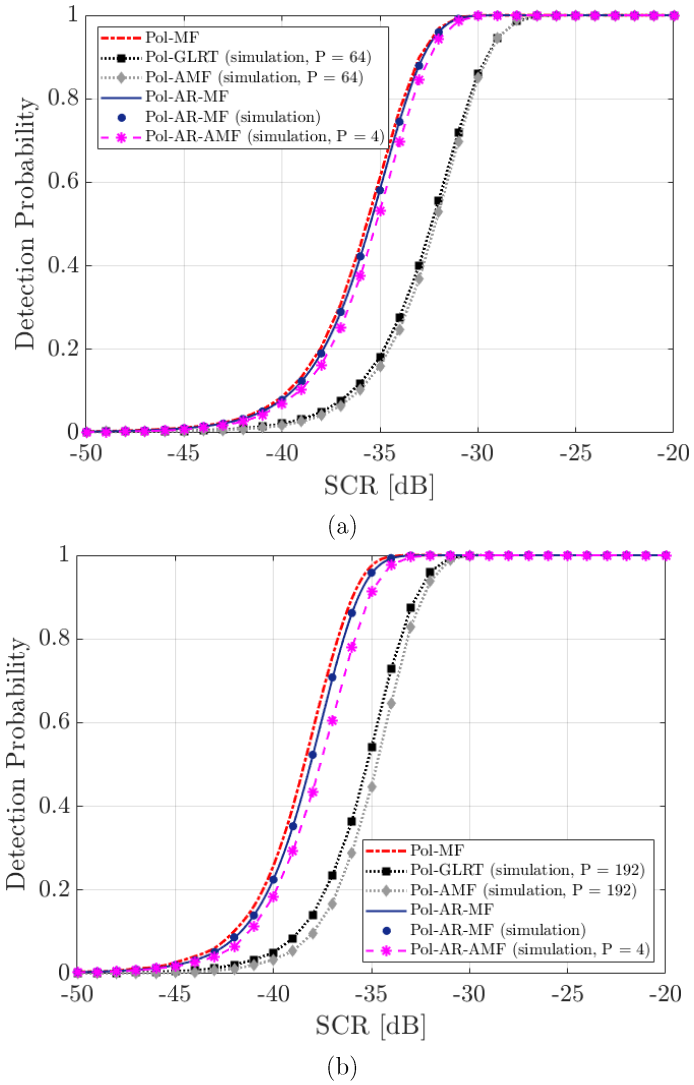

Figure 3.3: *Pd* versus SCR for $M = 32$, Swerling 0 target model and different polarimetric channels: (a) $L = 1$ (HH), (b) $L = 3$ (HH, VV, HV)

We consider $M = 32$, target normalized Doppler frequency $f_d = 0.25$ and different numbers of polarimetric channels. Specifically, in Figure 3.3(a) we use $L = 1$ (HH) while in Figure 3.3(b) we consider $L = 3$ (HH, VV, HV). We note that, when $L = 1$, the proposed detector falls within the single-channel parametric approaches [3],[14] that only exploit the temporal domain for clutter cancellation and target detection.

Then, the same case studies are considered in Figure 3.4 except that a fluctuating target model is used according to a Swerling I model. Specifically, the target complex amplitudes vector $\boldsymbol{\alpha}$ is generated as a zero-mean Gaussian random vector, with the following covariance matrix

$$\mathbf{M}_t = \sigma_t^2 \begin{bmatrix} 1 & \rho_t & 0 \\ \rho_t & 1 & 0 \\ 0 & 0 & \xi_t \end{bmatrix} \tag{3.37}$$

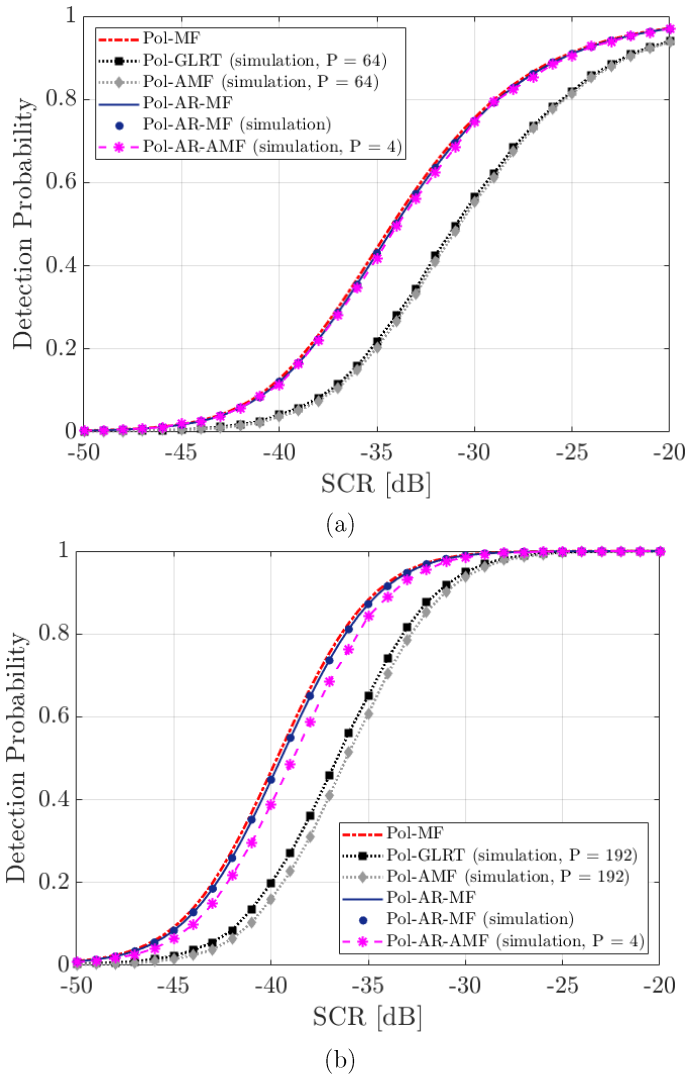

Figure 3.4: *Pd* versus SCR for $M = 32$, Swerling I target model and different polarimetric channels: (a) $L = 1$ (HH), (b) $L = 3$ (HH, VV, HV)

denoting ρ_t as the cross-correlation coefficient between the two co-polarized target amplitudes. In this analysis, $\rho_t = 0$ and $\xi_t = 0.1$. Again, Figure 3.4(a) and Figure 3.4(b) have been obtained for $L = 1$ (HH) and $L = 3$ (HH, VV, HV) polarimetric channels, respectively. In all figures, the Pol-MF is considered as a benchmark of our performance evaluation and its performance are reported in dash-dot red. The performance of the Pol-GLRT and the Pol-AMF are reported in dotted black and grey, respectively, and both are operated using $P = 2ML$.

The theoretical asymptotic *Pd* for the proposed detector is reported in continuous dark blue line while the results of the MC simulation for the clairvoyant Pol-AR-MF (with 10^4 independent MC trials) are reported in dark blue dots. The MC simulation results obtained when applying the adaptive detector Pol-AR-AMF, with P secondary data are reported in dashed magenta.

The *Pfa* has been chosen to be 10^{-3} and, for a fair comparison, the detection threshold of the Pol-AR-AMF has been numerically adjusted to guarantee the desired false alarm rate even in non-asymptotic regime.

By observing Figure 3.3 and Figure 3.4, the following considerations apply.

- The Pol-MF sets the performance bounds, that improve moving from a system equipped with single polarimetric channel to a fully polarimetric system employing $L = 3$ channels, thanks to the enhanced capability to discriminate target echoes from disturbance. The improvement is larger for the Swerling I target model since the polarimetric channels combination also allows the amplitude fluctuations to be averaged out thus removing some of the target fades.
- The Pol-GLRT and the Pol-AMF yield a non-negligible detection loss (3-4 dB) with respect to their clairvoyant version (Pol-MF) employing all the available degrees of freedom for disturbance removal. This is due to the need to estimate a very high number of unknown parameters when no model is adopted for the disturbance spectral characteristics. As expected, the Pol-GLRT shows a slight advantage over the Pol-AMF. However, the number of secondary data for both detectors has been adjusted so that $P = 2ML$, which yields $P = 64$ and $P = 192$ for $L = 1$ and $L = 3$, respectively. In practical cases it may be difficult to obtain the required amount of training data with the desired characteristics so that further degraded performance is expected for both the fully adaptive detection schemes.
- Whilst it exploits a reduced number of temporal degrees of freedom for clutter cancellation, the Pol-AR-MF shows comparable performance with respect to the Pol-MF provided that the number Q of taps matches the actual order of the AR process modelling the disturbance. The case of a possible mismatch between the disturbance spectral characteristics and the order of the AR process used to build the detector is addresses in Chapter 4.
- The slight loss observed in Figure 3.3 and Figure 3.4 is only due to the border effect arising from a block-based implementation of the detection scheme as discussed in Section 3.2.2. In fact, according to this implementation, the summation across the sequence $\mathbf{y_0}(\mathrm{m})$ is limited to $M - Q - 1$ consecutive samples thus a loss of $(Q - 1)/M$ is obtained for the corresponding integration gain over the available CPI. Incidentally, we recall that other implementations are possible, e.g. based on lattice filters, where this loss might be avoided by processing partially overlapped data batches.
- The theoretical asymptotic Pd expressions perfectly match with the MC simulation results, implying that the obtained expressions can accurately describe the detection performance of the Pol-AR-MF both under the deterministic and stochastic target models.

- The Pol-AR-AMF yields remarkable detection performance with only a limited adaptivity loss with respect to its clairvoyant version Pol-AR-MF. As expected, this loss increases as L increases, since a bigger ($QL \times QL$) matrix must be estimated and the number of training data has been kept constant ($P = 4$ in all considered cases).
- Nevertheless, the Pol-AR-AMF outperforms the other polarimetric adaptive detectors, even using much fewer training data. This advantage clearly demonstrates its suitability for practical applications.

In Figure 3.5(a-c), we show the probability of detection for a Swerling I target model and $M = 2$ polarimetric channels (HH, VV), when using a number M of pulses equal to 16, 32, and 64, respectively. In all cases, the Pol-AR-AMF is applied with $P = 4$ training data while both the Pol-GLRT and the Pol-AMF use $P = 2ML$, namely $P =$ 64,128 and 256. Similar considerations apply as for the results reported in Figure 3.3 and Figure 3.4.

In addition, by comparing Figure 3.5(a-c), we further notice that, as the number M of pulses increases:

- all target detection strategies benefit from the increased number of temporal observations that at least provides an increased coherent integration gain.
- Moreover, the observed loss of the Pol-AR-AMF with respect to the Pol-MF due to the border effect decreases since the number of samples excluded from the coherent integration ($Q - 1$) becomes less significant with respect to M. To parity of training data, the adaptivity loss shown by the Pol-AR-AMF decreases thanks to the higher number of temporal observations available to estimate the same number of parameters (QL). In this regard, we observe that, even operating with $P = 4$; in the considered case study, the Pol-AR-AMF substantially reaches its asymptotic detection performance for $M \geq 32$.
- In contrast, the conventional polarimetric adaptive detection schemes, i.e. the Pol-GLRT and the Pol-AMF, require a progressively higher number of secondary data in order to control the adaptivity loss, making such detection strategies unsuitable for real application. This conclusion is further reinforced by considerations relevant to the computational burdens required by these detectors.
- Overall, the advantage of the Pol-AR-AMF over the Pol-GLRT and the Pol-AMF increases as M increases showing that the number of temporal degrees of freedom to be employed adaptively can be kept constant thus easing the training/computational burden while guaranteeing the desired disturbance removal. In fact, the Pol-AR-AMF allows the additional temporal observations to be effectively exploited to reduce the adaptivity loss and to enhance the coherent integration of target echoes.

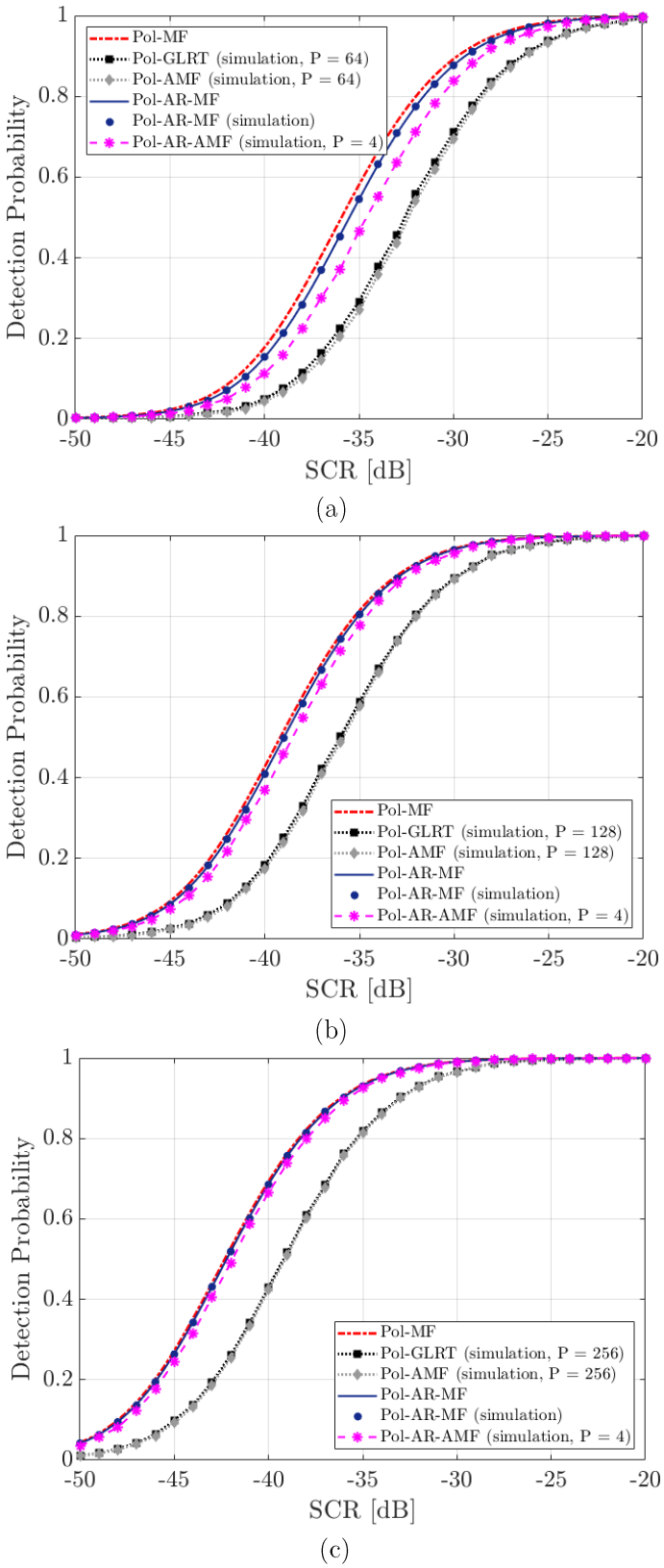

Figure 3.5: Pd versus SCR for $L = 2$ (HH, VV) and different pulses: (a) $M = 16$, (b) $M = 32$, (c) $M = 64$

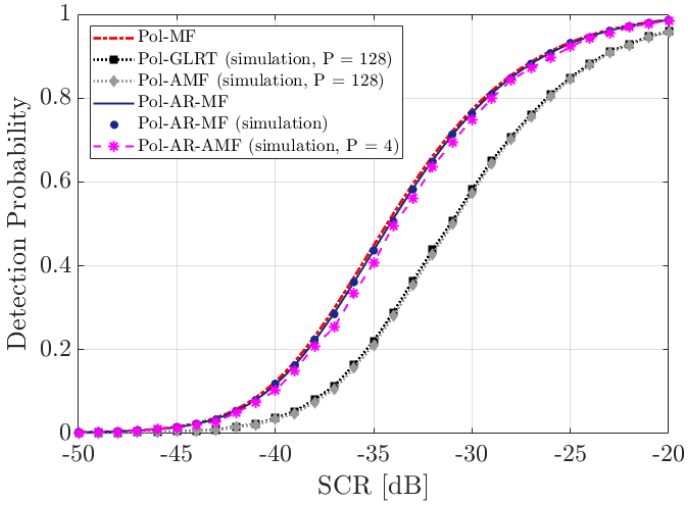

Figure 3.6: Pd versus SCR for $L = 2$ (HH, VV), $M = 32$ and $\rho_t = 0.99$

Note that, although the devised comments specifically refer to the considered case study, similar considerations apply to alternative cases obtained with a different choice of the relevant parameters. For instance, we plot in Figure 3.6 the results obtained when considering the same scenario used in Figure 3.5(b) but assuming that the cross-correlation coefficient between the target amplitudes at channels HH and VV is equal to $\rho_t = 0.99$.

As it is apparent the performance of all the considered detection schemes degrade since the target echoes at the two co-polarized channels are correlated, so that the target fade average is much less effective than in the former case in which $\rho_t = 0$. Moreover, the target echoes are also partially cancelled by the clutter cancellation stage of the adaptive detectors which is intended to mitigate polarimetric correlated signals. However, we highlight that the comparative analysis between different adaptive detectors remains unchanged and the Pol-AR-AMF still outperforms the fully adaptive detectors even operating with a much smaller training data size.

The considerations above are confirmed by Figure 3.7(a-b), where we study the detection performance depending on the selected Doppler frequency and target polarimetric cross-correlation coefficient. In Figure 3.7 (a), we consider SCR = – 35 dB and $P_{fa} = 10^{-3}$, and we report the Pd obtained with the proposed Pol-AR-MF for the same scenario used in Figure 3.6 as a function of ρ_t and f_d. In Figure 3.7 (b), we compare it with the Pol-GLRT operated using $P = 2ML = 128$ and with the Pol-AR-AMF operated using $P = 4$, for $\rho_t = 0$ and $\rho_t = 0.99$. In both Figure 3.7(a) and (b), a logarithmic scale has been used to enhance the difference at high Pd values. As expected, as the target polarimetric correlation coefficient decreases, the cancellation notch obtained with all the considered approaches progressively narrows allowing a better discrimination of the target echo against the polarimetric correlated disturbance.

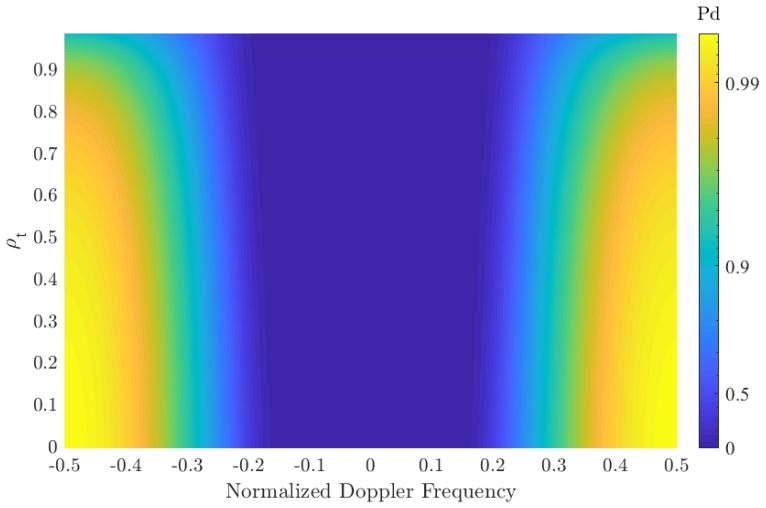

(a)

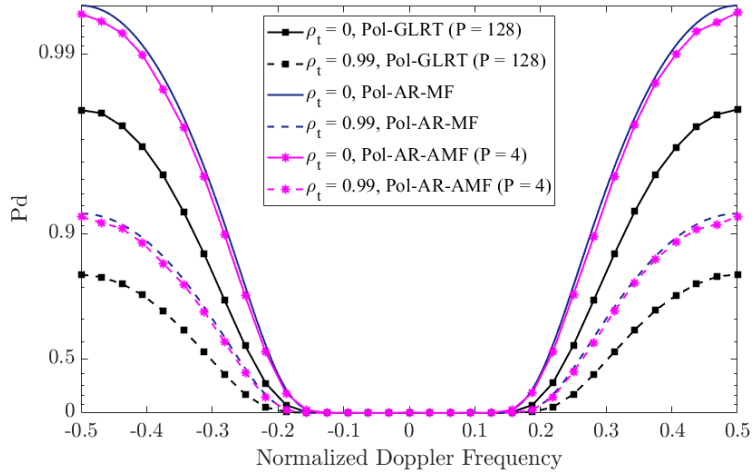

(b)

Figure 3.7: P_d for SCR = – 35 dB, $P_{fa} = 10^{-3}$, $L = 2$ (HH, VV), $M = 32$:
(a) P_d for Pol-AR-MF as a function of f_d and ρ_t
(b) P_d versus f_d for $\rho_t = 0$ and ρ_t= 0.99.

However, for both the considered ρ_t values, the proposed Pol-AR-AMF operating with $P = 4$ nearly reaches its asymptotic detection performance thus remarkably outperforming the conventional Pol-GLRT. Specifically, it provides a target detection probability improvement up to 20% in the considered scenario.

3.5 Summary

In this Chapter, we derived a novel polarimetric adaptive detector based on a multi-channel AR process for the disturbance. The asymptotic expressions for the performance of the proposed detector have been derived and the effectiveness of the proposed approach has

been investigated via numerical analysis. It was shown that the devised approach can improve the target detection capability with respect to traditional detection schemes when both single-pol and multi-pol radar systems are considered. Moreover, based on the adopted parametric method, the proposed detection scheme also allows to relax the requirement on the number of target-free training data and on the computational effort, which are key points in applications where the number of adaptive degrees of freedom is large as well as in heterogeneous environment.

These conclusions are indeed valid when the input disturbance strictly follow the underlying model adopted for the detector design. In real-world scenario this is rarely the case therefore it is of high practical interest to understand the behaviour of the proposed detection scheme when applied against disturbance components with diverse spectral characteristics. Therefore, in Chapter 4 the general case of an input disturbance process that does not exactly match the employed AR $(Q-1)$ model will be addressed.

Chapter 4
Polarimetric adaptive target detector based on a multi-channel AR model: Performance Assessment under Mismatched Spectral Model

In Chapter 3, a multi-channel AR model based polarimetric detection scheme has been developed and its performance has been studied against clutter with characteristics exactly matching the adopted parametric model. In this Chapter, we address the general case of an input disturbance process that does not exactly match the employed AR(Q-1) model and the performance assessment is extended, by means of theoretical and simulated analyses, to include the case of disturbance components with diverse spectral characteristics. Consequently, an appropriate modification is introduced to the detection scheme to make it robust to typical spectral mismatches occurring in practical situations.

In Section 4.1 we briefly recall the AR model based polarimetric detector introduced in Chapter 3 and provide theoretical expressions for its detection performance under spectral model mismatches. A numerical analysis is then reported in Section 4.2 for two different case studies. The modified AR model based polarimetric adaptive detector is presented in Section 4.3 whereas its performance is assessed in Sections 4.4. Eventually, we draw our conclusions in Section 4.5.

4.1 Theoretical asymptotic performance under disturbance model mismatch

Let us consider the test statistic of the clairvoyant detector derived in Chapter 3 , reported here for ease of reference

$$T_{Pol-AR-MF} = \mathbf{x}_0^H \mathbf{B}\,\mathbf{C}\,\mathbf{C}^H \mathbf{B}^H \mathbf{x}_0 \underset{H_0}{\overset{H_1}{\gtrless}} \eta_{AR-MF} \tag{4.1}$$

where $\mathbf{x_0}$ is the vector where we arrange the primary data samples collected M at consecutive temporal observations from the L available polarimetric channels. Matrices $\mathbf{B}$ and $\mathbf{C}$ depend on the AR(Q – 1) parameters as well as on the target temporal steering vector; their definitions are detailed in Chapter 3 and are summarized in Table 4.1.

In Chapter 3, we addressed the *matched* case, namely the case of an input disturbance that exactly matches the AR(Q – 1) model adopted for the design of the detection scheme and we provided analytical expressions of the asymptotic performance of the derived detector. More precisely, the *Pfa* expression to be used when setting the detection threshold is given by eq. (3.29) and it is reported here for ease of reference

$$P_{fa} = \sum_{l=0}^{L-1} \frac{\eta^l}{2^l\,\Gamma(L-l)} e^{-\frac{\eta}{2}} \tag{4.2}$$

being η the detection threshold, while equations (3.31) and (3.32) report the asymptotic detection probability *Pd* expressions for the Swerling 0 and Swerling I target model [109], respectively. In this Chapter, we address the general case of an input disturbance that is not drawn from the assumed AR (Q – 1) model. Still, we assume that matrices $\mathbf{B}$ and $\mathbf{C}$ in (4.1) are evaluated based on the parameters of a multichannel AR process of given order (Q – 1). In other words, we evaluate matrices $\mathbf{A}_{mis}(L(Q-1)\times L)$ and $\mathbf{R}_{mis}(L\times L)$ starting from the actual data covariance matrix $\mathbf{M}$, i.e. $\mathbf{M} = E\{\mathbf{x_0}\mathbf{x_0}^H\}$, via the following relations

$$\begin{cases} \mathbf{A}_{mis} = \bar{\mathbf{M}}_{00}^{-1}\bar{\mathbf{M}}_{01} \\ \mathbf{R}_{mis} = \bar{\mathbf{M}}_{11} - \bar{\mathbf{M}}_{01}^H\,\bar{\mathbf{M}}_{00}^{-1}\bar{\mathbf{M}}_{01} \end{cases} \tag{4.3}$$

being $\bar{\mathbf{M}} = \begin{bmatrix} \bar{\mathbf{M}}_{00} & \bar{\mathbf{M}}_{01} \\ \bar{\mathbf{M}}_{01}^H & \bar{\mathbf{M}}_{11} \end{bmatrix}$ the first $QL\times QL$ block of matrix $\mathbf{M}$, with $\bar{\mathbf{M}}_{00}(L(Q–1)\times L(Q–1))$, $\bar{\mathbf{M}}_{01}(L(Q–1)\times L)$ and $\bar{\mathbf{M}}_{00}(L\times L)$. As a consequence, matrices $\mathbf{A}_{mis}$ and $\mathbf{R}_{mis}$ represent the parameters of an AR model that possibly approximates the actual spectral characteristics of the disturbance but does not exactly match them. Therefore, the filtering of the data via matrices $\mathbf{B}$ and $\mathbf{C}$ does not provide a perfect whitening in either the polarimetric and the temporal domain. In contrast, some residual correlation might appear. These residuals in turn depend on the actual characteristics of the input disturbance and are expected to degrade the performance of the detector both in terms of *Pfa* control and *Pd*. These effects are investigated in the following for the clairvoyant detector in (4.1). The reported analysis is also representative of the asymptotic performance, of the adaptive version of the proposed detector, the Pol-AR-AMF, under spectral model mismatch. Specifically, provided that a large number of training data P is available, we assume that the ML estimate of the covariance matrix $\widehat{\mathbf{M}}$ tends towards the actual disturbance covariance matrix $\mathbf{M}$ and, consequently, the estimated AR parameters tend towards the clairvoyant, though mismatched, values in (4.3).

Table 4.1
Summary of defined quantities

Quantity	Definition/meaning
$\mathbf{B}$	$[\mathbf{B}_0 \quad \mathbf{B}_1 \quad \dots \quad \mathbf{B}_{M-Q}]$
$\mathbf{C}$	$\sqrt{2}(\mathbf{1}_{M-Q+1\times 1} \otimes \mathbf{W}^{-\frac{1}{2}})$
$\mathbf{B}_m$	$\begin{bmatrix} \mathbf{0}_{Lm\times L} \\ \mathbf{P\Sigma}(m) \\ \mathbf{0}_{L(M-Q-m)\times L} \end{bmatrix}$
$\mathbf{W}$	$\sum_{m=0}^{M-Q} \mathbf{\Sigma}^H(m)\mathbf{P}\,\mathbf{\Sigma}(m)$
$\mathbf{P}$	$\mathbf{H}^H\mathbf{R}^{-1}\mathbf{H}$
$\mathbf{H}$	$[-\mathbf{A}^H \quad \mathbf{I}_L]$
$\mathbf{\Sigma}(m)$	$\tilde{\mathbf{t}}(m) \otimes \mathbf{I}_L$
$\tilde{\mathbf{t}}(m)$	Q-dimensional sub-vector of the temporal steering vector starting from the m-th sample

In sub-Section 4.1.2-A, we focus on the probability of false alarm while corresponding expressions for the target detection probability are developed in sub-Section 4.1.2-B.

4.1.1 False alarm probability

Let us consider the test statistic of the clairvoyant detector in (4.1) and define the L–dimensional vector $\check{\mathbf{z}}_0 = \mathbf{C}^H\mathbf{B}^H\mathbf{x}_0$, namely $\check{\mathbf{z}}_0$ represents the data after both polarimetric and temporal disturbance cancellation, which then undergoes the non-coherent integration across the polarimetric channels.

Under the H_0 hypothesis, $\check{\mathbf{z}}_0$ is a zero-mean complex Gaussian random vector with covariance matrix $\mathbf{D}_0 = \mathbf{C}^H\mathbf{B}^H\,\mathbf{M}\,\mathbf{BC}$, being $\mathbf{M}$ the actual covariance matrix of the input disturbance process, i.e. $\check{\mathbf{z}}_0|_{H_0} \sim \mathcal{CN}(\mathbf{0}_{L\times 1}, \mathbf{D}_0)$.

Depending on the form taken by the matrix $\mathbf{M}$, the test statistic in (4.1), namely $T_{Pol\text{-}AR\text{-}MF} = \|\check{\mathbf{z}}_0\|^2$ might have different distributions. For the 'matched' case, we recall that $\mathbf{D}_0 = 2\mathbf{I}_L$ (see Appendix C for proof). In contrast, for the general case when the input disturbance process does not strictly follow the AR($Q-1$) model, some residual correlation might appear after the temporal cancellation stage so that $\mathbf{D}_0 \neq 2\mathbf{I}_L$ and (4.2) is no longer valid.

However, we can resort to the same approach reported in Appendix D to derive a closed form expression for the *Pfa*. Let $\gamma_0, \dots, \gamma_{R-1}$ denote the $R \leq L$ distinct non-zero eigenvalues of $\mathbf{D}_0$, each with multiplicity μ_r, $r = 0, \dots, R-1$. By proceeding as in [50], we obtain the *Pfa* expression as follows

$$P_{fa} = \sum_{r=0}^{R-1} \sum_{k=0}^{\mu_r - 1} \frac{-e^{-\frac{\eta}{\gamma_r}} \eta^k}{\Gamma(k+1)} \delta_{k,r} \tag{4.4}$$

where η is the threshold, and the definition of the coefficients $\delta_{k,r}$, $k = 0, \ldots, \mu_r - 1$, $r = 0, \ldots, R - 1$, is detailed in eq.(D.3) of Appendix D. By inverting (4.4) the threshold η_{AR-MF} can be obtained for the clairvoyant detector in (4.1).

In the special case when no eigenvalue is repeated, which is typically verified in practical cases under spectral mismatch, namely when $R = L$ and $\mu_r = 1$, $r = 0, \ldots, R - 1$, eq. (4.4) can be simplified and the following *Pfa* is easily obtained

$$P_{fa} = \sum_{l=0}^{L-1} \frac{\gamma_l^{L-1}}{\prod_{\substack{i=0 \\ i \neq l}}^{L-1} (\gamma_l - \gamma_i)} \mathrm{e}^{-\frac{\eta}{\gamma_l}} \tag{4.5}$$

In the dual special case when matrix $\mathbf{D}_0$ has one unique eigenvalue λ_0 ($R = 1$) with multiplicity $\mu_0 = L$, the test statistic turns into a Gamma distributed variable, i.e.

$$T_{Pol-AR-MF} \sim \Gamma(L, \gamma_0) \tag{4.6}$$

and the *Pfa* expression can be simplified as

$$P_{fa} = \sum_{k=0}^{L-1} \frac{\left(\eta / \gamma_0\right)^k e^{-\frac{\eta}{\gamma_0}}}{\Gamma(k+1)} \tag{4.7}$$

Note that (4.7) is equivalent to (4.2), if the scale parameter $\gamma_0 = 2$,, namely if a perfect whitening has been obtained in both the polarimetric and temporal domain. In the general case, we expect that the higher similarity exists between the adopted AR model and the actual correlation characteristics of the disturbance process, the better this is rejected and the closer (4.4) gets to (4.2).

In contrast, in the general spectral mismatched case, the derived *Pfa* expressions, and hence the threshold η_{AR-MF} to be used, depend on the eigenvalues of the residual disturbance matrix $\mathbf{D}_0$ that are unknown in practical cases. Therefore, by recalling that the reported performance is representative of the performance of the adaptive polarimetric detector Pol-AR-AMF for large number of training data, we conclude that it does not ensure the CFAR property even in the asymptotic regime if spectral model mismatches exists. The CFAR characteristic tends to be guaranteed only if the adopted model reasonably approximates the spectral characteristics of the disturbance.

4.1.2 Detection probability

The disturbance residuals arising from the cancellation stage are also responsible of degradations in terms of target detection capability. These are theoretically investigated in the following with reference to a Swerling 0 target model and a Swerling I target model, respectively.

A. Non-fluctuating target model (Swerling 0)

When a non-fluctuating target model (Swerling 0) is assumed, vector $\check{\mathbf{z}}_0$ is a complex Gaussian random vector, with mean vector $\boldsymbol{\upsilon} = \mathbf{C}^H\mathbf{B}^H\mathbf{s}$, being $\mathbf{s}$ the target component in the received primary data, and covariance matrix $\mathbf{D}_0$, i.e. $\check{\mathbf{z}}_0|_{H_1} \sim \mathcal{CN}(\boldsymbol{\upsilon},\mathbf{D}_0)$. According to this model, the test statistic of the clairvoyant detector, $T_{Pol-AR-MF} = \|\check{\mathbf{z}}_0\|^2$, is a non-central quadratic form and the *Pd* cannot be written in a closed form for any $\mathbf{D}_0$. However, following the approach in [50], in Appendix E we develop an approximated expression for the asymptotic *Pd* that can be written as:

$$P_d \approx 1 - \frac{e^{-p_0\,\eta}}{p_0\sqrt{2\pi}} \sum_{l=0}^{L-1} \frac{1}{1-p_0\gamma_l} \frac{e^{\sum_{l=0}^{L-1}|\bar{v}_l|^2\left[\frac{1}{1-p_0\gamma_l}-1\right]}}{\sqrt{\left|\frac{1}{p_0^2} - \sum_{l=0}^{L-1}\left[\frac{{\gamma_l}^2}{(1-p_0\gamma_l)^2}\left(1+\frac{2|\bar{v}_l|^2}{1-p_0\gamma_l}\right)\right]\right|}} \tag{4.8}$$

where η is the detection threshold evaluated from (4.4), $p_0 = -(j\,\omega_0 + \beta)$ and the definitions of ω_0 and β are detailed in the Appendix D.

B. Fluctuating target model (Swerling I)

Assuming a Swerling I model for the target, namely if the target complex amplitude is a zero-mean Gaussian random variable with covariance matrix $\mathbf{M}_t = E\{\boldsymbol{\alpha}\boldsymbol{\alpha}^H\}$, vector $\check{\mathbf{z}}_0$ is a complex Gaussian random variable with zero-mean vector and covariance matrix $\mathbf{D}_0' = \mathbf{D}_0 + \mathbf{C}^H\mathbf{B}^H\,(\mathbf{t}\mathbf{t}^H \otimes \mathbf{M}_t)\,\mathbf{B}\mathbf{C}$, i.e. $\check{\mathbf{z}}_0|_{H_1} \sim \mathcal{CN}(\mathbf{0}_{L\times 1}, \mathbf{D}_0')$. Therefore, following the same procedure as for the *Pfa* in Section 4.1.1, the *Pd* is obtained as

$$P_d = \sum_{r=0}^{R-1}\sum_{k=0}^{\mu_r'-1} \frac{-e^{\left(-\frac{\eta}{\gamma_r'}\right)}\eta^k}{\Gamma(k+1)}\delta_{k,r}' \tag{4.9}$$

where η is the detection threshold, $\gamma_0', \ldots, \gamma_{R-1}'$ denote the $R \le L$ distinct eigenvalues of $\mathbf{D}_0'$, each with multiplicity μ_r', and the coefficients $\delta_{k,r}'$ are evaluated using eq. (D.3) of Appendix D, by replacing γ_n with γ_r'.

4.2 Asymptotic performance analysis against simulated data

In this Section, we carry out an asymptotic performance analysis of the proposed detector via numerical examples. The purpose of this Section is twofold. First, we aim at verifying the validity of the theoretical performance expressions, then we aim at investigating the performance loss only due to the spectral model mismatch, neglecting the additional degradation introduced by the adaptivity that will be considered later.

To this aim, we carried on extensive MC simulations in two different case-studies, as detailed in the following:

- **Case study A**. In the first case study we assume that the disturbance is a L – channel AR (3) process and we investigate the robustness of the proposed detector when a model order mismatch occurs, namely when the detector is build using $Q \neq 4$. Specifically, the disturbance affecting the system is generated using the same parameters adopted in Chapter 3 with $L = 3$ (HH, VV, HV) polarimetric channels and $M = 32$.
- **Case study B.** In the second case study we consider the model used in [83], where a Gaussian spectral shape is adopted for the disturbance, and we investigate the robustness of the proposed detector that is based on a multi-channel AR model approximation. To this purpose, we generate a disturbance characterized by a disturbance covariance matrix $\mathbf{M}$ that can be written as $\mathbf{M} = \mathbf{\Pi} \otimes \mathbf{\Upsilon} + \sigma_n^2 \mathbf{I}_{LM}$, denoting $\mathbf{\Pi}$ as the normalized temporal covariance matrix shared by all polarimetric channels, $\mathbf{\Upsilon}$ as the disturbance polarimetric covariance matrix and σ_n^2 as the noise power, defined with respect to the clutter power at HH and VV channels σ_d^2 via the clutter-to-noise ratio (CNR) of 40dB. Specifically, we assume $\mathbf{\Pi}$ to be Gaussian shaped with one-lag correlation coefficient $\varrho = 0.95$, namely the generic element $\Pi_{m,p} = \varrho^{(m-p)^2}$, ($m$, $p = 0$, …, $M - 1$). We consider $M = 32$ and $L = 3$ (HH,VV,HV), and we assume that the HH and VV channel share the same disturbance power level, i.e. $\sigma_{d,HH}^2 = \sigma_{d,VV}^2 = \sigma_d^2$, deliberately set to $\sigma_d^2 = 1$, while the HV channel is generated with power level 20 dB lower than in HH and VV, i.e. $\sigma_{d,HV}^2 = \xi_d \, \sigma_d^2$, with $\xi_d = 0.01$. Furthermore, a correlation coefficient equal to $\rho_{HH/VV} = 0.9$ is set between the HH and VV channels, while the cross-polarized components are assumed independent from the co-polarized ones, i.e. $\rho_{HV/HH} = \rho_{HV/VV} = 0$ thus resulting in null cross-spectra. Ultimately, the disturbance polarimetric covariance matrix can be written as

$$\boldsymbol{\Upsilon} = \sigma_d^2 \begin{bmatrix} 1 & \rho_{HH/VV} & 0 \\ \rho_{HH/VV} & 1 & 0 \\ 0 & 0 & \xi_d \end{bmatrix} \tag{4.10}$$

In Figure 4.1(a), we plot the *Pfa* versus threshold obtained in case study A when employing the detector in (4.1) with a grid of Q values, encoded by different brown shades and line styles. Specifically, the reported curves have been obtained using the theoretical expression in (4.4), whereas the markers correspond to the results of MC simulations for the Pol-AR-MF. On the same figure, we also report in green the *Pfa* expression obtained from (4.2). This curve is representative of spectral *matched* case, i.e. a perfect whitening is assumed for the disturbance in both temporal and polarization domains.

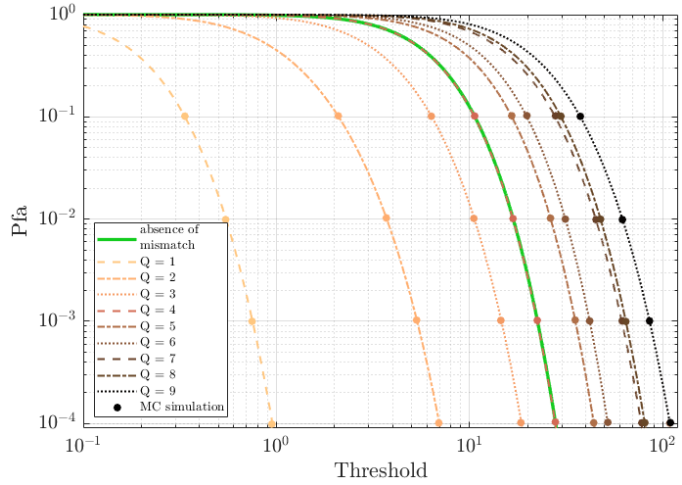

(a)

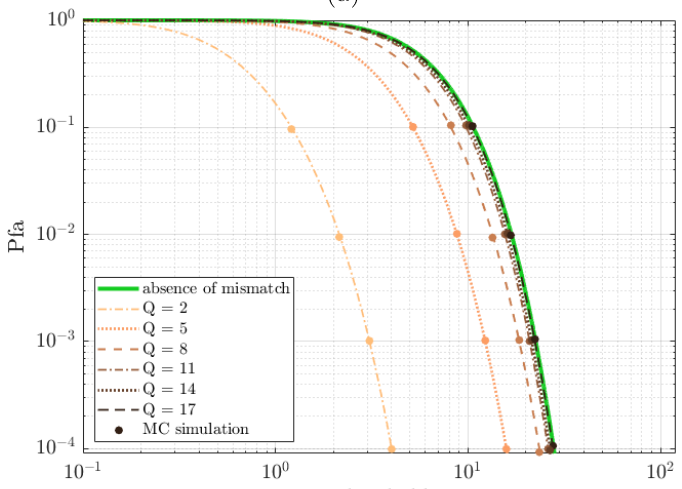

(b)

Figure 4.1: *Pfa* versus threshold for different values of Q for: (a) case study A, (b) case study B.

Similarly, in Figure 4.1(b) we report the results for case study B. Figure 4.1(a-b) show that:

- if a spectral model mismatch occurs, the detection threshold must be properly adjusted to guarantee the nominal *Pfa* and the required modification is largely dependent on the mismatch extent. This confirms that the CFAR property is not ensured even under the asymptotic condition.
- However, the higher the similarity between the AR process used to build the detection test and the true spectral characteristics of the disturbance, the closer gets the theoretical *Pfa* expression to (4.2), revealing that a better disturbance cancellation was performed.

Depending on the spectral characteristics of the input disturbance, the Q value that allows to have acceptable mismatch loss typically changes. As is expected, when the detector is fed with an AR disturbance process of order $\bar{Q} - 1$(case study A, Figure 4.1(a)), the mismatch loss increases when both underestimating and overestimating the model order with respect to the exact value $Q = \bar{Q} = 4$. In contrast, when case study B is considered (Figure 4.1(b)), as Q increases, the brown curves tend to look alike and to resemble the green curve. For instance, in this case, $Q \geq 15$ should be adopted to achieve an acceptable approximation of the Gaussian shaped power spectral density based on a multi-channel AR model, since a reasonably high temporal correlation coefficient was assumed in this case study. For the performance evaluation under the H_1 hypothesis, both Swerling 0 and Swerling I target models are considered, in Figure 4.2 and Figure 4.3, respectively. The target normalized Doppler frequency was set to $f_d = 0.25$ and the same set of parameters are adopted as in Chapter 3.

In particular, when a Swerling 0 target model is used (see Figure 4.2), the deterministic target complex amplitudes vector is set as $\boldsymbol{\alpha} = a_t\left[1 \quad e^{j\Delta\phi_{HH/VV}} \quad \sqrt{\xi_t}e^{j\Delta\phi_{HH/HV}}\right]^T$, where $\xi_t = 0.1$, $\Delta\phi_{HH/VV} = \pi/4$, and $\Delta\phi_{HH/HV} = \pi/2$.

When a fluctuating target model is adopted according to a Swerling I model (see Figure 4.3), vector $\boldsymbol{\alpha}$ is generated as a zero-mean Gaussian random vector, with covariance matrix

$$\mathbf{M}_t = \sigma_t^2 \begin{bmatrix} 1 & 0 & 0 \\ 0 & 1 & 0 \\ 0 & 0 & \xi_t \end{bmatrix} \tag{4.11}$$

where ξ_t has been set to $\xi_t = 0.1$. The results are reported for $Pfa = 10^{-3}$, for the two case studies A (see Figure 4.2(a) and Figure 4.3(a)) and B (see Figure 4.2(b) and Figure 4.3(b)) as a function of the SCR at the first polarimetric channel, i.e. SCR=$|a_t|^2/\sigma_d^2$ in Figure 4.2 and SCR = σ_t^2/σ_d^2 in Figure 4.3. In all figures, we plot in dash-dot red the *Pd* of the Pol-MF in (3.6) and we consider it as a benchmark of our performance evaluation since this detector does not make any assumption on the spectral shape of the actual disturbance but is based on the exact knowledge of the input disturbance covariance matrix.

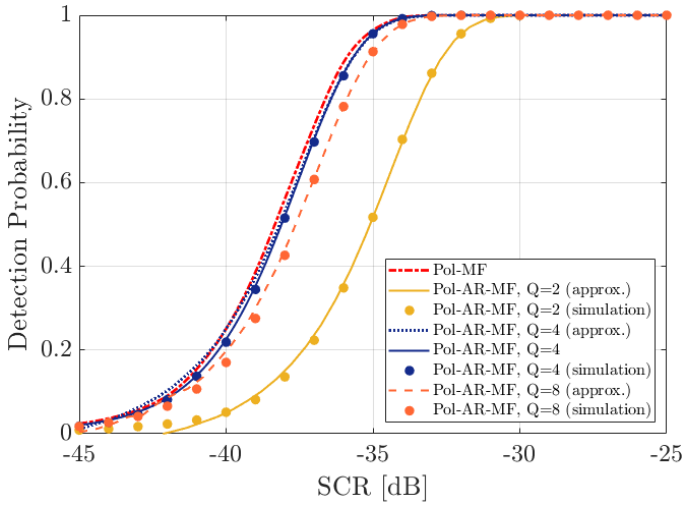

(a)

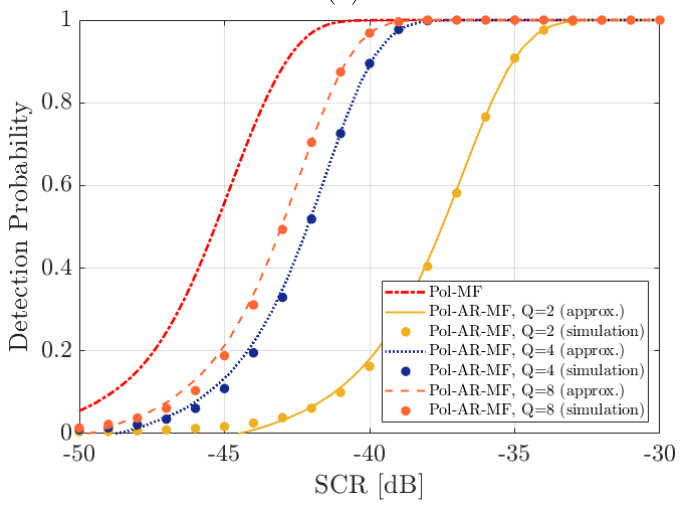

(b)

Figure 4.2: Pd versus SCR for $Pfa = 10^{-3}$, Swerling 0 target model and (a) case A, (b) case B

Also, in each figure, we compare the MC simulation results of the Pol-AR-MF with the appropriate theoretical expressions, i.e. from either (4.8) or (4.9), depending on the target model, for three different values of Q, namely $Q = 2$, 4 and 8.

By observing Figure 4.2 and Figure 4.3, the following considerations apply.

- Both the closed-form and the approximate theoretical expressions match well with the results of the MC simulations, implying that the obtained Pd expressions can accurately describe the asymptotic detection performance of the proposed detector under spectral mismatches. We recall that, in case study A, the detector operating with $Q = 4$ represents the spectral *matched* detector investigated Chapter 3. Consequently, in Figure 4.2(a) also the exact expression derived in Chapter 3 (see eq. (3.31)) is reported, in solid dark blue line, for comparison. This additional comparison further confirms that (4.8) effectively approximates the closed-form solution when available, up to low Pd values.

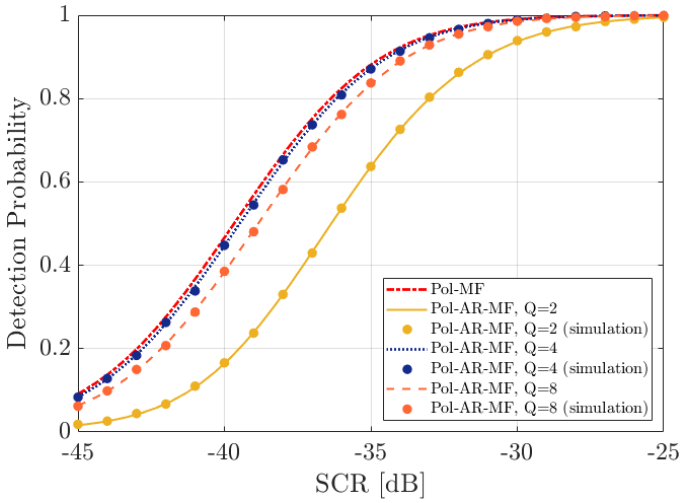

(a)

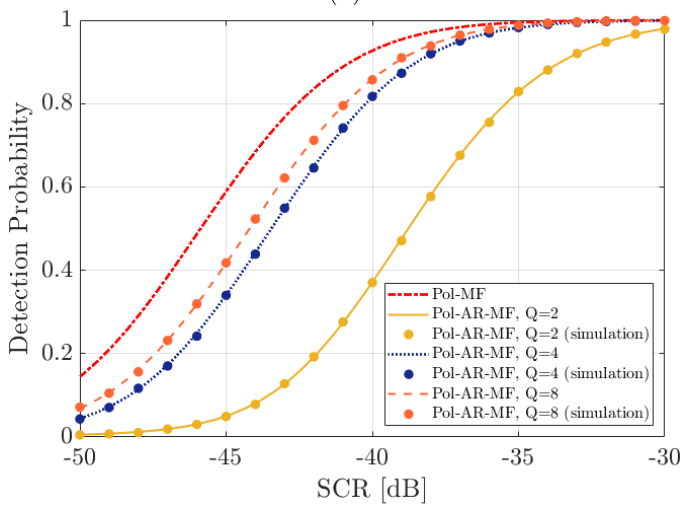

(b)

Figure 4.3: Pd versus SCR for $Pfa = 10^{-3}$, Swerling I target model and (a) case A, (b) case B

- As for Figure 4.1, the better the employed AR model approximates the true spectral characteristics of the disturbance, the better the target detection performance is. As expected, when considering case study A (Figure 4.2(a) and Figure 4.3(a)), the *matched* case of $Q = 4$ is the best performing. However, if a limited order mismatch occurs the resulting loss is still acceptable, especially when overestimating the order of the AR process (see the curves for $Q = 8$). In contrast, we see a larger performance degradation when underestimating the value of Q to be used. In the case under exam, the highest mismatch loss is obtained for $Q = 2$ and it is about 3dB with respect to the Pol-MF for both the non-fluctuating and fluctuating target models.
- When the case study B is considered (Figure 4.2(b) and Figure 4.3(b)), the detection performance of the clairvoyant Pol-AR-MF detector improves as Q increases. Note that

as for the *Pfa*, depending on the temporal correlation properties of the disturbance, the Q value required to obtain a good whitening and, subsequently, a limited target detection loss with respect to the Pol-MF, might significantly change. In the case under exam, a loss smaller than 3dB is reached for $Q \geq 4$ for both the non-fluctuating and fluctuating target model.

Although the considerations devised for Figure 4.1, Figure 4.2 and Figure 4.3 specifically refer to the considered case studies, similar comments apply to alternative cases obtained with a different choice of the relevant parameters. For instance, with reference to case study B, depending on the position of employed Doppler frequency value with respect to the filter temporal notch, the behaviour might not always be regular with respect to Q as the filter sidelobes might not be negligible.
However, we expect that a Q value that better fits the data exist and that this value grows as the temporal correlation of the disturbance grows and vice versa. For instance, Figure 4.5(a-b) shows the results obtained for case study B with the same parameters used in Figure 4.1(b) and Figure 4.3(b) but with a lower one-lag correlation coefficient value, i.e. $\varrho = 0.93$. In Figure 4.5(a), we plot the *Pfa* versus threshold for a grid of Q values while in Figure 4.5(b) we plot the *Pd* versus SCR for a Swerling I target model. By observing Figure 4.5(a-b), we confirm that the higher is Q, the better is the approximation of the Gaussian shaped power spectral density based on a multi-channel AR model. However, as a lower temporal correlation is employed, a lower number of taps should be adopted to achieve an acceptable approximation. In fact, Figure 4.5 (a) shows that $Q \geq 10$ allows a good approximation. Furthermore, Figure 4.5 (b) shows that using $Q = 4$, the clairvoyant Pol-AR-MF only yields approx. 1.5 dB loss with respect to the Pol-MF.

Summarizing, the analyses of *Pfa* and *Pd* of Sections 4.1 and 4.2 have clearly demonstrated that:

- Spectral model mismatches jeopardize the CFAR property for the proposed detection scheme even under asymptotic conditions. In other words, a practical strategy for the threshold setting (or at least a suitable approximation) is no longer available.
- The presence of spectral model mismatches might also yield significant degradations in term of target detection capability. The observed asymptotic loss is contained within few dBs when a limited mismatch is present. However, this might jeopardize the benefits of the proposed AR model-based approaches in practical cases where a spectral mismatch typically exists, and the observed loss should be summed up with the adaptivity loss deriving from an operation with a limited number P of secondary data.

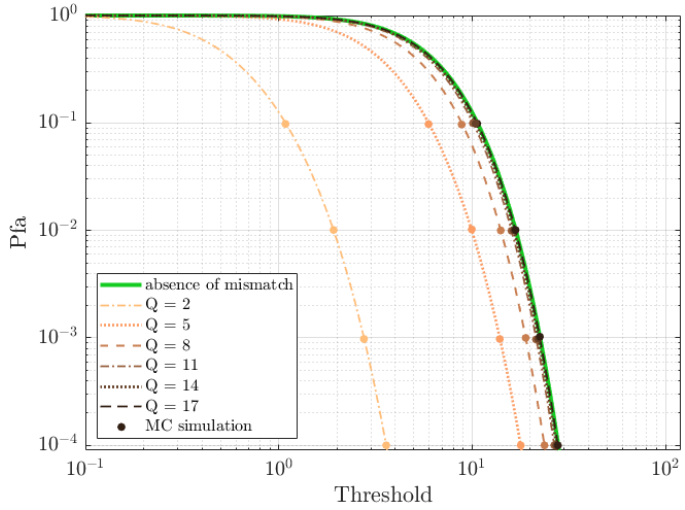

(a)

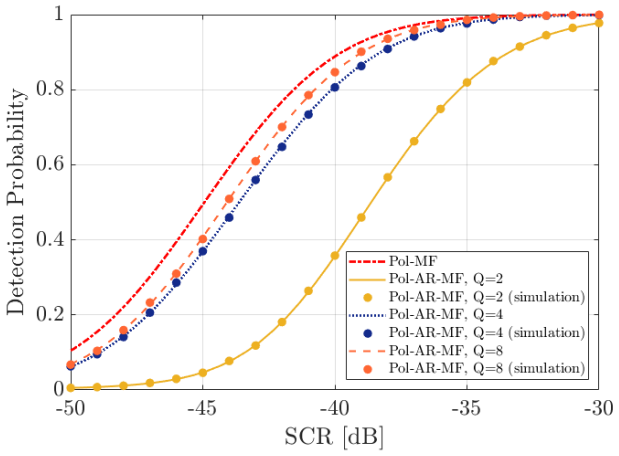

(b)

Figure 4.4: Performance evaluation for case study B with $\varrho = 0.93$ at $f_d = 0.28$: (a) *Pfa* versus threshold for different values of *Q*, (b) *Pd* versus SCR for Swerling I target model for $Pfa = 10^{-3}$

4.3 Modified AR model based Polarimetric Adaptive Matched Filter

We aim at identifying a proper modification to the proposed AR model based polarimetric detection scheme to make it robust to limited mismatches in the spectral characteristics of the disturbance. Most importantly, a practical strategy should be devised for the threshold setting in order to control the false alarm rate.

Notice that this is typically the case when no *a priori* information is available on the disturbance affecting the received data as in real-world radar systems. Moreover, despite effective approaches could be exploited to identify a suitable AR model that approximates

the actual disturbance characteristics [99], the resulting approximation might not be perfect thus resulting in a residual spectral model mismatch.

The theoretical developments in Section 4.1 clearly show that the considered mismatch is encoded in the covariance matrix $\mathbf{D_0}$ of the output random vector $\check{\mathbf{z}}_0$, namely the vector collecting the data after both polarimetric and temporal disturbance cancellation, which then undergoes the non-coherent integration across the polarimetric channels. This matrix tends to $2\mathbf{I}_L$ if the AR model adopted for the detector design matches or very well approximates the actual disturbance characteristics. In contrast, in the presence of spectral mismatches, $\mathbf{D_0}$ takes alternative forms that are unknown in practice.

Therefore, an asymptotically CFAR detection scheme can be obtained by cascading an additional whitening stage with the main stages of the proposed detector aiming at restoring a polarimetrically white output $\check{\mathbf{z}}_0$. Accordingly, the modified clairvoyant detector becomes:

$$T'_{Pol-AR-MF} = 2\,\mathbf{x}_0^H\mathbf{B}\,\mathbf{C}\,\mathbf{D}_0^{-1}\,\mathbf{C}^H\mathbf{B}^H\mathbf{x}_0 \underset{H_0}{\overset{H_1}{\gtrless}} \eta'_{AR-MF} \tag{4.12}$$

where the scaling factor 2 allows a direct comparison with the clairvoyant detector in Chapter 3. In the following, the detection scheme in (4.12) will be referred to as the modified polarimetric AR model based matched filter (Mod-Pol-AR-MF).

It is easy to verify that the distribution of the detector in (4.12) coincides with that obtained in the *matched* case considered in Chapter 3 if appropriate modifications are applied to the relevant parameters. Specifically, under the H_0 hypothesis, we might write $T'_{Pol-AR-MF} = \|\check{\mathbf{z}}_{0w}\|^2$, where $\check{\mathbf{z}}_{0w}$ is the whitened vector $\check{\mathbf{z}}_{0w} = \sqrt{2}\left(\mathbf{D}_0^{-1/2}\right)^H \check{\mathbf{z}}_0$ and $\check{\mathbf{z}}_{0w} \sim \mathcal{CN}(\mathbf{0}_{L\times 1}, 2\mathbf{I}_L)$. Therefore, the distribution of the test statistic is a central Chi-squared distribution with $2L$ degrees of freedom, i.e. $T'_{Pol-AR-MF} \sim \chi^2_{2L}(0)$, and the P_{fa} is given by (4.2).

Similarly, under the H_1 hypothesis, the theoretical P_d expressions derived in Chapter 3, for both the non-fluctuating and fluctuating target models exactly describe the detection performance of the modified detector if the target components are properly modified. Specifically, eq. (3.31) holds if the non-centrality parameter of the noncentral Chi-squared distribution of the test statistic is modified as $\varsigma' = \left\|\sqrt{2}\left(\mathbf{D}_0^{-1/2}\right)^H \mathbf{C}^H\mathbf{B}^H\mathbf{s}\right\|^2$. On the other hand, eq. (3.32) applies if $\gamma_0, \ldots, \gamma_{R-1}$ denote the $R \leq L$ distinct eigenvalues of the modified covariance matrix $\mathbf{D}_0'' = 2\left(\mathbf{D}_0^{-1/2}\right)^H \mathbf{D}_0'\ \mathbf{D}_0^{-1/2}$ where $\mathbf{D}_0'$ was defined in Section 4.1.2, which yields $\mathbf{D}_0'' = 2\mathbf{I}_L + 2\left(\mathbf{D}_0^{-1/2}\right)^H \mathbf{C}^H\mathbf{B}^H\,(\mathbf{t}\mathbf{t}^H \otimes \mathbf{M}_t)\,\mathbf{B}\mathbf{C}\ \mathbf{D}_0^{-1/2}$. These modifications basically encode the effect of the additional cancellation stage on the target and clutter components and must be carefully analysed in order to understand whether the modified detection scheme is able to limit the target detection loss due to disturbance spectral model mismatches.

To make the detection scheme in (4.12) adaptive, we assume that a set of P secondary data is available, $\mathbf{x}_p$, $p = 1, \ldots, P$, which are target-free, i.i.d and share the same statistic of $\mathbf{x_0}$ under the H_0 hypothesis.

As for the adaptive detector presented in Chapter 3, these data are first exploited to replace the unknown, though mismatched, parameters $\mathbf{A}_{mis}$ and $\mathbf{R}_{mis}$ within $\mathbf{C}$ and $\mathbf{B}$ with their ML estimates $\widehat{\mathbf{A}}_{mis}$ and $\widehat{\mathbf{R}}_{mis}$, obtained from the P training data.. Then the test statistic of the modified adaptive detector is built as:

$$T'_{Pol-AR-AMF} = 2\mathbf{x}_0^H \widehat{\mathbf{B}}\, \hat{\mathbf{C}}\, \widehat{\mathbf{D}}_0^{-1}\, \hat{\mathbf{C}}^H \widehat{\mathbf{B}}^H \mathbf{x}_0 \underset{H_0}{\overset{H_1}{\gtrless}} \eta'_{AR-AMF} \tag{4.13}$$

where the output covariance matrix $\mathbf{D_0}$ is also estimated from the secondary data once they underwent the same filtering stages applied to the primary data. In particular, according to this doubly adaptive detection scheme, we define the output of the first adaptive stage for the p-th input vector as $\boldsymbol{\zeta}_p = \hat{\mathbf{C}}^H \widehat{\mathbf{B}}^H \mathbf{x}_p$, and we build an estimate of $\mathbf{D_0}$ as $\widehat{\mathbf{D}}_0 = \frac{1}{P}\sum_{p=1}^{P} \boldsymbol{\zeta}_p \boldsymbol{\zeta}_p^H$. We observe that the secondary data to be exploited for the estimation of matrix $\mathbf{D_0}$ should not necessarily coincide with the secondary data exploited to build the first cancellation stage of the detector.

Notice that, when $L = 1$, the adaptive transformation obtained by using the inverse of matrix $\widehat{\mathbf{D}}_0$ would simply correspond to the scalar scaling factor of a Cell-Average CFAR autogate. In fact, we would have $\widehat{\boldsymbol{D}}_0^{-1} = \varpi^{-1}$, where ϖ represents an estimate of the residual clutter power. This is obtained using P training data that underwent the filtering stages based on matrices $\widehat{\boldsymbol{B}}$ and $\widehat{\boldsymbol{C}}$, i.e. $\varpi = \frac{1}{P}\sum_{p=1}^{P} |\zeta_p|^2$ with $\zeta_p = \widehat{\boldsymbol{C}}^H \widehat{\boldsymbol{B}}^H \mathbf{x}_p$ ($p = 1, \ldots, P$).

When $L > 1$, the adaptive transformation obtained by using the inverse of matrix $\widehat{\mathbf{D}}_0$ corresponds to an additional filtering stage based on the polarimetric information extracted at the output of the previous filtering stages. The introduced whitening stage is expected to make the false alarm control capability more robust against residual disturbance contributions that endure the first cancellation stage, as discussed in the following.

Under asymptotic conditions, $\widehat{\mathbf{A}}_{mis}$ and $\widehat{\mathbf{R}}_{mis}$ are asymptotic, though mismatched, estimates obtained from an infinite number of secondary data [58]. Consequently, the distribution of the test statistic of the adaptive detector in (4.13) tends towards that of the clairvoyant detector in (4.12) based on mismatched parameters.

Under asymptotic conditions, the distribution of the test statistic of the adaptive detector in (4.13) tends towards that of the clairvoyant detector in (4.12). Therefore, when exploiting many training data, the performance of the modified polarimetric AR model based adaptive matched filter (Mod-Pol-AR-AMF) can be approximated by its asymptotic performance, as detailed above. Note that the CFAR property is restored for the modified adaptive detector at least in the asymptotic regime. In this regard, the analyses in Chapter 3 have shown that a number P of training data equal to QL is typically enough to guarantee the asymptotic

condition for the Pol-AR-AMF when M is sufficiently high since the estimation of parameters $\widehat{\mathbf{A}}$ and $\widehat{\mathbf{R}}$ benefits from the average performed both across the secondary data and the temporal observations within the CPI.

However, this consideration does not apply to the additional stage included in the Mod-Pol-AR-AMF proposed in this Section. In fact, this stage involves the estimation and inversion of a $L \times L$ matrix $\widehat{\mathbf{D}}_0$, based on the available P training data. Therefore, an additional adaptivity loss is expected when operating with finite P, and this might result in a limited control of the *Pfa* and degradations of the target detection capability.

To overcome the first issue, the fluctuations in the estimation of matrix $\widehat{\mathbf{D}}_0$ can be considered in the resulting *Pfa* expression. To this purpose we make the simplified assumption that the first adaptive cancellation stage meets the asymptotic condition, namely the outputs $\boldsymbol{\zeta}_p$ of this adaptive stage has the same distribution of the output $\check{\mathbf{z}}_p = \mathbf{C}^H \mathbf{B}^H \mathbf{x}_p$ of the clairvoyant filter. Specifically, under the H_0 hypothesis, we have $\boldsymbol{\zeta}_p \sim \mathcal{CN}(\mathbf{0}_{L\times 1}, \mathbf{D}_0)$, being $\boldsymbol{\zeta}_p$, $p = 0, \ldots, P$, a set of statistically independent vectors. Under such simplified assumptions, the probability density function of the test statistic of the adaptive detector in (4.13), $T'_{Pol-AR-AMF} = 2\,\boldsymbol{\zeta}_0^H\, \widehat{\mathbf{D}}_0^{-1} \boldsymbol{\zeta}_0$, is well known in the technical literature for multivariate analysis as the central F-distribution [99]. Specifically, we have $\frac{P-L+1}{2LP} T'_{Pol-AR-AMF} \sim F(2L, 2(P-L+1))$ and a better approximation of the *Pfa* can be obtained accordingly:

$$P_{fa} = \frac{(1-\kappa)^{P-L+1}}{\Gamma(P-L+1)} \sum_{l=0}^{L-1} \frac{\Gamma(P-l)}{\Gamma(L-l)} \kappa^{L-l+1} \tag{4.14}$$

being $\eta = 2P \frac{\kappa}{(1-\kappa)}$ the detection threshold.

The capability to control the false alarm rate based on (4.14) will be investigated in the following against both numerical and real data aiming at understanding the reliability of the adopted assumptions in practical cases. In turn, such analysis will also prove the CFAR property of the Mod-Pol-AR-AMF even when operating with finite P. In addition, it is expected that the additional adaptive stage included in the Mod-Pol-AR-AMF might yield a non-negligible effect on its target detection capability. The benefits/drawbacks of this effect will be studied in the following Section through numerical analysis and in Chapter 5 through experimental data analysis.

4.4 Numerical Results

First, we investigate the false alarm rate control provided by the Mod-Pol-AR-AMF when using (4.14) for threshold setting. Specifically, we plot in Figure 4.5 the measured *Pfa* versus the nominal *Pfa* for case study A and different values of Q, namely $Q = 2$, 4, 8 and 12, using different training data size, namely $P = 4$, 16 and 192.

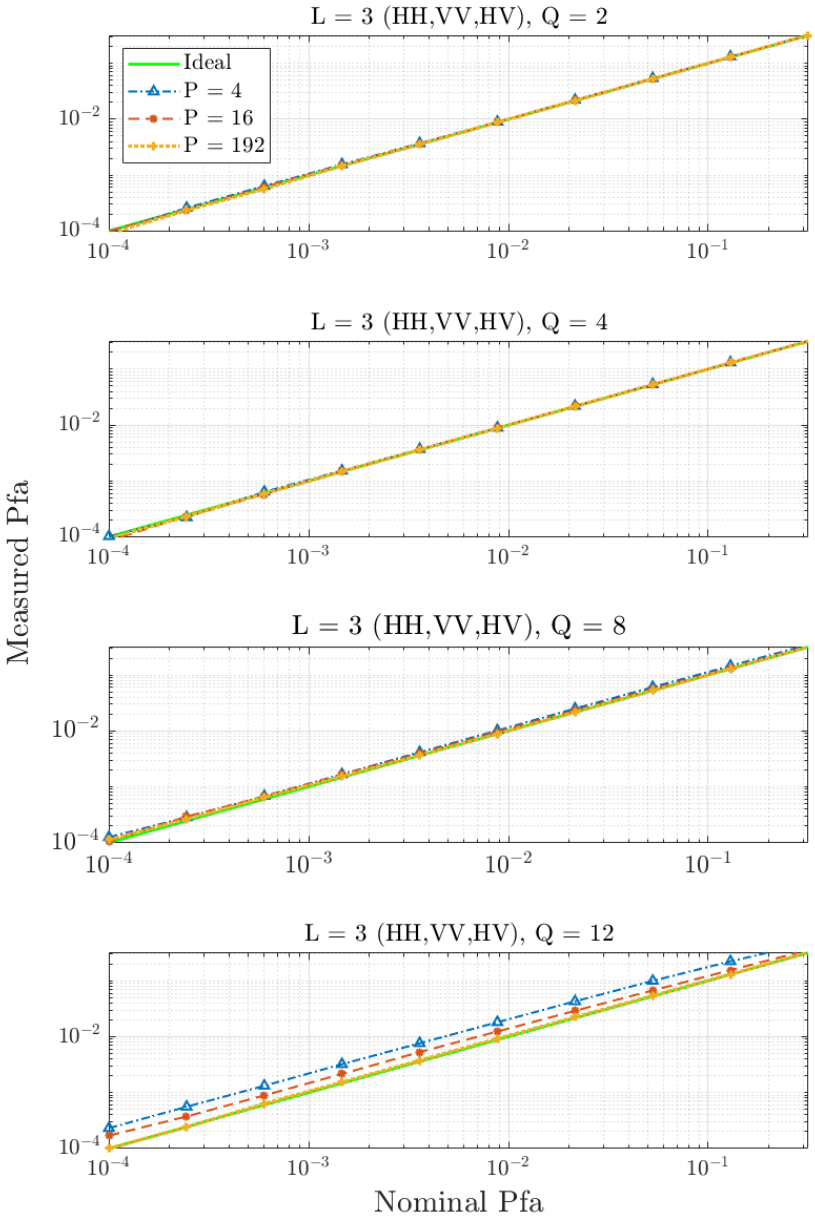

Figure 4.5: Measured *Pfa* versus nominal *Pfa* for $M = 32$, $L = 3$ (HH,VV,HV), different Q values and different training data size

We recall that (4.14) represents an approximated expression of the *Pfa* since it relies on perfect estimates of the matrices exploited for the first adaptive stage whereas it only accounts for the fluctuations in the second adaptive stage.

Figure 4.5 shows that such simplified approach allows a good control of the actual *Pfa* up to reasonably low false alarm rates, at least when the number P of secondary data is enough to provide approximate asymptotic conditions at the first adaptive stage. In this regard, we observe that some degradations appear when operating with $Q = 12$ and a limited training

data size. Below this value, the capability of controlling the *Pfa* is ensured both when a spectral model mismatch occurs and when it does not, i.e. $Q = 4$.

For the performance evaluation under the H_1 hypothesis, we consider the same Swerling I target model described in Section 4.2 and we plot the results in Figure 4.6(a-b) for case studies A and B, respectively. Specifically, we report the target detection probability versus SCR for the Mod-Pol-AR-AMF with $Q = 5$ and $P = 16$ or 192. Notice that, with the adopted value for the number Q of taps, the detection scheme operates under spectral mismatched conditions in both considered case studies. In each sub-figure, we use the Pol-MF as a benchmark for the performance evaluation while the performance obtained with the adaptive Pol-GLRT, working with $P = 2ML = 192$ secondary data, are also reported for comparison.

As it is apparent from Figure 4.6(a-b), the Mod-Pol-AR-AMF with $Q = 5$ outperforms the Pol-GLRT when operating with the same number of secondary data. In fact, with $P = 192$, the proposed detector approximates its asymptotic version and provides performance that is largely comparable to the ideal Pol-MF. The loss with respect to the benchmark is negligible in case study A (Figure 4.6(a)) where a limited mismatch exists between the actual spectral characteristics of the disturbance and the model adopted by the detection scheme. In contrast, a slightly higher loss is observed in case study B (Figure 4.6(b)) since the detector is attempting to approximate a Gaussian spectral shaped disturbance with a multi-channel AR process of order $Q - 1 = 4$. Nevertheless, the resulting loss is smaller than 1dB in the considered case study. When significantly reducing the number of secondary data, a consistent degradation is obtained with the Mod-Pol-AR-AMF which is mostly attributed to the fluctuations in the estimation of matrix $\widehat{\mathbf{D}}_{\mathbf{0}}$, namely the second adaptive stage. In fact, following the results of Chapter 3, $P = 16$ is expected to provide accurate estimates of the matrices required at the first adaptive stage when operating with $Q = 5$ and $M = 32$.

Anyway, thanks to the limited adaptivity loss, which is the typical benefit of parametric approaches (see e.g. [32],[44],[46],[74],[99]) ,the Mod-Pol-AR-AMF is still able to guarantee better performance with respect to the Pol-GLRT operating with a much larger training set in both the considered case studies. We incidentally observe that this result is obtained with a significantly reduced computational effort.

To complete the analysis, in Figure 4.7(a-b) we compare different polarimetric detectors in terms of SCR loss with respect to the Pol-MF, measured at $Pd = 0.9$. The Mod-Pol-AR-AMF is applied with a grid of Q values and different P values. The comparative analysis also includes the performance of the Pol-AR-MF in (4.1) and the Mod-Pol-AR-MF in (4.12), which are representative of the asymptotic performance of the original proposed detector and the newly modified detection scheme, respectively.

As expected, regardless of the considered case-study, the Pol-GLRT yields a loss that only depends on the data size LM and number P of secondary data. This loss is equal to 3.1dB and is shown as a horizontal line in Figure 4.7(a) and Figure 4.7(b).

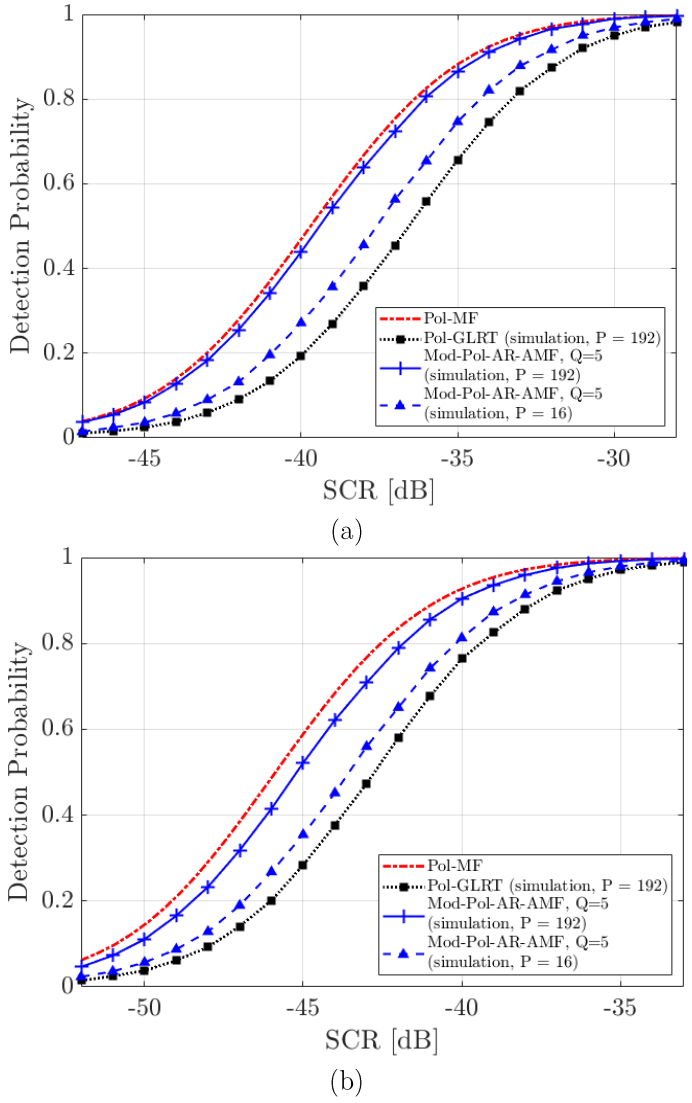

Figure 4.6: Pd vs SCR for the Mod-Pol-AR-AMF against a Swerling I target model in (a) case study A, and (b) case study B.

When comparing the clairvoyant detectors, namely the Pol-AR-MF and the Mod-Pol-AR-MF, we observe that the additional cancellation stage included by the modified scheme allows to limit the spectral mismatch loss investigated in Section 4.2. Specifically, when the detector is fed with an AR disturbance process of order $\bar{Q} - 1$ (case study A, Figure 4.7(a)), the smallest asymptotic loss with respect to the Pol-MF is observed when using $Q = \bar{Q} = 4$ with both detectors; we recall that this loss in this case is solely due to the border effect arising from a block-based implementation of the detection scheme as discussed in Chapter 3.

In contrast, when underestimating or overestimating the order of the AR process, the Mod-Pol-AR-MF limits the asymptotic loss thus making the resulting scheme more robust to AR model order mismatches with respect to the Pol-AR-MF.

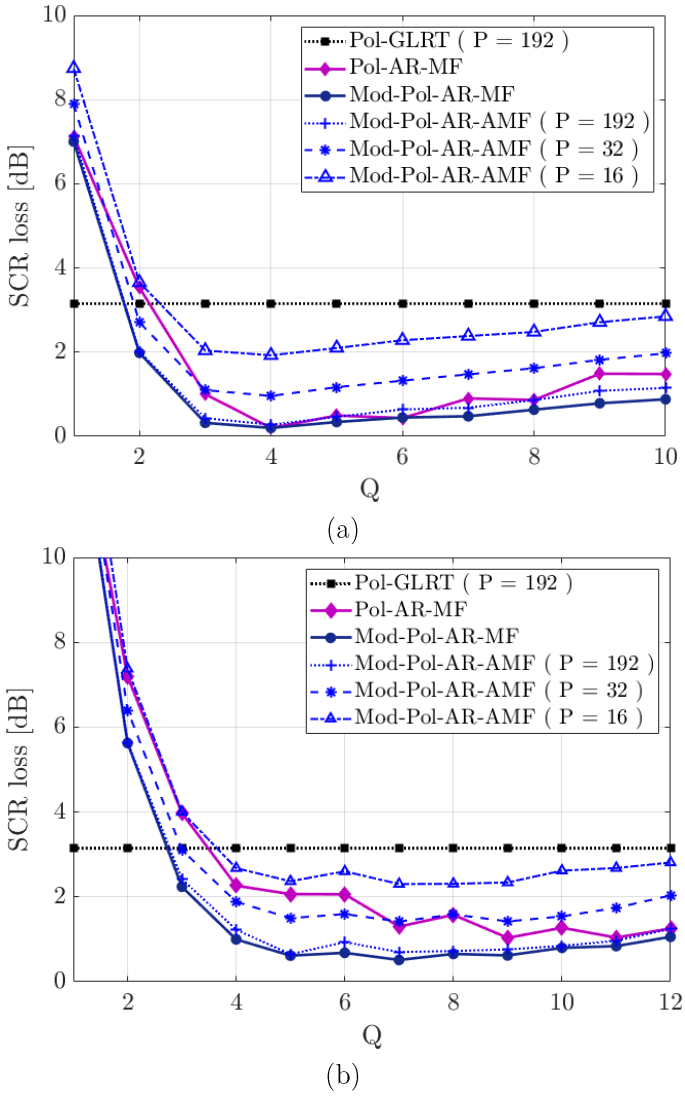

Figure 4.7: SCR loss versus Q for differrent detection schemes against a Swerling I target model in (a) case study A, and (b) case study B

Similar considerations apply to the asymptotic performance obtained in case-study B (Figure 4.7(b)) for a Gaussian spectral shaped disturbance. In this case, the asymptotic performance of the Pol-AR-MF slowly improves as the number of taps Q increases. In contrast, using the modified detector a much smaller Q is required to achieve negligible asymptotic loss with respect to the Pol-MF; for instance, in the considered case study B, further increasing Q beyond $Q = 5$, does not yield significant improvements in terms of target detection capability as the reduced spectral mismatch loss is compensated by a larger border effect when a block-based implementation is considered for the proposed scheme.

It is then interesting to understand the effect of the additional adaptivity loss when operating with a finite number P of secondary data based on the proposed Mod-Pol-AR-AMF. As is apparent from Figure 4.7(a-b), the Mod-Pol-AR-AMF with $P = 192$ basically

reaches the asymptotic performance for all the considered values of the number Q of taps. Therefore, we can conclude that when operating with the same number of secondary data, the proposed Mod-Pol-AR-AMF outperforms the performance of the Pol-GLRT for almost every considered value of Q. When reducing the size of the training set, an additional adaptivity loss is experience by the Mod-Pol-AR-AMF (see the curves for $P = 32$ and $P = 16$). Notice that the additional loss is almost independent of the number of taps since it is mostly due to the fluctuations in the estimation of the $L \times L$ matrix $\widehat{\mathbf{D}}_{\mathbf{0}}$ to be used in the second adaptive stage, which is the price to be paid to benefit from the observed advantages. Nevertheless, in the considered case studies, the Mod-Pol-AR-AMF retains its performance improvement over the Pol-GLRT even when using a number of training data of $P = 16$, namely 12 times smaller than the one used for the Pol-GLRT.

4.5 Summary

In this Chapter, the performance of the polarimetric adaptive detector presented in Chapter 3 has been studied for the case of an input disturbance that does not perfectly match the AR model used for the derivation of the detection test. The theoretical and simulated analyses have revealed the limitations of the original detector under such conditions and these include the loss of the asymptotic CFAR property and subsequent degradations in terms of target detection capability. Consequently, an appropriate modification to the devised detector has been introduced to make it robust to typical spectral mismatches occurring in practical situations.

The effectiveness of the resulting detection scheme has been demonstrated against simulated data, where the modified detector was proven to guarantee a remarkable control of the false alarm rate and target detection performance outperforming the traditional detection schemes. In Chapter 5, the effectiveness of the proposed detection scheme is investigated against experimental data.

Chapter 5
Polarimetric adaptive target detector based on a multi-channel AR model: Experimental Validation

In this Chapter the effectiveness of the polarimetric adaptive detection scheme introduced in Chapter 3 and Chapter 4 is investigated against experimental data. First, in Section 5.1 real data collected by mean on a polarimetric active radar system are used and the performance assessment is carried out also in comparison with the conventional polarimetric adaptive detection strategies considered in the previous Chapters. Then, in Section 5.2, a dataset collected by means of a FM radio-based PCL system are used. In the latter case, some reasonable approximations are introduced in Section 5.3, in order to reduce the computational burden required by the direct implementation of the Mod-Pol-AR-AMF and enable an extensive analysis over the entire dataset.

5.1 Performance assessment against real active radar data

The sea clutter radar measurements employed in this Section have been collected at the Osborne Head Gunnery Range (OHGR), Dartmouth, Nova Scotia, Canada, using the McMaster IPIX radar [47]. The IPIX radar is a polarimetric radar system that alternatively transmits bursts of pulses in each of two linear polarizations (H and V) and receives the corresponding back-scattered echoes at both polarizations with two parallel receiving channels. The experiment description as well as information concerning the radar parameters, the sea state, etc. are reported in [30],[47].

The sea clutter data collected my means of the IPIX radar have been widely used in the literature, see e.g. [27],[31],[34], [38],[39],[47]. Specifically, the results reported in this work refer to the target-free data file *starea4* collected on November 6, 1993. The auto- and cross-spectra of the HH, VV and HV channels, averaged out over the range bins, are reported in Figure 5.1 in black, blue and red, respectively.

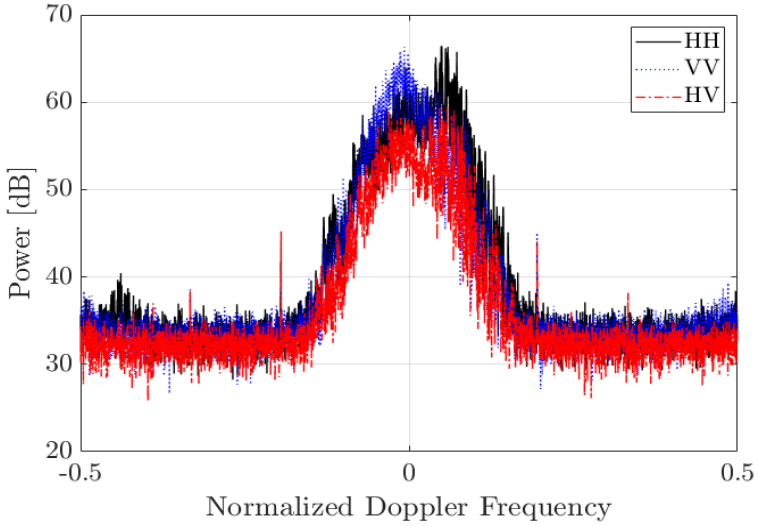

Figure 5.1: Clutter power spectra at *starea4* data file

In order to preliminary investigate the capability of the Mod-Pol-AR-AMF of discriminating targets against the background, we first consider a sample data sub-set that collects the range sweeps from three polarimetric channels, i.e. $L = 3$ (HH, VV, HV) at $M = 32$ consecutive pulses.

Before applying the proposed detector, a fictitious point-like target is injected at range cell 6 and $f_d = 0.25$. As for the simulated analysis, the target complex amplitudes are set as $\boldsymbol{\alpha} = a_t\left[1 \quad e^{j\Delta\phi_{HH/VV}} \quad \sqrt{\xi_t}e^{j\Delta\phi_{HH/HV}}\right]^T$, with a_t selected to guarantee SCR at the first polarimetric channel equal to SCR = -25dB, $\xi_t = 10$, $\Delta\phi_{HH/VV} = \pi/4$, and $\Delta\phi_{HH/HV} = \pi/2$.

We report in Figure 5.2(a-d) the normalized range-Doppler maps, resulting after applying the Mod-Pol-AR-AMF across the available range cell with different Q values, namely $Q =$ 1,2, 4 and 8. Figure 5.2 shows that, when using Mod-Pol-AR-AMF with $Q = 1$ (see Figure 5.2 (a)), the clutter contribution at the considered CPI is such that the target is very unlikely to be discriminated. Then, as Q increases, the disturbance level is progressively reduced, and the target peak becomes more evident thus it could be easily distinguished from the background. The performance is comparable from $Q = 2$ to $Q = 5$, although we do not show all the cases here for brevity. Afterwards, as the number of taps further increases, the background level starts slowly increasing again and Figure 5.2 (d) shows an example for Q = 8. Similar results are obtained when considering different CPIs within the available data. Therefore, in the following, we focus our analysis on a limited set of choices for the number of taps Q which also represent suitable values for practical applications.

For a complete performance assessment, we carried out an extensive analysis by evaluating the false alarm rate control capability as well as the target detection performance over the entire data set. In Figure 5.3, we plot the measured *Pfa* versus the nominal *Pfa* for three values of Q namely $Q = 3$,4 and 5 and two different numbers of training data, namely $P =$ 192 and 16. In each sub-plot, we show two different results.

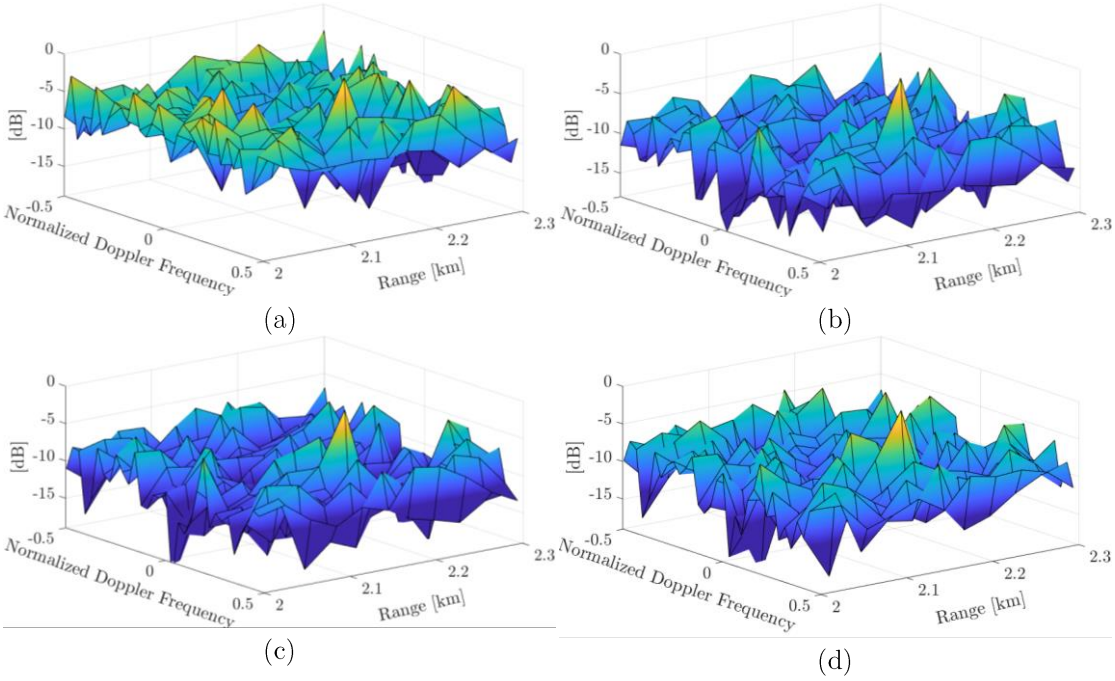

Figure 5.2: Range – Doppler maps after using the Mod-Pol-AR-AMF with P = 32 and (a) $Q = 1$ (b) $Q = 2$ (c) $Q = 4$ (d) $Q = 8$.

In magenta, we plot the results obtained when using the original proposed detector Pol-AR-AMF by setting the detection threshold according to (4.2) namely by assuming that (i) a perfect matching exists between the spectral model adopted to build the detector and the actual disturbance characteristics and (ii) the Pol-AR-AMF is working in the asymptotic regime, where the employed *Pfa* expression is valid. Figure 5.3 clearly shows that the latter assumptions are too strict and that (4.2) would not provide an acceptable capability of controlling the false alarm rate for any value of P. However, these results also show that, among the set of Q values considered in Figure 5.3, the choice of $Q = 4$ appears to be the one that would yield a better false alarm rate control based on the above strategy. In turn, this suggests that an AR (3) model provides a reasonable approximation of the spectral characteristics of the data at this data file [30].

In the same figures, the dark blue lines show the results obtained with the Mod-Pol-AR-AMF, when selecting the detection threshold according to (4.14). Figure 5.3 confirms that the modified detector is robust to both spectral mismatches and non-asymptotic conditions since a quite good control of the *Pfa* is guaranteed for all the considered combinations of values for Q and P up to $Pfa = 10^{-3}$. Incidentally, we note that lower *Pfa* values could not be estimated due to the limited size of the considered data set. Afterwards, the *Pd* was investigated by injecting a fictitious Swerling I target into the sea clutter measurements before applying the proposed Mod-Pol-AR-AMF.

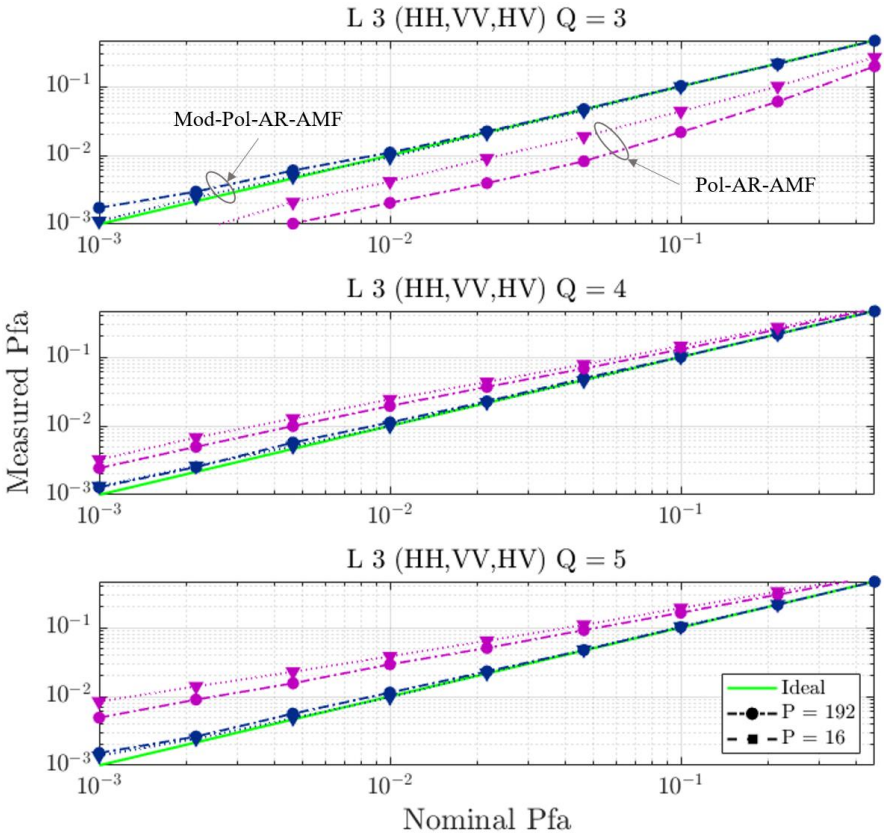

Figure 5.3: Measured *Pfa* versus nominal *Pfa* for $M = 32$, $L = 3$ (HH,VV,HV), different Q values and different training data

The same parameters adopted in Section 4.2 have been used for generating the target amplitudes across the polarimetric channels. We plot the results in Figure 5.4 for $Pfa = 10^{-3}$ and $Q = 4$, using different numbers of polarimetric channels, i.e. $L = 1$ (HH), $L = 2$ (HH,VV), $L = 3$ (HH,VV,HV), and different amount of secondary data. For comparison, we also report the performance of the Pol-GLRT operated using $P = 2ML$ in dotted black.

By observing Figure 5.4 we notice that as the number of available polarimetric channels increases, the target discrimination capability increases and the performance of all polarimetric adaptive detectors improves. In particular, due to the higher SCR at the cross-polarized channel, using $L = 3$ (HH, VV, HV) yields a considerable performance improvement.

When comparing the Mod-Pol-AR-AMF and the Pol-GLRT, the results in Figure 5.4 largely confirms the simulated analyses. In fact, we observe that, using the same number of training data ($P = 2ML$) the Mod-Pol-AR-AMF remarkably outperforms the Pol-GLRT. This consideration applies even when using much fewer training data ($P = 32$ or 16), especially when $L = 1$ or $L = 2$ polarimetric channels are considered. As expected, the advantage of the Mod-Pol-AR-AMF over the Pol-GLRT slightly reduces with $L = 3$; however, it still is the most suitable approach against the considered data set.

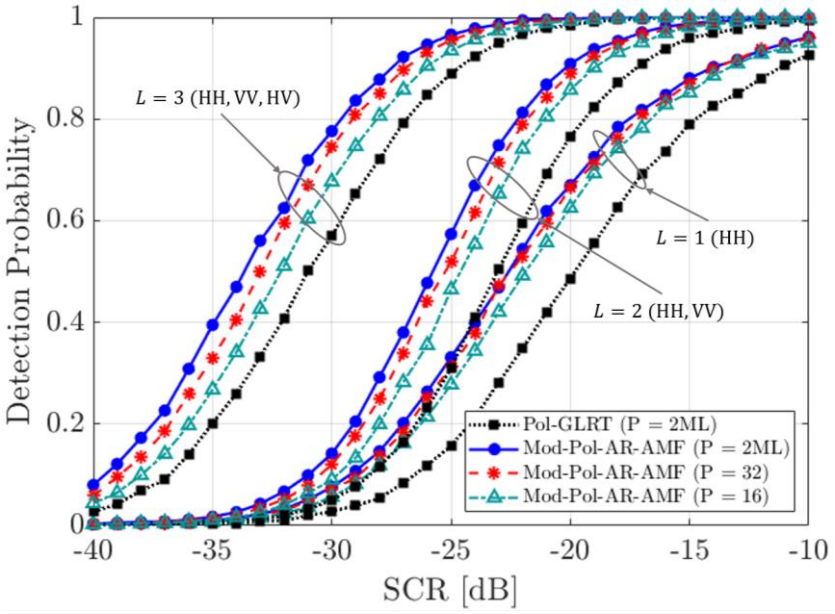

Figure 5.4: *Pd* versus SCR with $Pfa = 10^{-3}$, M = 32 with different polarimetric channels for Q = 4.

Finally, in Figure 5.6 we study the detection performance as a function of the Doppler frequency and the target polarimetric cross-correlation coefficient ρ_t. Specifically, we consider $Pfa = 10^{-3}$ and we inject a fictitious point like target using the same model adopted for Figure 5.4 with SCR = –20 dB. In Figure 5.6 (a), we report the *Pd* obtained with the proposed Mod-Pol-AR-AMF as a function of ρ_t and f_d with $P = 2ML = 128$. In Figure 5.6 (b) we focus on the extreme values of ρ_t and we compare the Mod-Pol-AR-AMF with $P = 128$ against the Pol-GLRT using the same training data and the Mod-Pol-AR-AMF operated using $P = 16$. Specifically, continuous lines refer to the case $\rho_t = 0$ while dashed lines are for $\rho_t = 0.99$. In both subfigures, a logarithmic scale has been used to enhance the difference at high *Pd* values. Figure 5.6 (a-b) confirms that the lower is the target polarimetric correlation, the narrower is the cancellation notch resulting from the Mod-Pol-AR-AMF. This result is well in line with the simulated analysis reported in Chapter 3, however here the difference between the case of $\rho_t = 0$ and $\rho_t = 0.99$ is slightly reduced, revealing a lower polarimetric correlation for the clutter [83].

5.2 Performance assessment against real PCL data

Let us consider a FM radio-based PCL system, equipped with L receiving channels, connected to differently polarized surveillance antennas. For such application, the proposed Mod-Pol-AR-AMF can be applied with only a few adjustments that can be easily accommodated into the general signal model adopted in Chapter 3.

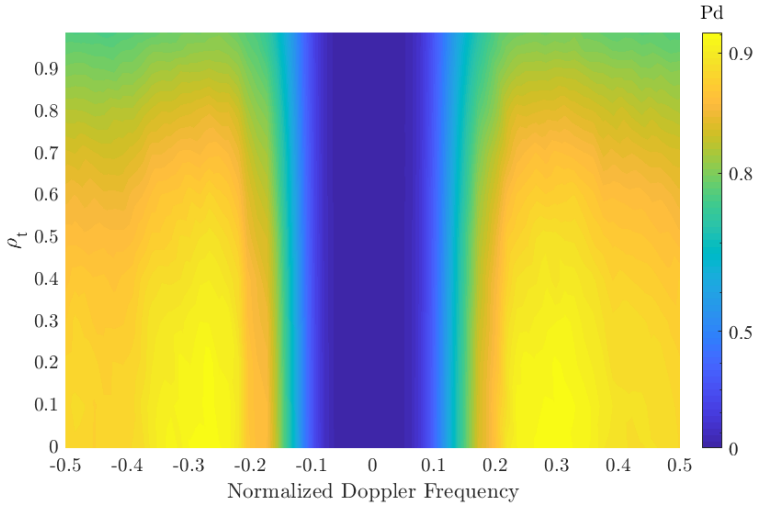

(a)

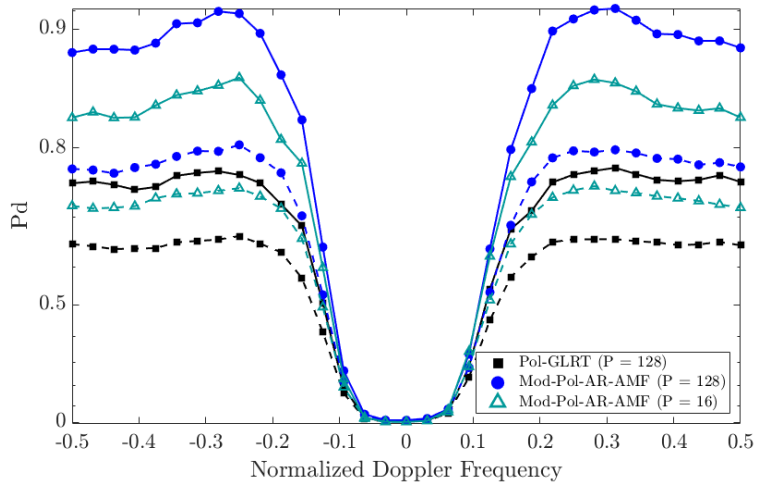

(b)

Figure 5.5: *Pd* for SCR = -20 dB, $Pfa = 10^{-3}$, L = 2 (HH, VV), M = 32:
(a) *Pd* for Mod-Pol-AR-AMF (P = 128) as a function of f_d and ρ_t
(b) *Pd* versus f_d for $\rho_t = 0$ (continuous lines) and $\rho_t = 0.99$ (dashed lines).

Specifically, in this case, the M 'temporal observations' are provided by M consecutive samples of the received signals included in the CPI. Correspondingly, the temporal steering vector $\mathbf{t}$ coincides with M samples of the signal collected at the reference channel.

According to the processing scheme introduced in Section 2.1, the signals collected by different antennas separately undergo the disturbance (direct signal and multipath) cancellation stage. Depending on the availability of one or more differently polarized reference antennas, this stage can be performed according to either the ECA [22] or its polarimetric version (P-ECA) [18].

Once this stage has been performed, L sequences of samples are made available corresponding to the polarimetric channels deployed.

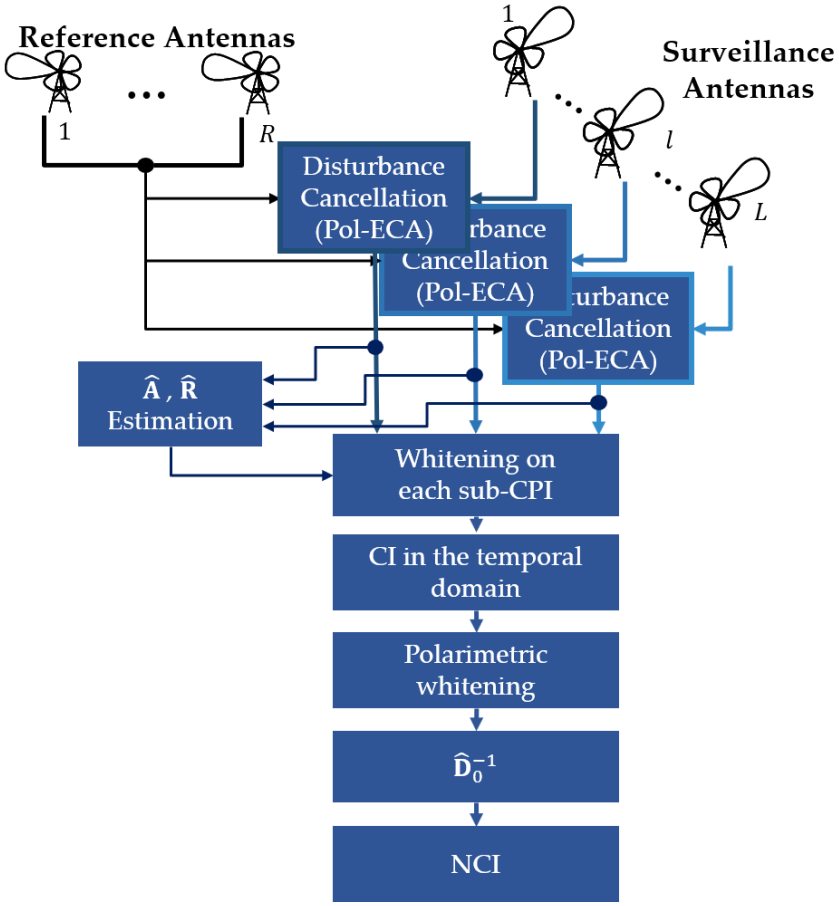

Figure 5.6: Sketch of the Mod-Pol-AR-AMF for PCL systems

We arrange the L outputs extracted at the m-th time lag into an L-dimensional vector $\mathbf{x_0}(m)$, $m = 0, \ldots, M-1$ in (3.1), reported here for convenience:

$$\mathbf{x_0}(m) = \left[x_0^{(0)}(m) \ldots x_0^{(1)}(m) \ldots x_0^{(L-1)}(m)\right]^T \tag{5.1}$$

being the M 'temporal observations' provided by M consecutive samples of the received signals included in the CPI. We recall that passive radars typically use long CPI (in the order of seconds) to attain desired levels of SNR.

Consequently, the number of samples M is usually very high (in the order of $\mathbf{10^6}$) and this prevents the direct application of the Pol-GLRT and the Pol-AMF due to (i) the unfeasible requirement of training data, and (ii) the prohibitive complexity of required computations.

In contrast, suitable estimates of matrices $\mathbf{A}$ and $\mathbf{R}$ to be used in the Mod-Pol-AR-AMF can be obtained based upon proper signal fragments, assuming that the target contribution is negligible with respect to the competing disturbance. A sketch of the entire Mod-Pol-AR-AMF strategy applied to PCL system is reported in Figure 5.6.

5.2.1 Acquisition campaign

The acquisition campaign has been conducted near Fiumicino Airport, in Italy, exploiting a FM radio transmitter located in Monte Cavo, approx. 35 km from the receiver site (see Figure 5.7). Two dual-polarized log periodic antennas were used (see Figure 5.8(a)), being each one equipped with two independent outputs, one vertical (V) one horizontal (H) polarized. Specifically, one of them was steered toward the exploited IO and employed to collect the V and H polarized versions of the reference signal. The other antenna was pointed toward the area to be monitored and the two outputs gathered the V and H polarized versions of the surveillance signal.

The data set consists of 2060 sequential data files (approx. 80 minutes covered), each one containing a 1.1 s registration of the signals simultaneously collected by different antennas at different carrier frequencies. The employed PCL prototype is based on a direct RF sampling approach and exploits the ICS-554 PMC module (GE Fanuc Embedded Systems) (see Figure 5.8 (b)).

Figure 5.7: Sketch of the acquisition campaign geometry

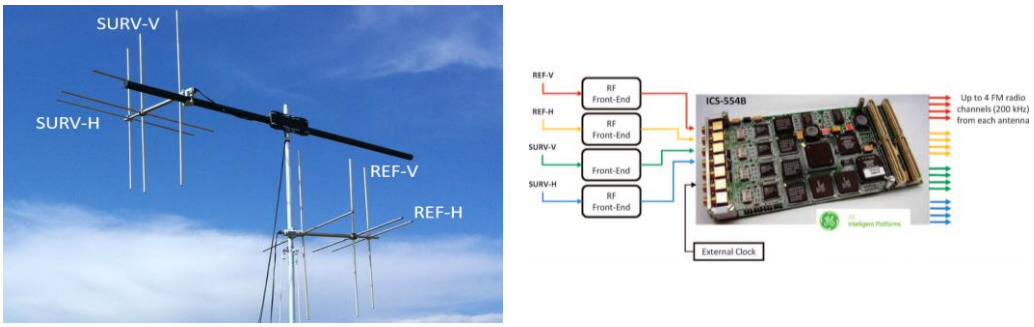

(a) (b)

Figure 5.8: Acquisition Campaign equipment:
(a) Dual-polarized antennas; (b) Multi-channel PCL prototype

This module consists of four 14-bit ADCs sampling synchronously the properly amplified and filtered analogue signals from up to four input channels. Simultaneous down conversion of up to 16 arbitrary signal bands (e.g. 16 FM radio channels) is provided by four Graychip GC4016 quad digital down-converters (DDC). The described setup allows collecting data from up to four different FM radio channels, reported in Table 5.1 each one from four different antennas. The air-truth for the same air space has been provided by the SBS-1 real time virtual radar, a portable low-cost Mode-S/ADS-B receiver.

Table 5.1
Collected FM radio channels

FM Ch ID	Carrier Frequency [MHz]	FM Radio Broadcast	Tx Polarization	Tx Power [kW]
FMCh1	91.2	RAI R.2	H	80
FMCh2	92.4	RTL	V	15
FMCh3	94.5	SUBASIO	V	15
FMCh4	103.0	RDS	V	30

5.2.2 Results

In order to investigate the effectiveness of the proposed detection scheme, we consider 50 consecutive data files and the FM channel at 94.5 MHz and we report the raw PCL detections in Figure 5.9 and Figure 5.10 for different detection schemes. In both figures we report in black the air-truth corresponding to the targets of opportunity that were present at the time. All the detections are reported in grey plots while the red ones represent the PCL detections that have been correctly associated to the available ATC data. The number of training data used to estimate matrices $\widehat{\mathbf{A}}$ and $\widehat{\mathbf{R}}$ has been set equal to 200 while the estimation of matrix $\widehat{\mathbf{D}}_{\mathbf{0}}$ is performed using 32 secondary data surrounding the CUT in the bistatic range-Doppler plane. A $Pfa = 10^{-5}$ has been used.

In Figure 5.9 we report the results obtained when the single-pol channels are separately employed and processed according to a conventional single-pol PCL processing scheme.In Figure 5.10 we report the results obtained when the polarimetric information is exploited acccording to (a) the P-GLRT presented in Chapter 2 and (b) the proposed Mod-Pol-AR-AMF using $Q = 3$. We recall that a comparison with the Pol-GLRT [83] and the Pol-AMF [26] is not possible.

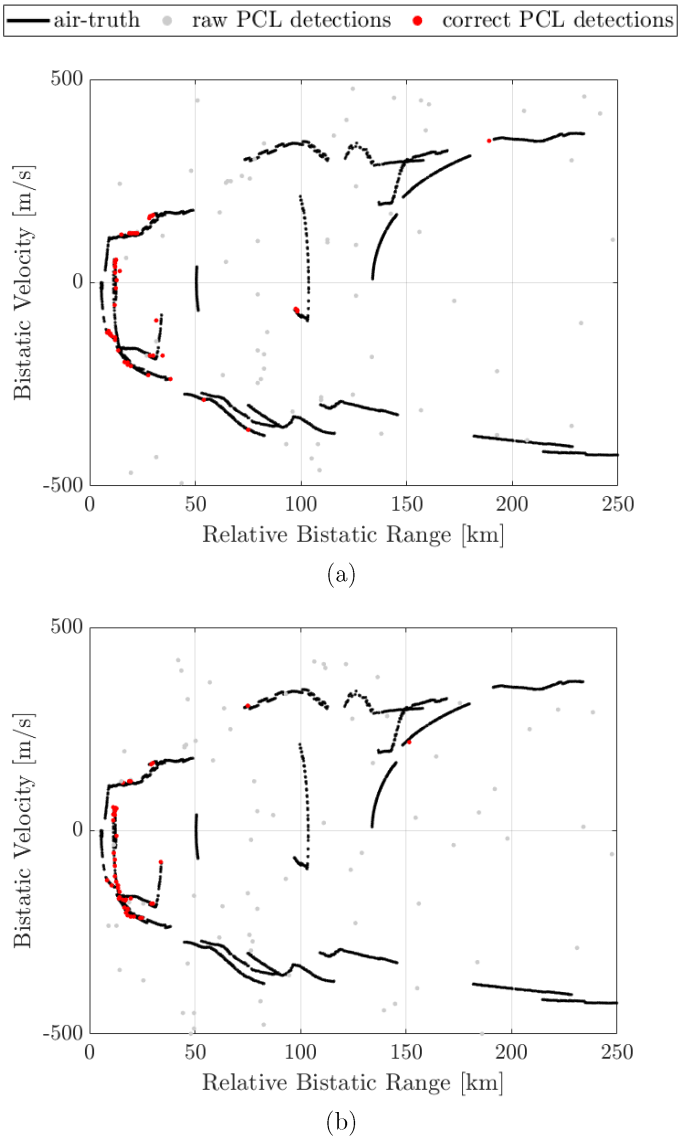

Figure 5.9: Raw PCL detections over 50 consecutive datafiles using: (a) single-pol H and (b) single-pol V

By observing Figure 5.9 and Figure 5.10, the following considerations are in order:

- The two single polarimetric channels yield to different results. For this set of datafiles, the single-pol V in Figure 5.9(b) is better performing with respect to the single-pol H in Figure 5.9(a). However, even when the best performing channel is used, the detection capability is quite poor, and targets are detected with a good continuity only up to 50Km bistatic range.
- When the polarimetric information is exploited using either the P-GLRT (Figure 5.10(a)) of the Mod-Pol-AR-AMF (Figure 5.10(b)), the improvement is tremendous, confirming that the polarimetric information can be very useful in order to reject the disturbance and enhance the target SNR.

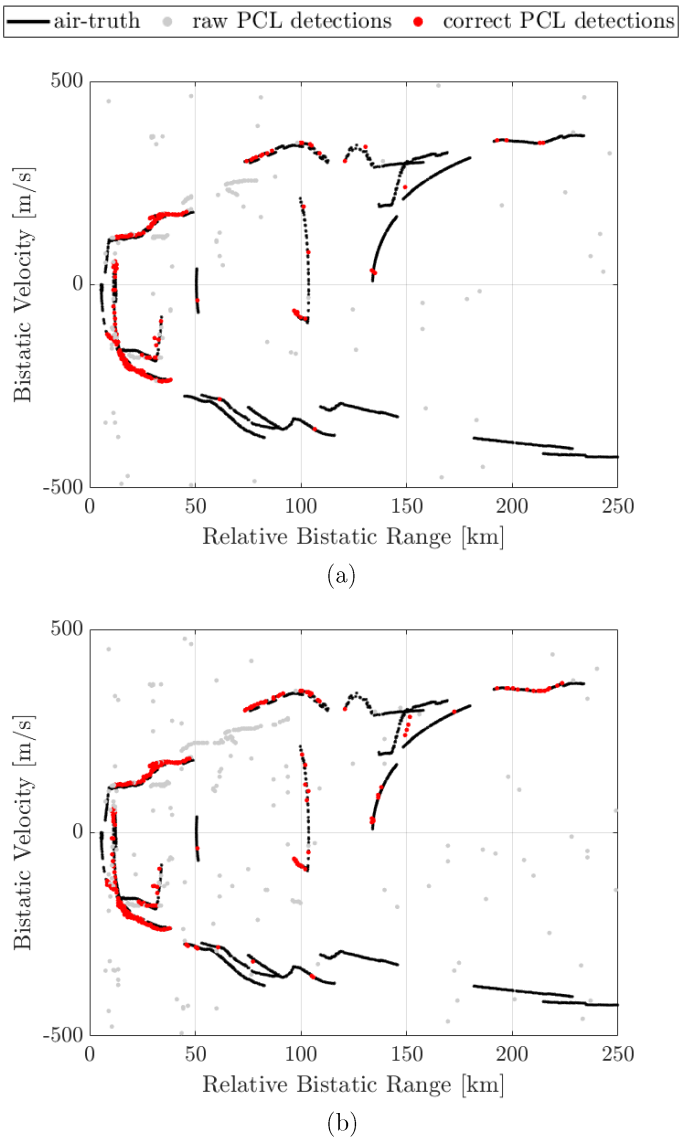

Figure 5.10: Raw PCL detections over 50 consecutive datafiles using:
(a) P-GLRT and (b) Mod-Pol-AR-AMF with $Q = 3$

- When the proposed approach is used (Figure 5.10(b)), a substantial improvement is obtained with respect to the P-GLRT and is evident in almost every track which is now detected with a very good continuity. The advantage is particularly evident on the track included between the 200 and 250 Km and approx. 350 m/s.

Based on these promising results, several tests over the entire data set must be carried out and an extensive analysis would be necessary. Nevertheless, the high computational burden required by the direct implementation of the proposed detector would make the required analysis unsuitable. Therefore, we look for a sub-optimal version of the proposed detector based on some reasonable approximations.

5.3 Sub-optimal Modified Polarimetric AR based AMF

In order to make the proposed detector suitable for a practical application and to strongly reduce the computational load, the two following simplifying assumptions are made

- The phase variation in the Q–dimensional sub-vector $\tilde{\mathbf{t}}(m)$, $m = 0, \ldots, M - Q$ collecting the reference signal samples is assumed negligible.
- The coherent integration operated within the portion of Q samples is neglected.

Note that these two assumptions stand for sufficiently small values of Q. Based on these approximations, the derivation of the sub-optimal version of the proposed detector is straightforward and yields

$$T'' = \frac{2}{\sum_{m=0}^{M-Q} |r_0(m+Q-1)|^2} \times \left[\sum_{m=0}^{M-Q} \tilde{\mathbf{x}}_0^H(m)\, \mathbf{H}^H \widehat{\mathbf{R}}^{-1}\, r_0(m+Q-1-\tau) e^{j2\pi f_d m T} \right] \widehat{\mathbf{D}}_0^{-1} \times \left[\sum_{m=0}^{M-Q} e^{-j2\pi f_d m T} r_0^*(m+Q-1-\tau) \widehat{\mathbf{R}}^{-1} \mathbf{H}\, \tilde{\mathbf{x}}_0(m) \right] \underset{H_0}{\overset{H_1}{\gtrless}} \eta'' \tag{5.2}$$

with T denoting the employed CPI, $r_0(m)$ denoting the m-th sample of the reference signal and η'' denoting the detection threshold.

A sketch of the Sub-optimal Modified Polarimetric AR based AMF is reported in Figure 5.11. Depending on the considered application, the exploited source of opportunity and the employed parameters, one would choose the most convenient application strategy.

Afterwards, the polarimetric whitening stage based on the disturbance covariance matrix $\widehat{\mathbf{D}}_0$ estimated on a set of training data surrounding the CUT. By admitting that the disturbance is locally homogeneous over the range-velocity map, the number of secondary data should be carefully selected by trading the theoretical adaptivity loss with the actual loss due to the inclusion of nonhomogeneous data vectors.

Finally, the detection threshold to be applied after the final NCI is selected according to the *Pfa* expression in (4.14).

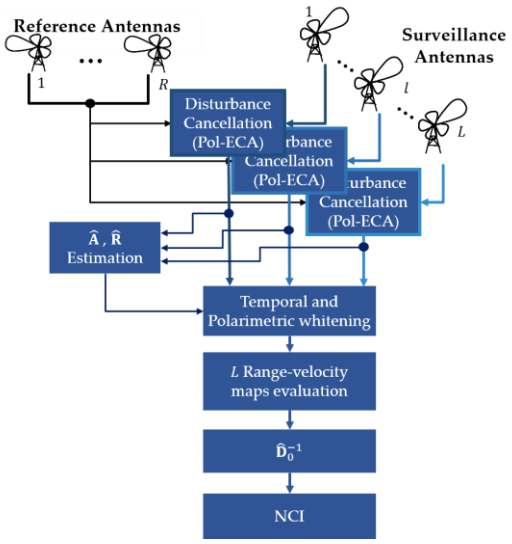

Figure 5.11: Sketch of the Sub-optimal Mod-Pol-AR-AMF for PCL systems

5.3.1 Results

In this Section a preliminary performance assessment of the Sub-optimal Mod-Pol-AR-AMF is performed on the entire available dataset and its effectiveness is demonstrated in comparison with the single-pol solutions, the P-NCI and the P-GLRT.

Based on the availability of real air traffic registrations, an extended detection performance analysis has been carried out by computing the performance statistics over the entire dataset. Specifically, the empirical receiver operating characteristic (ROC) curves have been obtained in order to demonstrate the relative frequency of target detections against the false alarm rate parameterized by the detection threshold applied to the specific detection scheme. With respect to the detection frequency, the analysis has been limited to targets laying in the range band [0; 100] km and included within an angular sector of 90° about the surveillance antenna pointing direction.

In contrast, in order to limit the impact of detections due to strong targets sidelobes and/or to targets not equipped with a transponder, the false alarm density has been recorded in the range band [150; 200] km where the target detection probability is very low so that it is expected not to affect the estimate of the false alarm rate. The results are reported in Figure 5.12 for the four FM radio channels simultaneously collected during the acquisition.

In each sub-figure, we report the detection frequency obtained when the two single polarimetric channels are separately used in dotted green and light blue lines, the result of the P-NCI in dashed black line, the results of the P-GLRT in dash-dot dark blue and finally ones obtained when using the new proposed detection strategy with $Q = 3$ in red.

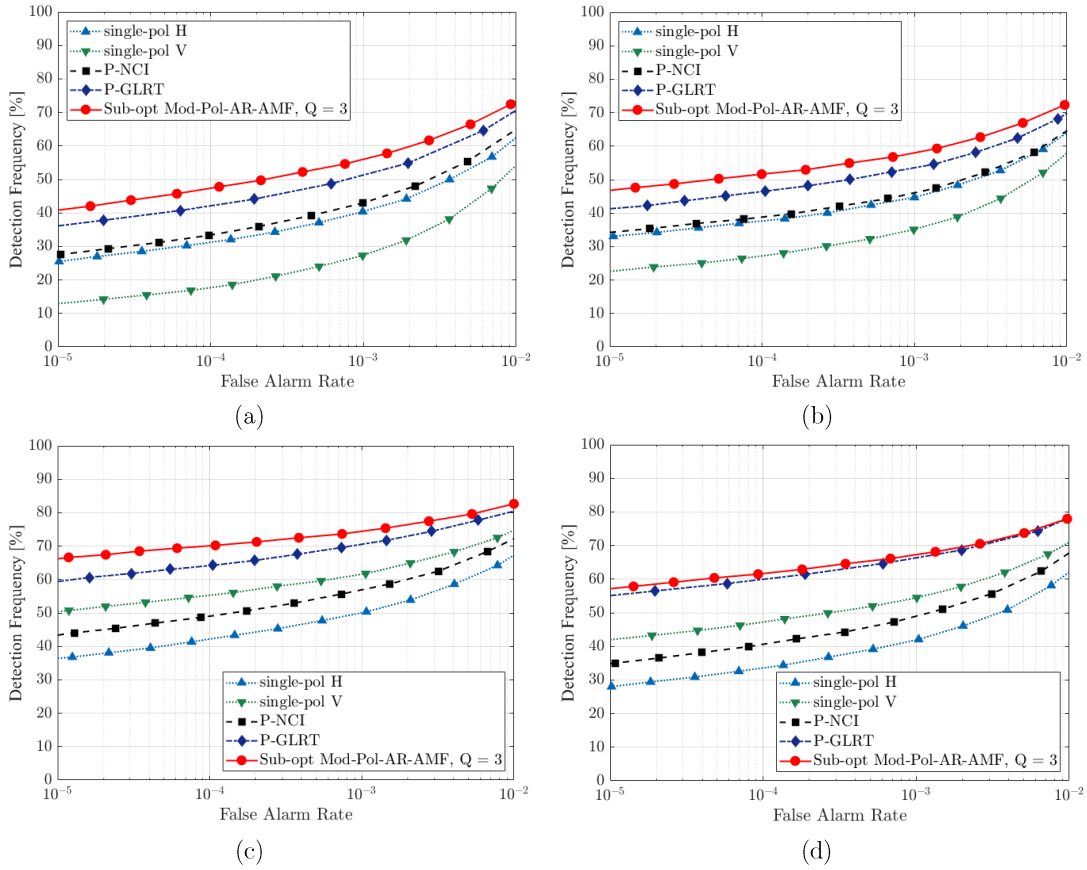

Figure 5.12: Empirical ROC curves for different detection schemes, using:
(a) FMch1 (b) FMch2 (c) FMch3 (d) FMch4

By observing Figure 5.12 the following considerations are in order:

- The signals received at the two single-pol channels and processed according to a conventional single-pol scheme, lead to different results. It is worth noticing that the best performing single-pol channel changes when changing the employed frequency channel; however, it does not depend on the polarization employed by the exploited IO (see Table 5.1 for details on the polarization used in transmission).
- The P-NCI usually yields a very limited detection performance improvement with respect to the single-pol operation. In some cases, due to the generally higher false alarms density, the performance is even degraded with respect to the best performing polarimetric channel, e.g. Figure 5.12(c-d).
- The proposed detection strategy always yields the best detection capability since, for a given false alarm rate, it allows to improve the detection frequency with respect to the other strategies. In all cases, a dramatic improvement is obtained with respect to the worst performing single-pol channel and a substantial enhancement of the detection frequency is obtained with respect to the best performing single-pol channel and the Pol-

NCI. Moreover, the improvement is remarkable with respect to the P-GLRT which was the best performing solution so far. Obviously, the expected performance enhancement depends on the exploited FM channel. For the considered data set, the poorest improvement with respect to the P-GLRT is observed at FMCh4 while the improvement obtained for the other FM channels is comparable.

To better compare the detection results, we report in Table 5.2 the number of correct PCL detections obtained setting the measured $Pfa = 10^{-4}$ for the different detection strategies, namely the single-pol H and V, the P-NCI, the P-GLRT and the Sub-opt Mod-Pol-AR-AMF using different Q values. Note that the maximum number of target occurrences is 9632.

By observing Table 5.2, we confirm the considerations made on Figure 5.12. Additionally, notice that:

(i) the proposed Sub-opt Mod-Pol-AR-AMF always allows the obtain the best detection performance with respect to all the considered strategies for the considered dataset and using the considered Q values. Specifically, the improvement is tremendous with respect to the worst performing single polarimetric channel and remarkable with respect to the other polarimetric detection schemes.

(ii) The detection performance obtained with the proposed strategy changes when changing the employed number of taps Q and the considered FM channel.

(iii) Even when using $Q = 1$, the Sub-opt Mod-Pol-AR-AMF offers a performance improvement with respect to the P-GLRT. More precisely, the number of detections is between 1.6% and 4.3% higher using the proposed strategy, depending on the FM channel. We recall that the whitening stages required by the P-GLRT are always enclosed in the proposed approach. However, the latter also includes additional processing stages aimed at further whitening the data.

(iv) The proposed Sub-opt Mod-Pol-AR-AMF allows obtaining a further improvement when increasing the number of taps from 1 to 3, namely when the whitening stage also exploits the temporal information. For instance, it allows an improvement of 6% with respect to the P-GLRT when using FMch3.

(v) When further increasing the employed Q value, a small loss can be obtained. This might be due to (a) the employed number of secondary data used for the estimation of matrices $\widehat{\mathbf{A}}$ and $\widehat{\mathbf{R}}$, in this example equal to 100 samples, which could no longer be sufficient to provide good estimations and (b) the spectral density of the data which might no longer be well approximated with the employed Q.

Table 5.2
Number of correct detections over the entire dataset, out of 9632 target occurrenciess, with measured $P_{fa} = 10^{-4}$

Detection scheme		FMch1	FMch2	FMch3	FMch4
Single-pol H		3002	3620	4059	3226
Single-pol V		1696	2615	5319	4546
P-NCI		3216	3730	4720	3908
P-GLRT		4030	4473	6181	5752
Sub-opt Mod-Pol-AR-AMF	Q = 1	4217	4737	6593	5913
	Q = 3	4564	4976	6751	5938
	Q = 5	4547	4969	6744	5880
	Q = 10	4420	4816	6621	5791

5.4 Summary

In this Chapter, the effectiveness of the polarimetric adaptive detection strategy proposed in Chapter 3 and Chapter 4 has been investigated against experimental data, collected by an FM radio-based PCL system. Its advantage has been shown also in comparison with other detection strategies, recalled in Chapter 2.

An extensive analysis has been carried out on the entire available set of data files using a sub-optimal version of the proposed strategy, based on reasonable approximations, aimed at reducing the computational load while accepting reduced loss. The extensive analysis has shown that the novel polarimetric model-based adaptive detector is able to improve effectively exploit both the polarimetric and temporal information in order to reject the residual disturbance thus remarkably improving the target detection capability.

Based on the promising results shown in this Chapter, possible future challenges would include the extension of the proposed detection strategy to include additional information diversity sources. For instance, as the authors in [17] have demonstrated, that polarization and frequency diversity could be jointly and fruitfully exploited in order to further improve the detection performance of PCL systems.

This Chapter concludes Part I of this thesis, where the problem of target detection for multi-polarimetic radar systems has been addressed. Once a target has been detected, it is of great interest the possibility to estimate its DoA in order to localize it in the Cartesian plane hence enabling a fully knowledge of the target position. Therefore, Part II of this thesis will be dedicated to addressing this issue.

Part II
Exploitation of frequency and spatial diversity for target localization

Chapter 6
Target DoA estimation exploiting spatial and frequency diversity:
Threshold region performance characterization

This Chapter opens Part II of this two-part thesis, which deals with target DoA estimation for system that jointly exploit signals received at multiple carrier frequencies, as a mean to mitigate the problem of angular ambiguities in arrays employing a limited number of channels. In particular, in this Chapter, the performance characterization of a DoA estimator in the low SNR region is presented. The case of a sensor array simultaneously collecting signals emitted at multiple carrier frequencies by a single source is considered. A ML approach is used as a reference method for DoA estimation and its accuracy is characterized in terms of MSE.

6.1 Background and Motivation

DoA estimation of narrow-band signals is a key problem in sensor array signal with a variety of application fields, such as radar, sonar, mobile communications, etc. The conspicuous interest attracted by this issue is testified by the amount of research literature dedicated to the topic, see e.g. [71] and the references therein. A variety of advanced estimation methods has been proposed and their performances have been extensively studied, see e.g. [33],[79],[89],[91],[93],[107],[108],[117].

However, the majority of studies published over the years addressed the problem of characterizing the performance of DoA estimators under asymptotic assumptions, where asymptotic generally refers to either a high number of samples or high SNR regime [33],[79],[107],[108]. Nevertheless, in many practical applications, such conditions are unlikely to be continuously guaranteed. This is the case of passive location systems, where the object of the location task could be an emitting source [11], [106], [113] or a target that backscatters a signal of opportunity, as in passive radar [50] or passive sonar [85] systems. The passive nature of such systems intrinsically limits the possibility to fully control the performance for any target of interest.

Specifically, the DoA estimation accuracy largely depends on the power level and the transmission rate of either the emitting source, in one-way propagation systems, or the IO, in two-way propagation systems.

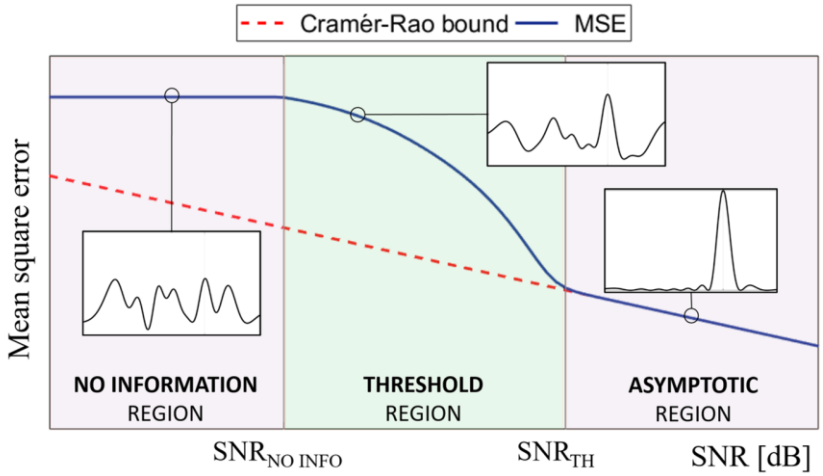

Figure 6.1: Qualitate behavior of the MSE versus the SNR for nonlinear DoA estimation.

These parameters cannot be directly controlled by the system designer. Therefore, it is not unlikely that the aforementioned systems operate in the low SNR regime where accurate angular localization might represent a challenging task. This is especially true when a limited number of receiving sensors is employed in order to limit the system complexity.

As it is well known, at low SNR values, the estimation accuracy of a nonlinear DoA estimator rapidly deviates from its asymptotic performance, experiencing the so-called threshold effect [6],[89]. This effect is qualitatively shown in Figure 6.1, where the MSE is reported versus the SNR: three regions can be identified, referred to as *no information region* (as SNR→0), *threshold region* and *asymptotic region* (as SNR→∞). The Cramér-Rao lower bound (CRB) [33], in dashed red, correctly describes the estimator performance in the asymptotic region, but it is not able to predict the estimator performance for low SNR values. In fact, while the CRB essentially depends on the local errors around the true value, the threshold effect is due to outliers, namely global estimation errors that occur due to an actual estimate outside the mainlobe of the objective function. This issue has been addressed in the open literature by several authors, e.g. [1],[6],[8],[88],[115],[124]. A number of lower bounds has been proposed, accounting for the global errors contribution to the overall MSE, see e.g. the Barankin bound [8], the Bayesian CRB [33],[115], the Ziv-Zakai bound [124].

With reference to the problem under consideration, a very tight bound has been provided in [6], which is able to predict the threshold behaviour of a ML DoA estimator for an array of sensors, receiving narrow-band signals from far-field emitters. It is based on some ideas presented in [89] and [116]. Basically, the MSE is split into two parts, the former coming from local errors obtained when the estimates are close to the true value, and the latter due to outliers. In this work, we elaborate on the achievements in [6] and deal with the case of a

multi frequency (MF) ML DoA estimator that exploits a non-uniform linear array receiving multiple signals simultaneously emitted at different carrier frequencies. Frequency diversity has been considered in sensor array processing with various objectives, using both coherent and non-coherent integration approaches, in several applications. They include, for instance, FDA [119], frequency diversity based MIMO [65],[114], and multi-frequency co-prime arrays [13]. We refer to DoA estimation based on the non-coherent exploitation of signals received at multiple carriers as a mean to mitigate the problem of angular ambiguities in arrays enjoying a limited number of channels. This idea is based on recognizing the change in the array grating lobe pattern that results from the change of frequency and it finds application in several scenarios [101].

Among the most interesting, we mention DoA estimation of single source that transmits signals on multiple carriers, either simultaneously or with rapid frequency hopping. For instance, this is the case of remotely piloted unmanned aerial vehicles (UAV) carrying RF emitting devices. Since the considered multi-carrier sources should not necessarily share the same transmitting antenna, possible scenarios of application also encompass the case of multiple emitters carried by the same platform, e.g. ships or aircrafts [25]. Another very interesting application context is offered by multi-band radar and sonar systems that aim at localizing targets backscattering signals emitted on multiple frequency channels by either one (i.e. mono-/bi-static configuration) or several transmitters (i.e. multistatic configuration). This scenario also embraces the case of PCL systems.

The purpose of this study is to provide a reliable performance characterization of the MF ML estimator in the threshold region. To this end, we exploit the same approach adopted in [6] and use some recent results from the theory of indefinite quadratic forms in Gaussian random variables [4] to evaluate the probability of outlier for the considered estimator. With reference to the source signal, two different models are considered, namely the deterministic and the stochastic, often referred to as conditional model assumption (CMA) and unconditional model assumption (UMA), respectively. The capability to predict jointly the threshold and asymptotic performance of the MF ML DoA estimator via the expressions derived in this study enables a fair comparison between different array configurations without resorting to time-consuming Monte Carlo simulations.

6.2 Signal model and Multi-Carrier ML DoA estimator

Let us consider a K-dimensional linear array, with $K \geq 2$ identical spatial channels, receiving narrowband signals at N different carrier frequencies. This array is employed to estimate the DoA $\boldsymbol{u_0}$ of a multi-frequency source when measurements are severely corrupted by noise. If a single source is present, the complex array output (after down-conversion, filtering and sampling) for the n-th frequency channel can be arranged into the K-dimensional column vector

$$\mathbf{x}_n(t) = \mathrm{A}_n(t)\ \mathbf{s}_\mathrm{n}(u_0) + \mathbf{n}_n(\mathrm{t})$$
$$n = 0, \ldots N-1,\ t = 0, \ldots, M_n - 1 \tag{6.1}$$

where

- $\mathrm{A}_n(t)$, $n = 0, \ldots, N-1$, is the complex baseband source signal. Depending on the application, it can represent the samples of the signal emitted by the source to be localized or the complex amplitude of the target backscattering in response to the signal of opportunity emitted at the l-th frequency channel. We model $\mathrm{A}_n(t)$, $n = 0, \ldots, N-1$, $t = 0, \ldots, M_n - 1$ as unknown parameters and handle them according to the stochastic and the deterministic framework.
- $\mathbf{s}_\mathrm{n}(u_0)$is the target steering vector and accounts for the array response from the target DoA. For a linear array composed by K elements at positions d_k, $k = 0, \ldots, K-1$, measured with respect to a generic phase reference location along the array, it is

$$\mathbf{s}_\mathrm{n}(u_0) = \left[e^{\left(-j\frac{2\pi}{\lambda_n}d_0u_0\right)} \quad \ldots \quad e^{\left(-j\frac{2\pi}{\lambda_n}d_{K-1}u_0\right)}\right]^H \tag{6.2}$$

  Where $u_0 = \sin(\theta_0)$ is the target DoA measured relative to the array boresight and λ_n is the n-th wavelength.
- $\mathbf{n}_n$ is a K-dimensional vector that collects the additive noise samples at the receiving sensors. The noise is assumed to be a spatially white zero-mean complex Gaussian process with unknown mean square value σ^2, independent of the source signal. It is further supposed that the noise contributions at different frequency channels are statistically independent and identically distributed (i.i.d.).
- M_n is the number of space snapshots available for the signal at the n-th carrier frequency and it is assumed known. In the general case, a different number of snapshots might be available for the different frequency channels and their total number is denoted by $Z = \sum_{n=0}^{N-1} M_n$.

Under the above hypotheses, the ML estimate of the DoA u_0 is found by jointly maximizing the likelihood function with respect to $\mathrm{A}_n(t)$, $n = 0, \ldots, N-1$, $t = 0, \ldots, M_n - 1$, and u_0, yielding

$$\hat{u}_0 = \underset{u}{\operatorname{argmax}}\{V(u)\} \tag{6.3}$$

where $u \in [-u_{MAX}, u_{MAX}]$ with $u_{MAX} = 1$ if the non-ambiguous angular sector is $[-\pi, \pi]$ and $V(u)$ is the concentrated ML objective function

$$V(u) = \sum_{n=0}^{N-1} \sum_{t=0}^{M_n-1} \left| \mathbf{s}_n{}^{\mathrm{H}}(u)\, \mathbf{x}_n(t) \right|^2 \tag{6.4}$$

In the absence of noise, this function is proportional to the weighted sum of the estimated array beampattern amplitudes computed at different carrier frequencies, i.e. $b_n(u) = \left| \mathbf{s}_n{}^{\mathrm{H}}(u)\, \mathbf{s}_n(u_0) \right|^2$. This is a direct consequence of the used model for the complex amplitudes $\mathrm{A}_n(t)$ across multiple frequency channels that does not enable the coherent summation of the results obtained at different carrier frequencies.

The asymptotic properties of the ML estimator are well known, whereas its performance in the threshold region has been characterized only in specific cases. In [6] an suitable approximation to the MSE of the ML estimator is provided for a non-uniform linear array exploiting a single carrier frequency case, i.e. for $N = 1$.

The purpose of this work is to extend the analysis of [6] to the multi-carrier ($N > 1$) scenario in order to provide a reliable characterization of the ML estimator performance close to the threshold when multiple frequency channels are employed. We observe that this extension is not straightforward as the exploitation of multiple signals emitted at multiple carriers has a non-trivial impact on the threshold SNR value. In fact, it simultaneously affects (i) the useful signal energy thanks to the increase of the number of snapshots, and (ii) the multi-frequency beampattern characteristics thanks to the diversity conveyed by multiple frequency channels, especially when the corresponding carriers are widely separated.

6.3 Approximation of the MSE and probability of outlier

In this Section, we briefly summarize the approach proposed in [6] to obtain an approximate expression for the MSE of the ML estimator in the threshold region, as it represents the starting point adopted in this work.

The MSE is split into two parts, one coming from small errors obtained when the estimates are close to the true value, and the other due to outliers. The total probability theorem implies that the MSE can be written as

$$\begin{aligned} E[(\hat{u}_0 - u_0)^2] = {} & \Pr\{\text{no outlier}\}\; E[(\hat{u}_0 - u_0)^2 | \text{no outlier}] \\ & + \Pr\{\text{outlier}\}\; E[(\hat{u}_0 - u_0)^2 | \text{outlier}] \end{aligned} \tag{6.5}$$

We recall that the probability of outlier P_0 is the probability of the event that, due to the presence of noise, the global maximum in the likelihood function is outside the mainlobe of the objective function. Close to the threshold region, outliers will tend to concentrate around the sidelobe peaks of the beampattern. Therefore, considering the function in (6.4) at the

sidelobe peaks, V(u_m), $m = 1, \ldots, N_p$ and resorting to the union bound [87] we can approximate P_0 as

$$P_0 \approx \sum_{m=1}^{N_p} P_m = \sum_{m=1}^{N_p} Pr\{V(u_m) > V(u_0)\} \tag{6.6}$$

Notice that the positions u_m of the nominal sidelobe peaks in (6.6) are identified based on the theoretical (noise-free) MF beampattern corresponding to (6.4). This is written as

$$V_{theo}(u) = \sigma^2 \sum_{n=0}^{N-1} M_n \, \mathrm{SNR}_n \, b_n(u) \tag{6.7}$$

where SNR_n is the SNR available at the single antenna element, for the single snapshot received at the n-th frequency channel, and its explicit expression will be provided in the subsequent Sections with reference to each adopted signal model. The numbering of the sidelobe peaks positions is defined so that u_0 is the position of the mainlobe peak and u_m, $m = 1, \ldots, N_p$, are the positions of the N_p sidelobe peaks of the resulting MF beampattern. The individual probabilities P_m will be referred to as the pairwise error probabilities, borrowing this terminology from communication theory [87].

Exploiting (6.6), the MSE approximation for the considered ML estimator is written as

$$E[(\hat{u}_0 - u_0)^2] \approx \left[1 - \sum_{m=1}^{N_p} P_m\right] \cdot \mathrm{CRB} + \sum_{m=1}^{N_p} P_m \, (u_m - u_0)^2 \tag{6.8}$$

where the CRB is used as a good predictor of the small errors of the MSE in the asymptotic region. Notice that this approximate expression is quite general and applies also to the case under consideration since the number N of frequency channels, the corresponding wavelengths, and the number M_n of snapshots available at the l-th carrier frequency will largely affect the pairwise error probabilities, the position of sidelobe peaks, and the CRB.

A closed form expression for the pairwise error probabilities P_m, $m = 1, \ldots, N_p$, has been derived in [6] for the case $N = 1$, and two different signal models, namely the deterministic (or conditional) and the stochastic (or unconditional).
In the former case, the amplitudes A(t), $t = 0, \ldots, M - 1$, are assumed to be deterministic (but unknown) complex values whereas in the latter situation, the signal is assumed to be a stationary, temporally white, zero-mean, complex Gaussian process. The derived expressions are reported here for ease of reference.

A. Deterministic Signal Model (or Conditional Model Assumption)

$$
\begin{aligned}
P_m = Q\left(\sqrt{\frac{S}{2}\left(1-\sqrt{1-|g_m|^2}\right)}, \sqrt{\frac{S}{2}\left(1+\sqrt{1-|g_m|^2}\right)}\right) \\
- e^{-\frac{S}{2}}\left\{ I_0\left(\frac{|g_m|S}{2}\right) - \frac{1}{2^{2M-1}} I_0\left(\frac{|g_m|S}{2}\right)\sum_{p=0}^{M-1}\binom{2M-1}{p}\right. \\
\left. - \frac{1}{2^{2M-1}}\sum_{p=1}^{M-1} I_p\left(\frac{|g_m|S}{2}\right)\right. \\
\left. \times\left[\left(\frac{1+\sqrt{1-|g_m|^2}}{|g_m|}\right)^l - \left(\frac{1-\sqrt{1-|g_m|^2}}{|g_m|}\right)^l\right]\sum_{k=0}^{M-1-p}\binom{2M-1}{k}\right\}
\end{aligned}
\tag{6.9}
$$

where

$$
Q(\alpha,\beta) = \int_{\beta}^{\infty} te^{-\frac{(t^2+\alpha^2)}{2}} I_0(\alpha t)\, dt \tag{6.10}
$$

is the Marcum Q-function, $I_p(\cdot)$ is the modified Bessel function of the first kind and order p, $g_m = \mathbf{s}^H(u_0)\mathbf{s}(u_0)/K$, and $\mathrm{S} \triangleq \frac{K}{\sigma^2}\sum_{t=0}^{M-1}|A(t)|^2$ may be interpreted as the total SNR integrated over the K antennas and the M snapshots.

B. Stochastic Signal Model (or Unconditional Model Assumption)

$$
P_m = \frac{1}{(1+q_m)^{2M-1}}\sum_{t=0}^{M-1}\binom{2M-1}{t} q_m^t \tag{6.11}
$$

where

$$
q_m = \left[\frac{1+\sqrt{1+\dfrac{4\sigma^2(\sigma^2+\sigma_s^2K)}{\sigma_s^4K^2(1-|g_m|^2)}}}{-1+\sqrt{1+\dfrac{4\sigma^2(\sigma^2+\sigma_s^2K)}{\sigma_s^4K^2(1-|g_m|^2)}}}\right] \tag{6.12}
$$

where $\sigma_s^2 = \mathrm{E}\{|A(t)|^2\}$ is the signal power.

The expressions in (6.9) and (6.11) are no longer valid if $N > 1$. They will be generalized for the multi-carrier case in the next two Sections both for the deterministic and the stochastic signals model.

6.4 Evaluation of the Pairwise Error Probabilities under CMA

6.4.1 Theoretical Derivation

In this Section, we derive the expression for the pairwise error probabilities under deterministic signal model, or Conditional Model Assumption.

The pairwise error probability in (6.6) can be written as

$$P_m = \Pr\{[V(u_m) > V(u_0)]\} = \Pr\{[V < 0]\} = \int_{-\infty}^{0} p_V(V)\,\mathrm{d}V \tag{6.13}$$

Being $p_V(V)$ the pdf of the random variable $\mathrm{V} = \mathrm{V}(u_0) - \mathrm{V}(u_m)$.

As it is apparent from (6.13), we need to evaluate the cumulative distribution function (CDF) of V in 0, i.e. $F_V(0)$. To this end, V can be rewritten as

$$V = V(u_0) - V(u_m) = \sum_{n=0}^{N-1} \sum_{t=0}^{M_n-1} |\, \mathbf{x}_n^H(t) \mathbf{P}_n\, \mathbf{x}_n(t)|^2 \tag{6.14}$$

where

$$\begin{gathered} \mathbf{P}_n = \mathbf{s}_n(u_0)\mathbf{s}_n{}^H(u_0) - \mathbf{s}_n(u_m)\mathbf{s}_n{}^H(u_m) \\ (n = 0, \ldots, N\text{-}1) \end{gathered} \tag{6.15}$$

is a rank-2 $K \times K$ Hermitian matrix.

By arranging the available snapshots in the $KZ \times 1$ vector $\mathbf{x} = \frac{1}{\sigma_n}[\mathbf{x}_0^H(0) \cdots \mathbf{x}_0^H(M_0 - 1)\ \mathbf{x}_1^H(0) \cdots \mathbf{x}_{N-1}^H(M_{N-1} - 1)]^H$ and by defining the corresponding $KZ \times KZ$ block diagonal matrix

$\mathbf{P} = \sigma^2 \begin{bmatrix} \boldsymbol{I}_{M_0} \otimes \mathbf{P}_0 & \cdots & \mathbf{0} \\ \vdots & \ddots & \vdots \\ \mathbf{0} & \cdots & \boldsymbol{I}_{M_{N-1}} \otimes \mathbf{P}_{N-1} \end{bmatrix}$, we can further simplify (6.14) as

$$V = \mathbf{x}^H \mathbf{P} \mathbf{x} \tag{6.16}$$

By definition, the rank of $\mathbf{P}$ is equal to $2Z$. Specifically, it exhibits at most N pairs of

distinct non-zero eigenvalues of equal magnitude but opposite sign. In the following, we assume that there are exactly N pairs of distinct eigenvalues, each with multiplicity M_n, $n = 0, \ldots, N-1$. In other words, we suppose that different carrier frequencies selected from the considered set yield distinct pairs of eigenvalues. Notice that this hypothesis is mild and easily verified in practical cases. In fact, one can easily evaluate the non-zero eigenvalues of $\mathbf{P}$ by using Theorem 18.1.1 in [45], thus obtaining

$$\begin{gathered}\gamma_n = K\sigma^2\sqrt{1-\left|g_{m,n}\right|^2} \\ \gamma_{n+N} = -K\sigma^2\sqrt{1-\left|g_{m,n}\right|^2} \\ (n = 0, \ldots, N-1)\end{gathered} \tag{6.17}$$

where $g_{m,n} = \mathbf{s}_n{}^H(u_0)\mathbf{s}_n(u_m)/K$ and we set $M_n = M_{n+N}$.

Let $\mathbf{P} = \mathbf{Q}\boldsymbol{\Lambda}\mathbf{Q}^H$ denote the eigenvalue decomposition of $\mathbf{P}$, we can assume that $\boldsymbol{\Lambda}$ is organized so that $\boldsymbol{\Lambda} = \begin{bmatrix} \bar{\boldsymbol{\Lambda}} & \mathbf{0}_{2Z\times(KZ-2Z)} \\ \mathbf{0}_{(KZ-2Z)\times 2Z} & \mathbf{0}_{(KZ-2Z)\times(KZ-2Z)} \end{bmatrix}$, where $\bar{\boldsymbol{\Lambda}}$ is a 2Z×2Z block with the non-zero eigenvalues on its main diagonal.

Equation (6.16) can be reworked as

$$V = (\mathbf{Q}^H\mathbf{x})^H\boldsymbol{\Lambda}\mathbf{Q}^H\mathbf{x} = \bar{\mathbf{x}}^H\bar{\boldsymbol{\Lambda}}\,\bar{\mathbf{x}} \tag{6.18}$$

where $\bar{\mathbf{x}} = \mathbf{S}^H(\mathbf{Q}^H\mathbf{x})$, $\mathbf{S} = \left[\mathbf{I}_{2Z} \;\vdots\; \mathbf{0}_{2Z\times(KZ-2Z)}\right]^H$.

Under the deterministic signal model, or CMA, $\mathbf{x}$ is a complex Gaussian random vector, i.e. $\mathbf{x} \sim \mathcal{CN}(\mathbf{q},\mathbf{I}_{KZ})$ with mean vector

$$\mathbf{q} = \frac{1}{\sigma}[A_0^*(0)\mathbf{s}_0^H(u_0) \ldots A_{N-1}^*(M_{N-1}-1)\mathbf{s}_{N-1}^H(u_0)]^H \tag{6.19}$$

Consequently, $\bar{\mathbf{x}} \sim \mathcal{CN}(\bar{\mathbf{q}}, \mathbf{I}_{2Z})$, with $\bar{\mathbf{q}} = \mathbf{S}^H(\mathbf{Q}^H\mathbf{q})$, and (6.19) is usefully rewritten as

$$V = \left(\bar{\mathbf{h}} + \bar{\mathbf{q}}\right)^H\bar{\boldsymbol{\Lambda}}\left(\bar{\mathbf{h}} + \bar{\mathbf{q}}\right) \tag{6.20}$$

where $\bar{\mathbf{h}}$ is a white zero-mean circularly symmetric complex Gaussian vector, i.e. $\bar{\mathbf{h}} \sim \mathcal{CN}(\mathbf{0}, \mathbf{I}_{2Z})$.

Using the expression in (6.20) for the variable V, we can now exploit the approach in [4] to derive an approximation of the sought pairwise error probability. Specifically, the CDF of V can be written as

$$F_V(y) = \int_{-\infty}^{\infty} p(\bar{\mathbf{h}})\, \mathrm{u}\big(y - (\bar{\mathbf{h}} + \bar{\mathbf{q}})^H\ \bar{\mathbf{\Lambda}}\,(\bar{\mathbf{h}} + \bar{\mathbf{q}})\big) d\bar{\mathbf{h}} \tag{6.21}$$

where $p(\bar{\mathbf{h}})$ is the pdf of $\bar{\mathbf{h}}$ and $\mathrm{u}(x)$ is the unit step function. Resorting to the Fourier transform representation or the unit step function

$$\mathrm{u}(x) = \frac{1}{2\pi}\int_{-\infty}^{\infty} \frac{e^{x(j\omega+\beta)}}{j\omega+\beta}\, d\omega \quad \text{for any } \beta > 0 \tag{6.22}$$

one can write $F_V(y)$ as

$$F_V(y) = \frac{1}{2\pi^{2Z+1}} \iint_{-\infty}^{\infty} e^{-\left(\|\bar{\mathbf{h}}\|^2 + (\bar{\mathbf{h}}+\bar{\mathbf{q}})^H (j\omega+\beta)\, \bar{\mathbf{\Lambda}}\, (\bar{\mathbf{h}}+\bar{\mathbf{q}})\right)} d\bar{\mathbf{h}}\, \frac{e^{y(j\omega+\beta)}}{j\omega+\beta}\, d\omega \tag{6.23}$$

that, solving the inner integral, yields

$$P_m = F_V(0) = \frac{1}{2\pi} \int_{-\infty}^{\infty} \frac{\exp\left\{-\bar{\mathbf{q}}^H \left[\mathbf{I}_{2Z} + \frac{1}{(j\omega+\beta)}\bar{\mathbf{\Lambda}}^{-1}\right]^{-1} \bar{\mathbf{q}}\right\}}{|\mathbf{I}_{2Z} + (j\omega+\beta)\bar{\mathbf{\Lambda}}|\ (j\omega+\beta)}\, d\omega \tag{6.24}$$

A closed form solution for the 1D integral in (6.24) cannot be obtained [100]. Therefore, as in [4], we resort to the saddle point (SP) technique [10], which is a well-known method for approximating integrals. To this end, we write (6.24) as

$$F_V(0) = \frac{1}{2\pi}\int_{-\infty}^{\infty} e^{f(\omega)}\, d\omega \tag{6.25}$$

with

$$\begin{aligned} f(\omega) = &-\ln(j\omega+\beta) - \sum_{k=0}^{2N-1} M_k \ln[1 + (j\omega+\beta)\gamma_k] \\ &- \sum_{k=0}^{2N-1} S_k \left[1 - \frac{1}{1 + (j\omega+\beta)\gamma_k}\right] \end{aligned} \tag{6.26}$$

where $S_k = \sum_{j\in I(k)} |\bar{q}_j|^2$, and $I(k)$ containing the indices of the vector $\bar{\mathbf{q}}$ entries corresponding to the k-th eigenvalue ($|I(k)|$=M_k).

To apply the SP technique, we approximate $f(\omega)$ using a second order Taylor expansion around ω_0 , where $\omega_0 = j(\beta + p_0)$ is the solution of

$$f'(\omega) = -\sum_{k=0}^{2N-1} S_k \left[\frac{j\gamma_k}{(1 + (j\omega + \beta)\gamma_k)^2}\right] - \frac{\mathrm{j}}{(j\omega + \beta)} - \sum_{k=0}^{2N-1} M_k \left[\frac{j\gamma_k}{1 + (j\omega + \beta)\gamma_k}\right] \tag{6.27}$$

with $p_0 \in (-\mu_{MAX}, 0)$, and $\mu_{MAX} = 1/\gamma_{MAX}$, being $\gamma_{MAX} = \max\{\gamma_k,\ k = 0, \ldots, N-1\}$
Consequently, the integral in (6.25) can be approximated as

$$F_V(0) \approx \frac{1}{2\pi} e^{f(\omega_0)} \sqrt{\frac{2\pi}{|f''(\omega_0)|}} \tag{6.28}$$

By writing $f(\omega_0)$ and $f''(\omega_0)$, after some standard algebra, we eventually obtain

$$P_m = F_V(0) \approx \frac{|p_0|}{\sqrt{2\pi}} \exp\left\{-\sum_{k=0}^{2N-1} M_k \ln(1 - \gamma_k p_0) - \frac{S_k \gamma_k p_0}{1 - \gamma_k p_0}\right\} \times \left|-\frac{1}{{p_0}^2} - \sum_{k=0}^{2N-1} \frac{\gamma_k^2 M_k}{(1 - \gamma_k p_0)^2} + \frac{2\gamma_k^2 S_k}{(1 - \gamma_k p_0)^3}\right|^{-1/2} \tag{6.29}$$

6.4.2 Simulation Results

We first verify the accuracy of the approximation in (6.29), by comparing it with its exact expression when available (i.e. for $N = 1$ see (6.9)).

In Figure 6.2(a) we report the normalized theoretical MF beampattern $\mathrm{V}_{\mathrm{theo}}(u)$ in (6.7) for a three-element array with element position $d = [0 \ \ 2 \ \ 6.8]\lambda_1$, where λ_1 is the wavelength of the exploited frequency channel and the DoA of the signal source is $u_0 = 0$. As it is apparent, a quite challenging array layout has been considered that is likely to yield outlier DoA estimates being the number of elements quite small and their spacing well above the employed wavelength. Consequently, a generally high sidelobe level is observed.
The most relevant sidelobe leading to outliers when the SNR decreases is indeed the highest sidelobe (indicated by the red arrow in Figure 6.2(a). It represents the selected sidelobe where the pairwise error probability P_m is evaluated in Figure 6.2(b) for different SNR values, versus

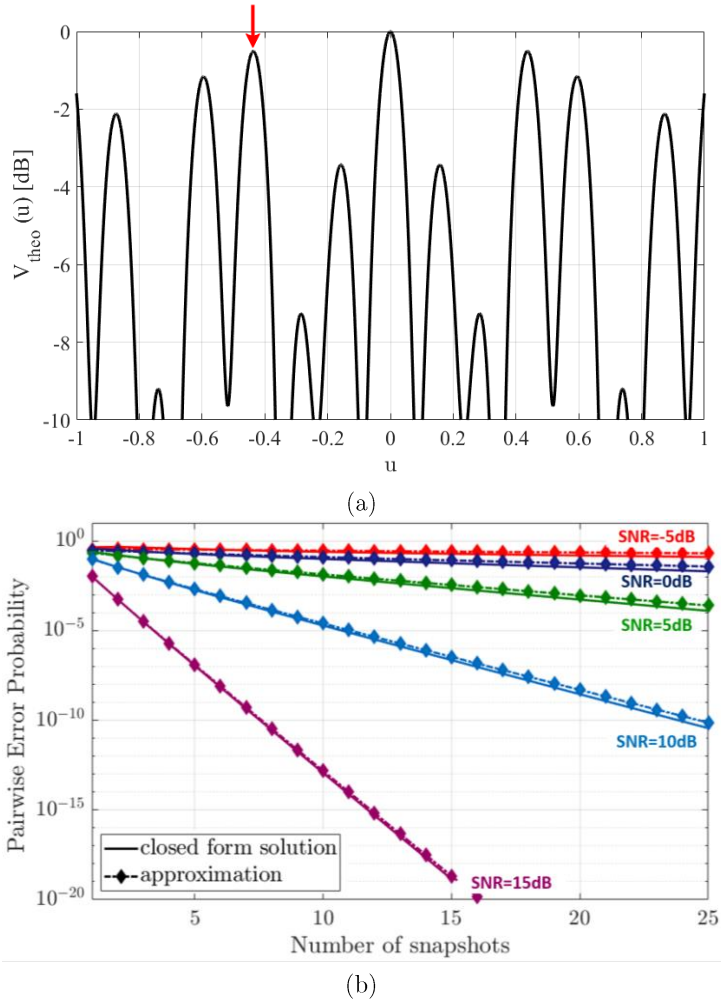

Figure 6.2: Results for $N = 1$ and $K = 3$ ($d = [0 \;\; 2 \;\; 6.8]\,\lambda_1$) : (a) Theoretical MF beampattern (b) Pairwise error probability for a selected sidelobe for different SNR versus M.

the number M of snapshots collected. Specifically, we refer to the SNR at the single antenna element, for the single snapshot, i.e. SNR $\triangleq \frac{1}{\sigma^2 M}\sum_{t=0}^{M-1}|A(t)|^2$.

Figure 6.2(b) shows that the P_m expression derived in (6.29) is able to approximate the pairwise error probability in (6.9), even for very low values, e.g. $P_m = 10^{-20}$.

In Figure 6.3 we compare the normalized theoretical MF beampattern $\mathrm{V}_{\mathrm{theo}}(u)$ of Figure 6.2(a) with that obtained exploiting three different frequency channels ($N = 3$) with wavelengths λ_1, $\lambda_2 = 0.76\,\lambda_1$, and $\lambda_3 = 0.57\,\lambda_1$, respectively. It is expected that the asymptotic DoA estimation accuracy could benefit from the joint exploitation of signals with higher carrier frequencies.

However, we observe that the additional frequency channels considered in this case study are more critical in term of outliers when separately employed with the same array of Figure 6.2. Nevertheless, Figure 6.3 shows that the sidelobe level is fruitfully reduced if the frequency

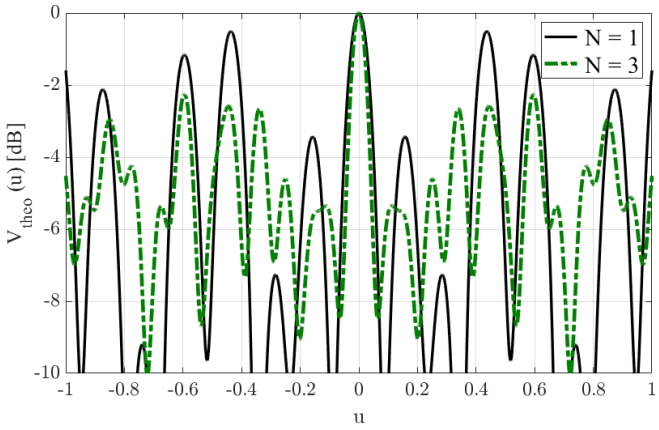

Figure 6.3: Theoretical MF beampattern $V_{theo}(u)$ for three-element array $d = [0 \;\; 2 \;\; 6.8]\,\lambda_1$ exploiting one or three frequency channels

diversity is exploited. Accordingly, we expect the probability of outlier to be lower since a higher noise level would be required for the sidelobes to exceed the main lobe peak.
Clearly, the lower the probability of outlier, the higher the number of MC simulation trials necessary to estimate such a rare event, i.e. the availability of a closed-form reliable expression to predict the estimator performance becomes more and more relevant.

To check the accuracy of the union bound approximation for the probability of outlier, MC simulations have been performed for different configurations. In all cases, the number of MC trials was 10^6, whereas this number was increased to $5{\cdot}10^7$ when the probability of outlier P_0 was expected to be below 10^{-4}. The outcome of the DoA estimation stage is labelled as *outlier* if it falls outside the mainlobe of the theoretical MF beampattern $V_{theo}(u)$. Each outlier is associated with the closest sidelobe peak, according to a minimum distance criterion.

We compare the results of the MC simulations with the probability of outlier evaluated as in (6.6) by using the result in (6.29) at each sidelobe peak. Although the positions of these peaks are usually not available in closed form, they can be readily calculated by some numerical methods.

In Figure 6.4, the probability of outlier P_0 is compared with the results of MC simulations (dots) for different SNR. The SNR_n at the n-th frequency channel is defined as $SNR_n \triangleq \frac{1}{\sigma^2 M_n}\sum_{t=0}^{M_n-1}|A_n(t)|^2$, where the same SNR level is assumed for the employed frequency channels. The results are reported for the case studies in Table 6.1. For cases A and B also the P_0 obtained with the exact expression in (6.9) is reported, in solid black line, for comparison.

Observing Figure 6.4 the following considerations are in order:

- the expression in (6.29) effectively approximates the closed form solution, when available.
- The union bound approximation is quite robust for high SNR whereas it overestimates the probability of outlier at very low SNR values, where the simplified hypotheses behind

(6.6) are no longer verified. However, this is not expected to be an issue since those values are likely to correspond to the no information region.

- As expected, the higher the total number Z of snapshots (collected either in time or in frequency domains) the better the performance.
- Keeping constant the total number of snapshots, better results can be obtained if they are collected at different frequency channels (compare the green and light blue lines), revealing that the frequency diversity is essential besides the expected increase in integrated SNR. Basically, case B yields a gain of approximately 5 dB for P_0 values below 10^{-2} whereas case C provides an additional gain of 7 dB.
- The last consideration is confirmed comparing case B and case E (see the green and magenta lines). In fact, even if two out of three frequency channels provide a lower SNR, their exploitation still allows to significantly reduce the probability of outlier with respect to the situation using $M = 3$ snapshots from the frequency channel with the highest SNR. This is due to the improvement arising in term of sidelobes level in the resulting multi-frequency likelihood function.
- When exploiting three snapshots from three frequency channels, the improvement is significant with respect to $Z = 1$, since case D benefits from both the resulting SNR integration and conveyed by the MF approach.

Table 6.1
Case studies A-E

	case A	case B	case C	case D	case E
Number of array elements K	3	3	3	3	3
Number of carriers N	1	1	3	3	3
Number of snapshots M	1	3	1	3	1
Array layout	$d = [0\ \ 2\ \ 6.8]\,\lambda_1$				
Wavelengths	λ_1	λ_1	$\lambda_1,\ \lambda_2 = 0.76\,\lambda_1,\ \ \lambda_3 = 0.57\,\lambda_1$		
SNR	–	–	$\mathrm{SNR}_1 = \mathrm{SNR}_2 = \mathrm{SNR}_3$		$\mathrm{SNR}_2 = \mathrm{SNR}_3 = \mathrm{SNR}_1 - 3\mathrm{dB}$

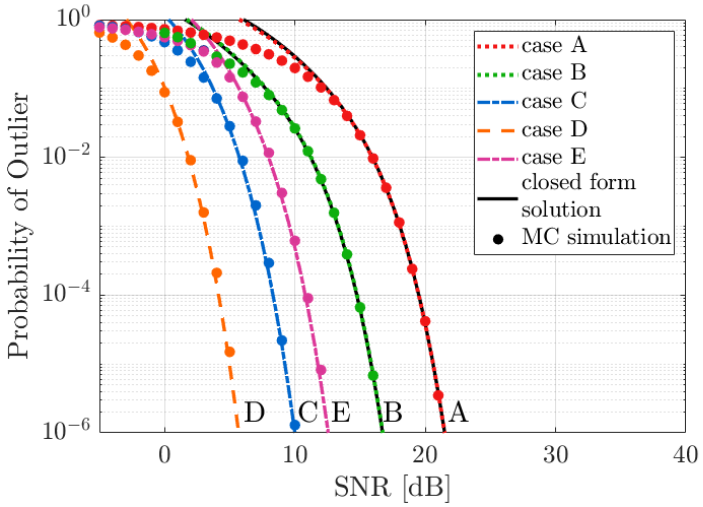

Figure 6.4: Probability of outlier under CMA for a three-element array $d = [0 \;\; 2 \;\; 6.8]\,\lambda_1$ for different case studies, reported in Table 6.1.

6.5 Evaluation of the Pairwise Error Probabilities under UMA

6.5.1 Theoretical Derivation

In this Section, we derive the expression for the pairwise error probabilities under stochastic signal model, or UMA. By proceeding as in Section 6.4.1, we obtain the same expression as in (6.18). However, under UMA, vector $\mathbf{x}$ is a set of statistically independent K-dimensional complex Gaussian random variables, with zero-mean vector and covariance matrix $\mathbf{R}$, i.e. $\mathbf{x} \sim \mathcal{CN}(\mathbf{0},\mathbf{R})$ where $\mathbf{R} = \begin{bmatrix} \mathbf{I}_{M_0} \otimes \mathbf{R}_0 & \cdots & \mathbf{0} \\ \vdots & \ddots & \vdots \\ \mathbf{0} & \cdots & \mathbf{I}_{M_{N-1}} \otimes \mathbf{R}_{N-1} \end{bmatrix}$ and the $K \times K$ blocks on the main diagonal are given by $\mathbf{R}_n = \frac{\sigma_{s,n}^2}{\sigma^2}\mathbf{s}_n(u_0)\mathbf{s}_n(u_0)^H + \mathbf{I}_K$, $n = 0, \ldots, N-1$, with $\sigma_{s,n}^2 = \mathrm{E}\{|A_n(t)|^2\}$ being the power of the n-th signal. Thus, V in (6.18) is a complex central quadratic form.

Without loss of generality, we can consider the central quadratic form in the variable $\mathbf{x}_w$ which is the whitened version of $\mathbf{x}$

$$\begin{aligned} \mathbf{x}_w &= \left(\mathbf{R}^{-1/2}\right)^H \mathbf{x} \\ \mathbf{P}_w &= \left(\mathbf{R}^{1/2}\right)^H \mathbf{x} \left(\mathbf{R}^{1/2}\right) \end{aligned} \tag{6.30}$$

The rank of matrix $\mathbf{P}_w$ is equal to $2Z$ and it has at most N pairs of distinct non-zero

eigenvalues. As in Section 6.4.1, we suppose that there are exactly N pairs of distinct eigenvalues, each with multiplicity M_n , $n = 0, \ldots, N-1$ given by

$$\begin{aligned}\gamma_n &= -\frac{K^2\sigma_{s,n}^2\left(1-\left|g_{m,n}\right|^2\right)}{2}\left[-1-\sqrt{1+\frac{4\sigma^2\left(\sigma^2+\sigma_{s,n}^2K\right)}{\sigma_{s,n}^4K^2\left(1-\left|g_{m,n}\right|^2\right)}}\right]\\ \gamma_{n+N} &= -\frac{K^2\sigma_{s,n}^2\left(1-\left|g_{m,n}\right|^2\right)}{2}\left[-1+\sqrt{1+\frac{4\sigma^2\left(\sigma^2+\sigma_{s,n}^2K\right)}{\sigma_{s,n}^4K^2\left(1-\left|g_{m,n}\right|^2\right)}}\right]\end{aligned} \tag{6.31}$$

Denoting by $\mathbf{P}_{\mathrm{w}} = \mathbf{Q}_w\mathbf{\Lambda}_w\mathbf{Q}_w^H$ the eigenvalue decomposition of $\mathbf{P}_{\mathrm{w}}$, we can assume that $\mathbf{\Lambda}_w$ is organized so that $\mathbf{\Lambda}_w = \begin{bmatrix}\overline{\mathbf{\Lambda}}_w & \mathbf{0}_{2Z\times(KZ-2Z)}\\ \mathbf{0}_{(KZ-2Z)\times 2Z} & \mathbf{0}_{(KZ-2Z)\times(KZ-2Z)}\end{bmatrix}$ where $\overline{\mathbf{\Lambda}}_w$ is a $2Z\times 2Z$ diagonal matrix containing the non-zero eigenvalues on its main diagonal.

Therefore, under UMA, the CDF of V can be written as

$$F_V(y) = \frac{1}{2\pi}\int_{-\infty}^{\infty}\frac{e^{y(j\omega+\beta)}}{\left|\mathbf{I}_{2Z}+(j\omega+\beta)\overline{\mathbf{\Lambda}}_w\right|\ (j\omega+\beta)}d\omega \tag{6.32}$$

The integral in (6.32) has a closed form solution that can be derived as in [4]. First, resorting to the partial fraction expansion, we can write

$$\frac{1}{\left|\mathbf{I}_{2Z}+(j\omega+\beta)\overline{\mathbf{\Lambda}}_w\right|\ (j\omega+\beta)} = \sum_{k=0}^{2N-1}\sum_{t=0}^{M_k-1}\frac{\alpha_{k,t}}{[1/\gamma_k+(j\omega+\beta)]^{t+1}} + \frac{1}{(j\omega+\beta)} \tag{6.33}$$

where the coefficients $\alpha_{k,t}$ are given by

$$\alpha_{k,t} = \frac{1}{\Gamma(M_k-t)}\left[\prod_{j=.0}^{2N-1}\mu_j^{M_j}\right]y_k^{(M_k-t-1)}(s)\Big|_{s=-\mu_k} \tag{6.34}$$

$$k = 0, \ldots, 2N-1,\ t = 0, \ldots, \mathrm{M}_k - 1$$

with $y_k^{(M_k-t-1)}(s)$ the (M_k – t – 1)-th derivative of $y_k(s)$, defined as

$$y_k(s) = \prod_{\substack{j=0 \\ j\neq k}}^{2N-1} (\mu_j + s)^{-M_j} \tag{6.35}$$

with $\mu_j = {}^{1}/_{\gamma_j}$, $j = 0, \ldots, 2N-1$, $\mu_{2N} = 0$ and $M_{2N} = 1$.

Now, using the expression in (6.33), we can split the integral in (6.32) in two parts and evaluate them separately. Eventually, after some calculations, we obtain a closed form solution

$$P_m = F_V(0) = \frac{1}{2}\left[1 + \sum_{k=0}^{2N-1} \text{sign}(\gamma_k) \cdot \alpha_{k,0}\right] \tag{6.36}$$

One can evaluate the coefficient $y_k^{(M_n-1)}$ in $\alpha_{k,0}$ differentiating the logarithm of $y_k(s)$, i.e. $\frac{d}{ds}\log\big(y_k(s)\big) = \frac{1}{y_k(s)} y_k^{(1)}(s)$, that yields

$$y_k^{(1)}(s) = -y_k(s) \sum_{\substack{j=0 \\ j\neq k}}^{2N} M_j (\mu_j + s)^{-1} \tag{6.37}$$

Subsequently, Leibniz's rule for differentiation of products may be applied. Thus, the required coefficients can be evaluated using the following recursion formula

$$\begin{aligned} y_k^{(p)}(s)\Big|_{s=-\mu_k} &= \frac{d^{p-1}}{ds^{p-1}} y_k^{(1)}(s)\Big|_{s=-\mu_k} \\ &= \sum_{u=0}^{p-1} \sum_{\substack{j=0 \\ j\neq k}}^{2N} M_j \binom{p-1}{u} \frac{(-1)^{p-u}\Gamma(p-u)}{(\mu_j - \mu_k)^{p-u}} y_k^{(r)}(s)\Big|_{s=-\mu_k} \qquad (p \geq 1) \end{aligned} \tag{6.38}$$

$$y_k^{(0)}(s)\Big|_{s=-\mu_k} = \; y_k(-\mu_k) = \prod_{\substack{j=0 \\ j\neq k}}^{2N} (\mu_j - \mu_k)^{-M_j}$$

Equation (6.36), with coefficients obtained using (6.34) and (6.38), provides a closed form expression of the pairwise error probability under UMA for the m-th sidelobe peak.

In particular, for the SF case, namely when $N = 1$ and $M \geq 1$, it coincides with the solution in (6.11), being $q_m = \left|\frac{\gamma_0}{\gamma_1}\right|$ the ratio between the absolute values of the two eigenvalues.

In the dual special case, namely when $M = 1$ and $N \geq 1$, with the assumptions made on the

distinct eigenvalues, we have $M_k = 1$, $k = 0, \ldots, 2N$. Consequently, we can write the residues $\alpha_{k,0}$ as

$$\alpha_{k,0} = \frac{\prod_{j=0}^{2N-1} \mu_j}{\prod_{\substack{j=0 \\ j \neq k}}^{2N} (\mu_j - \mu_k)} \tag{6.39}$$

6.5.2 Simulation Results

To verify the accuracy of the expression in (6.36), Figure 6.5 compares the results of MC simulations with the probability of outlier evaluated using (6.6) and P_m obtained from (6.36) under stochastic signal model. The results are reported versus SNR, being in this case $\text{SNR}_n \triangleq \frac{\sigma_{s,n}^2}{\sigma^2}$. The same methodology is adopted as in Section 6.4.2, and the same three-element array layout $d = [0\ 2\ 6.8]\ \lambda_1$ is employed together with some representative case studies, namely those B,C and D.

Observing Figure 6.5, some of the considerations made on Figure 6.4 under CMA can be confirmed also under UMA. In addition, we notice that:

- when very few snapshots are available (collected either in time or in frequency), the union bound approximation slightly overestimates the probability of outlier also for high SNR values (see cases B and C); similar results were obtained also in [6] for the single-carrier case.
- Increasing the number of snapshots, the union bound approximation seems quite robust for high SNR, whereas it still is not very tight for very low SNR values (see case D). However, as aforementioned, those values are likely to correspond to the no information region.
- Compared with Figure 6.4, a higher probability of outlier can be obtained under UMA for the same case study. The benefits provided by frequency diversity become smaller and smaller when few snapshots are available. In contrast, the gain resulting from the availability of multi-frequency observations becomes quite evident increasing the number of snapshots collected at each carrier frequency, especially for low values of the probability of outlier.

6.6 Simulation Results: MSE Approximation

So far, the robustness of the expressions characterizing the pairwise error probability under CMA and under UMA has been investigated in the multi-carrier case with reference to the probability of outlier. In this Section, the identified expressions are used to provide an accurate characterization of the MF ML DoA estimator performance for a multi-channel receiver operating in the threshold region.

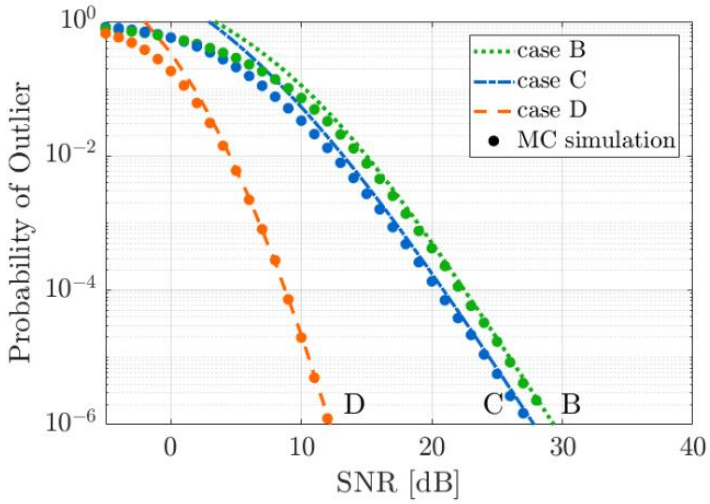

Figure 6.5: Probability of outlier under UMA for a three elements array $d = [0 \;\; 2 \;\; 6.8]\,\lambda_1$ for different case studies, reported in Table 6.1.

To this end, we resort to the approximate formula in (6.8) where

- P_m is given by (6.29) or (6.36) depending on the signal model, namely CMA or UMA;
- the CRB can be easily evaluated starting from the general expression of the Fisher information matrix $\mathbf{I}(\Theta)$ for the problem under consideration [52]

$$\mathrm{I}(\Theta)_{p,k} = \mathrm{tr}\left(\frac{\partial \boldsymbol{\Gamma}(\boldsymbol{\zeta})}{\partial \zeta^{(\mathrm{p})}}\boldsymbol{\Gamma}^{-1}(\boldsymbol{\zeta})\frac{\partial \boldsymbol{\Gamma}(\boldsymbol{\zeta})}{\partial \zeta^{(\mathrm{k})}}\boldsymbol{\Gamma}^{-1}(\boldsymbol{\zeta})\right) + 2\Re\left(\frac{\partial \mathbf{m}^{H}(\boldsymbol{\zeta})}{\partial \zeta^{(\mathrm{p})}}\boldsymbol{\Gamma}^{-1}(\zeta)\frac{\partial \mathbf{m}(\boldsymbol{\zeta})}{\partial \zeta^{(\mathrm{k})}}\right) \tag{6.40}$$

Where $\boldsymbol{\Gamma}(\boldsymbol{\zeta})$ and $\mathbf{m}(\boldsymbol{\zeta})$ are the covariance matrix and the mean vector of the received signal $\mathbf{x}$ and depend on a set of unknown parameters $\boldsymbol{\zeta}$, being $\boldsymbol{\zeta}$ a W-dimensional vector, so that p, k = 0, …, W – 1.

The application of (6.40) to the DoA estimation problem of interest herein yields two different expressions for the CRB, relative to the deterministic and stochastic signal models.

A. Deterministic Signal Model (or Conditional Model Assumption)

According to the definitions in Sections 6.4, we would have $\boldsymbol{\zeta} = [u_0 \;\; A_0(0) \ldots A_0(M_0 - 1) \ldots A_{N-1}(M_{N-1} - 1)]$, namely $W = Z + 1$, $\mathbf{m}(\boldsymbol{\zeta}) = \mathbf{q}$, being $\mathbf{q}$ defined in (6.19) and $\boldsymbol{\Gamma}(\boldsymbol{\zeta}) = \boldsymbol{\Gamma} = \mathbf{I}_{KZ}$. Therefore, after some algebra, the following expression is obtained

$$\mathrm{CRB}_{CMA}(\mathrm{u}_0) = \left[8\pi^2 \sum_{k=0}^{K-1}\left(d_k - \frac{1}{K}\sum_{p=0}^{K-1} d_p\right)^2 \sum_{n=0}^{N-1}\frac{M_n\,\mathrm{SNR}_n}{\lambda_n^2}\right]^{-1} \tag{6.41}$$

B. Stochastic Signal Model (or Unconditional Model Assumption)

According to the definitions in Sections 6.5, the set of unknown parameters would be reduced to a scalar $\boldsymbol{\zeta} = \mathrm{u}_0$, namely $W = 1$, while $\mathbf{m}(\boldsymbol{\zeta}) = \mathbf{0}$ and $\boldsymbol{\Gamma}(\zeta) = \mathbf{R}$.
Therefore, after some algebra, the following expression is obtained

$$\mathrm{CRB}_{UMA}(\mathrm{u}_0) = \left[8\pi^2 \sum_{k=0}^{K-1} \left(d_k - \frac{1}{K}\sum_{p=0}^{K-1} d_p\right)^2 \sum_{n=0}^{N-1} \frac{M_n \, \mathrm{SNR}_n}{\lambda_n^2 (1 + K \, \mathrm{SNR}_n)}\right]^{-1} \tag{6.42}$$

In both cases, the array layout affects the performance via the term $G = \sum_{k=0}^{K-1} \left(d_k - \frac{1}{K}\sum_{p=0}^{K-1} d_p\right)^2$ that basically measures the mean square distance of the array elements from a barycentre. Larger arrays (in the sense that the factor G is higher) yield better asymptotic performance.

However, a given layout yields a different impact when employed at different carrier frequencies and this impact is related to the SNR available at each frequency channel. As expected, (6.42) tends to (6.41) for high SNR values. In the following, aiming at demonstrating the reliability of the MSE approximation in (6.8) when using the expressions in (6.29), (6.36), (6.41) and (6.42), we compare the theoretical performance to the results of MC simulations.

As in Section 6.4, the number of trials was set to 10^6 and it was increased to $5 \cdot 10^7$for SNR values such that $P_0 < 10^{-4}$. In particular, Figure 6.6 shows the comparison between the MSE approximation and the results of MC simulations (dots) versus the SNR under CMA for case studies A-D, defined in Table 6.1. The corresponding CRB for each case is also reported in dashed grey. The three operative regions are quite easily identified and, as expected, the CRB is not able to model the ML estimator performance is the threshold region. In contrast, the considered MSE approximation is quite accurate in representing the performance of the estimator both in the threshold and the asymptotic region. This consideration applies both to the single-frequency cases A-B and to the multi-frequency situations C-D.

Notice that in the former situations, the results of [6] could have been fruitfully exploited. However, the reported analysis demonstrates that the approximate expression in (6.29) for the pairwise error probability provides a reliable tool that can be exploited both when a single frequency channel is available and when a multi-carrier receiver is considered. Remarkably, the approximate MSE can be successfully exploited to evaluate the lower limit SNR value that represents the boundary between the threshold region and the asymptotic region, namely the threshold SNR value. This value is heavily dependent on the probability of outlier (see Figure 6.4) in each considered case, the MSE significantly deviates from the CRB curve when P_0 gets above 10^{-5}. This could represent an interesting point of view when comparing different array layouts and frequency channels combinations.

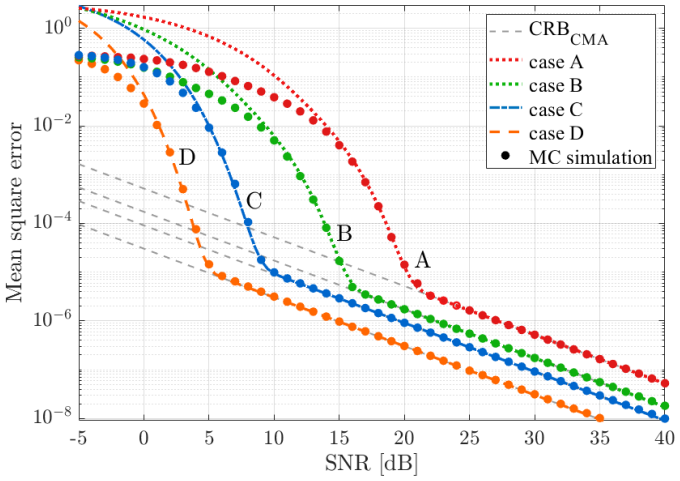

Figure 6.6: MSE approximation under CMA for a three-element array $\mathrm{d} = [0 \;\; 2 \;\; 6.8]\,\lambda_1$ for different case studies, reported in Table 6.1.

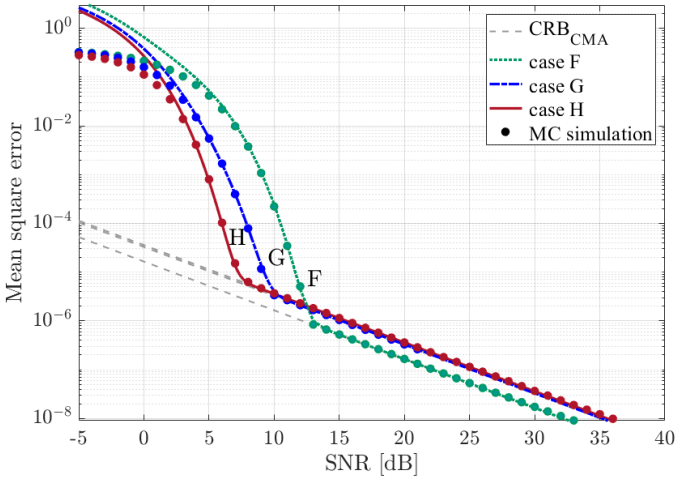

Figure 6.7: MSE approximation under CMA for different four-element arrays and one snapshot from each of three frequency channels.
The considered case studies are reported in Table 6.2.

For instance we report in Figure 6.7 the results obtained using two different array layouts for a four-element array when $M_n = M = 1$, $n = 0, \ldots, N-1$ snapshot is collected from each of the $N = 3$ frequency channels ($Z = 3$). Specifically, we consider the case studies F, G and H in Table 6.2.

Observing Figure 6.7, we notice that the more effective configuration in the asymptotic region is not necessarily the best also in the threshold region. Moreover, keeping constant the array layout and the number of frequency channels (e.g. see cases G and H), the choice of the carrier frequencies has a non-negligible impact on the threshold value, and this can be easily predicted using the proposed MSE approximation.

Table 6.2
Case studies F-I

	case F	case G	case H	case I
Number of array elements K	4	4	4	4
Number of carriers N	3	3	3	4
Number of snapshots M	1	1	1	1
Array layout	$d = [0\ 3.8\ 8.8\ 15.5]\lambda_1$		$d = [0\ 2\ 6.8]\,\lambda_1$	
Wavelengths	$\lambda_1,\ \lambda_2 = 0.76\,\lambda_1,\ \lambda_3 = 0.57\,\lambda_1$		$\lambda_1,\ \lambda_2 = 0.76\,\lambda_1$ $\lambda_4 = 0.68\,\lambda_1$	$\lambda_1,\ \lambda_2 = 0.76\,\lambda_1$ $\lambda_3 = 0.57\,\lambda_1$ $\lambda_4 = 0.68\,\lambda_1$
SNR	$\mathrm{SNR}_1 = \mathrm{SNR}_2 = \mathrm{SNR}_3$		$\mathrm{SNR}_1 = \mathrm{SNR}_2 = \mathrm{SNR}_4$	$\mathrm{SNR}_1 = \mathrm{SNR}_2 = \mathrm{SNR}_3 = \mathrm{SNR}_4$

In Figure 6.8 we compare the MSE approximation under UMA with the results of MC simulations versus the SNR for the aforementioned case studies C, D and H (see Table 6.1 and Table 6.2). Moreover, a new situation is also introduced, namely case I, exploiting the same three-element array as in C and D but with $M_n = M = 1$, $n = 0, \ldots, N-1$ snapshot from each of the $N = 4$ frequency channels (see Table 6.2 for details).

The following considerations are in order:

- the three operative regions are still quite easily identified for all cases.
- When only three snapshots are collected (see cases C and H), the MSE approximation slighly overestimates the performance in the threshod region. This is due to the fact that the union bound approximation does not appear tight in that situation, see e.g. case C in Figure 6.5.

6.7 Summary

In this Chapter, appropriate approximations to the MSE of a MF DoA ML estimator have been introduced to provide a reliable performance characterization in the threshold region. The reported analysis showed that the proposed MSE approximations are effectively able to model the performance of the estimator employing multiple observation possibly collected at different frequency channels both under CMA and under UMA.

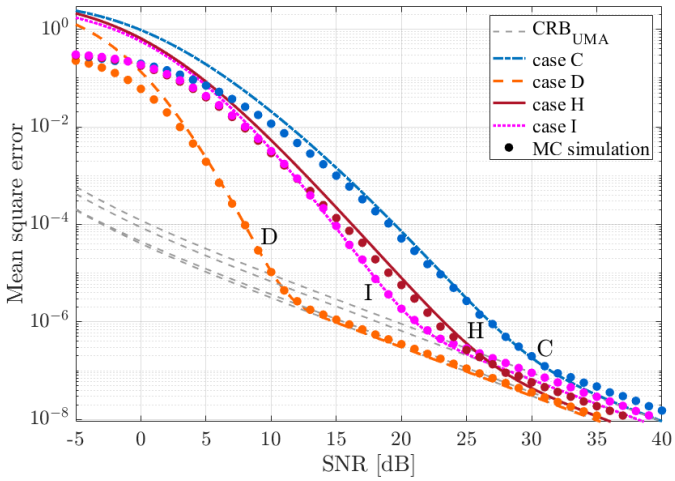

Figure 6.8: **MSE** approximation under UMA for different case studies reported in Table 6.1 and Table 6.2.

The capability of predicting the threshold SNR value can be a powerful tool that can be used in order to optimize the receiving system design. For instance, it can be exploited to identify a suitable array layout with the aim to control the insurgence of statistical ambiguities on target localization, especially in systems typically operating with low SNR levels and few antenna elements such as PCL systems. The benefits of jointly exploiting the spatial and frequency diversity will be shown in the following Chapter against real passive radar data.

Chapter 7
Target DoA estimation exploiting spatial and frequency diversity: Experimental Validation

In this Chapter and experimental validation is carried out to demonstrate the benefits stemming from the joint exploitation of spatial and frequency diversity. To this aim, dedicated test campaigns have been carried out in cooperation with the colleagues of Leonardo S.p.A. Specifically, two acquisition campaigns are considered, one aimed at carrying out a performance assessment for air surveillance application, the other aimed at detecting an localizing small drones.

First, the acquisition campaigns and the considered datasets are described, then we detail the employed processing scheme and finally, we report the experimental results obtained.

7.1 Multi-frequency ML DoA estimation for DVB-T based PCL system

Let us consider the availability of one reference antenna, steered toward the exploited IO and K surveillance antennas, steered toward the area to be monitored and able to simultaneously collect signals transmitted at N different carrier frequencies by the same emitter. The main processing stages of the multi-channel DVB-T based PCL system are reported in Figure 7.1. First, the basic PCL processing described in Section 1.1.2 is separately applied to each surveillance signal, with properly selected parameters, depending on the application. Then, the target detection and 2D localization are performed exploiting the MF information.

Target detection. Once the range-velocity maps have been evaluated at all the available surveillance channels the target detection stage is performed. Depending on the considered application, different MF operation approaches can be used. Specifically, for the aircraft surveillance application, the centralized detection scheme is used, namely first a NCI across

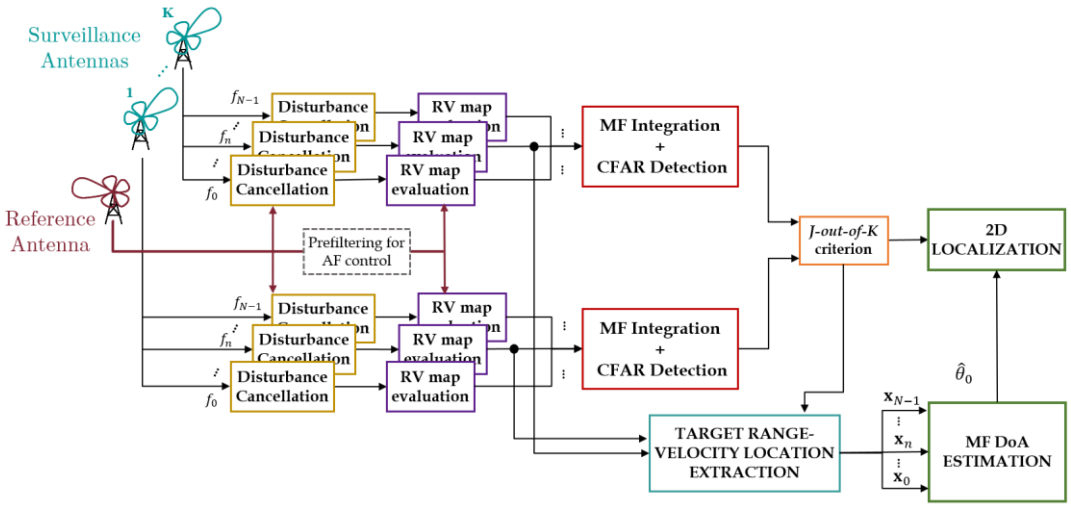

Figure 7.1: Processing scheme for a PCL system exploiting multiple frequency channels

the N DVB-T channels is applied then the output of this stage undergoes a MF CA-CFAR detection scheme. On the other hand, the decentralized detection scheme is adopted for the drone surveillance application, namely a detection is declared at a given bistatic range-bistatic velocity location when H detections out of N available frequency channels are obtained. In this case, a conventional CA-CFAR threshold is separately applied at each single frequency channel. Finally, a J– out of– K criterion can be applied to integrate the detection results obtained at the K surveillance channels.

2D localization. Once the target has been detected on the range-velocity plane, the DoA of the corresponding echo is estimated. To this end, we adopt the conventional ML approach described in Chapter 6 and briefly recalled here. For the n-th frequency channel, $n = 0, \ldots, N-1$, we consider the K range-velocity maps relative to the K surveillance antennas, and we assume to collect in a vector $\mathbf{x}_n$ the complex values extracted at the range-velocity location where the target has been detected. Vector $\mathbf{x}_n$ includes both target contribution and noise and is written as $\mathbf{x}_n = A_n\, \mathbf{s}_n(u_0) + \mathbf{n}_n$, which corresponds to eq. (6.1) when $M_n = 1$, $n = 0, \ldots, N-1$. Therefore, the ML estimate of the DoA u_0 is obtained as

$$\hat{u}_0 = \underset{u}{\operatorname{argmax}} \sum_{n=0}^{N-1} \frac{1}{\sigma_n^2} |\mathbf{s}_n{}^H(u)\, \mathbf{x}_n|^2 \tag{7.1}$$

where σ_n^2 is the noise power at the n-th frequency channel and $\mathbf{s}_n(u)$ is the spatial target steering vector in eq. (6.2) of Chapter 6.

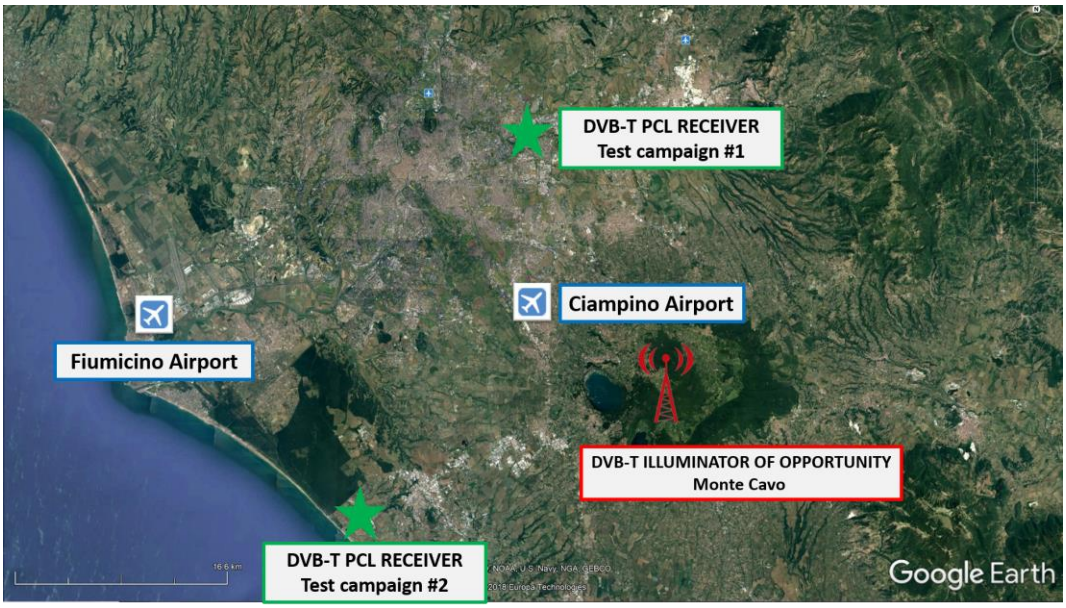

Figure 7.2: Acquisition geometries during test campaigns #1 & #2

7.2 Acquisition campaigns and adopted methodology

To demonstrate the effectiveness of the proposed strategy, dedicated test campaigns have been carried out in cooperation with the colleagues of Leonardo S.p.A using their DVB-T based AULOS passive sensor. Specifically, different tests have been carried out either at Leonardo S.p.A. premises in Rome, Italy (test campaign #1) or at the military airport of Pratica di Mare Airport, Rome, Italy (test campaign #2). The two acquisition geometries are sketched in Figure 7.2. In both test campaigns, the signals emitted by the Monte Cavo transmitter have been used as sources of opportunity and three Yagi-Uda antennas, displaced in the horizontal plane, have been used as to collect the surveillance signals, simultaneously emitted by the same IO at two or three DVB-T frequency channels. Table 7.1 reports the exploited DVB-T channels for each dataset.

During **test campaign #1**, the main beam of the surveillance antennas includes a Section of the civilian air traffic departing or arriving at Fiumicino and Ciampino airports. Live Air Traffic Control (ATC) registrations of the aircrafts present in the same area have been also collected. The availability of air-truth for the non-cooperative targets allowed us to carry out a quantitative analysis to evaluate the performance improvement. Two different array layouts have been considered namely two receiving sensors with positions d=[0 0.63]m and three antennas with positions d=[0 0.63 1.55]m. Further details on the considered data are reported in Table 7.1.

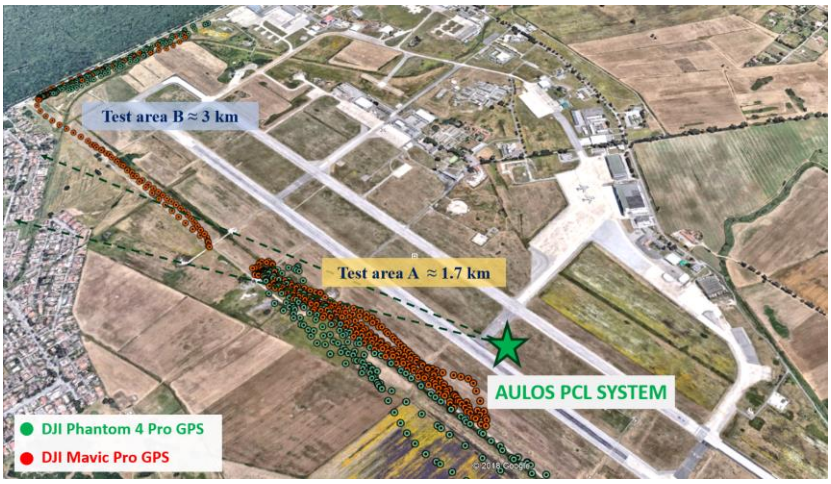

Figure 7.3: Enlarged view of the acquisition geometry during test campaign #2

Figure 7.4: Drones employed cooperative targets during test campaign #2

Test campaign #2 was carried out at Pratica di Mare airport (see the enlarged view of the acquisition geometry in Figure 7.3) to demonstrate the potentialities of PCL systems to offer simultaneous surveillance of aircraft and drones [70]. Two different array layouts have been considered namely two receiving sensors with positions $d = [0\ 0.63]m$ and three antennas with positions $d = [0\ 0.63\ 1.58]\ m$. During the test campaigns, two very small drones, flying in the surrounding area of the airport were employed as cooperative targets, see Figure 7.4. Specifically, a DJI Phantom 4 Pro of size approx. 25 cm $\times$ 25 cm (propellers excluded) is shown in Figure 7.4(a) and a DJI Mavic Pro of size approx. 20 cm long and 8.3 cm wide (propellers excluded) is shown in Figure 7.4(b). In the test campaigns, both drones were equipped with a GPS receiver in order to record their position and their trajectories are reported as green and red plots in Figure 7.3. We considered two different test areas. The first one was at a distance of about 1.7 km away from the receiver (Test area A in Figure 7.3 (b)), and the two drones flew along various paths reaching a minimum distance of 0.85 km up to a maximum distance of 1.93 km from the receiver site. In the second case, the drones flew up to the allowed boundaries of the airport area, yielding a maximum distance from the receiver of approx. 3 km (Test area B in Figure 7.3). Further details on the considered dastasets A & B are reported in Table 7.1.

Table 7.1
Details of the data sets collected during the performed tests campaigns.

	Test campaign #1	Test campaign #2	
		Dastaset A	Dastaset B
Number of drones	–	2	2
Number of datafiles	34	107	195
Scan duration [s]	0.45	0.6	1.4
CPI [s]	0.3	0.5	1
Total time duration [min]	≈ 2.1	≈ 8	≈ 17
Frequency channels	f_0 = 586 MHz f_1 = 714 MHz f_2 = 762 MHz	f_0 = 570 MHz f_1 = 754 MHz	f_0 = 570 MHz f_1 = 754 MHz
Number of surv. antennas	3	3	3
Test area,[min max] distance	–	A, [0.85 1.79] km	B, [2.15 3.18] km

Array layout selection Due to physical constraints, such as the minimum spacing between the antenna elements and a maximum feasible length, an extensive layout optimization was not possible. However, given a set of possible configurations and a set of available frequency channels for each test campaign, the best array layout was chosen based on the results of Chapter 6. The DoA estimation performance of the array layouts employed during test campaign #1 and #2 are reported in Figure 7.5 and Figure 7.6 , respectively, in terms of both probability of outlier and MSE. In each subfigure, both the SF and the MF cases are considered, under the simplifying assumption of equal SNRs and CMA. The improvement offered by the MF solutions is evident in both cases. In fact, we see that very low *P0* values (comparable to the *Pfa*) are obtained for SNR $\geq$ 12 dB when MF channels are exploited, see red lined in Figure 7.5(a) and Figure 7.6(a). Note that target echoes received with lower SNR are unlikely to be exceed the threshold and result in detection. In order words, once a target is detected, it is also likely for it to be correctly localized in the Cartesian plane, with a very good accuracy namely with MSE $\leq 10^{-4}$ thanks to the enhancement of target equivalent SNR resulting from the integration across the frequency channels.

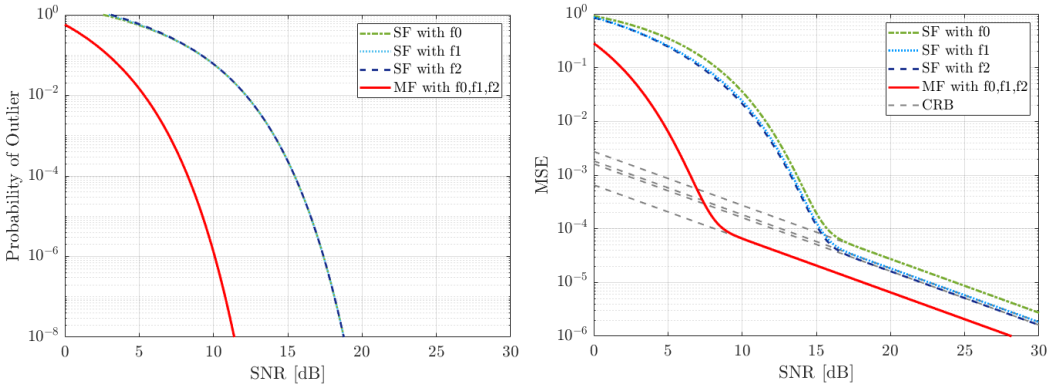

(a) (b)

Figure 7.5: DoA estimation performance for test campaign #1 under CMA
(a) Probability of outlier (b) MSE

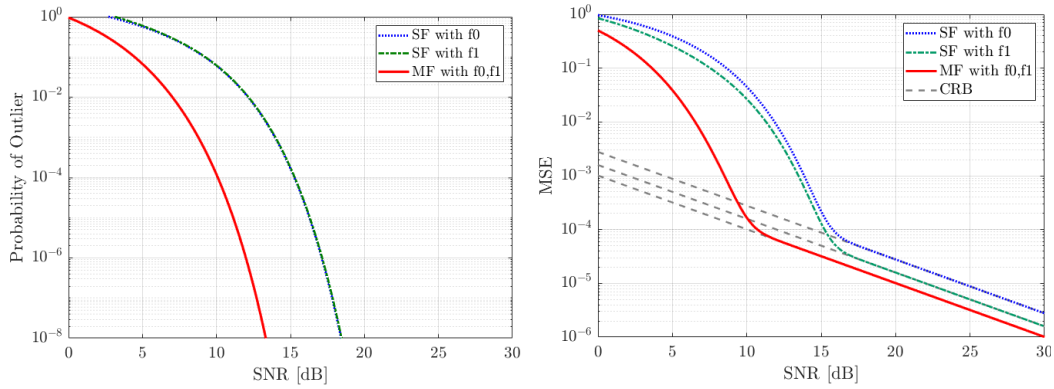

(a) (b)

Figure 7.6: DoA estimation performance for test campaign #2 under CMA
(a) Probability of outlier (b) MSE

7.3 Experimental Results

7.3.1 Test campaign #1: Aircraft surveillance

The results reported for the test campaign #1 are relative to a single target track, potentially observed at 34 consecutive data files, i.e. approx. 136s. All the available data files of each carrier frequency have been separately processed, according to the DVB-T PCL processing scheme reported in Figure 7.1. In particular, the disturbance cancellation stage is performed using ECA [22] with 1000 taps (i.e. 33 km @ $f_S = 64/7$ MHz). With reference to the target detection stage, we resort to a CA-CFAR with a nominal $Pfa = 10^{-6}$ on the final range-velocity plane, which results in different Pfa on each surveillance channel depending on the employed number of surveillance antennas.

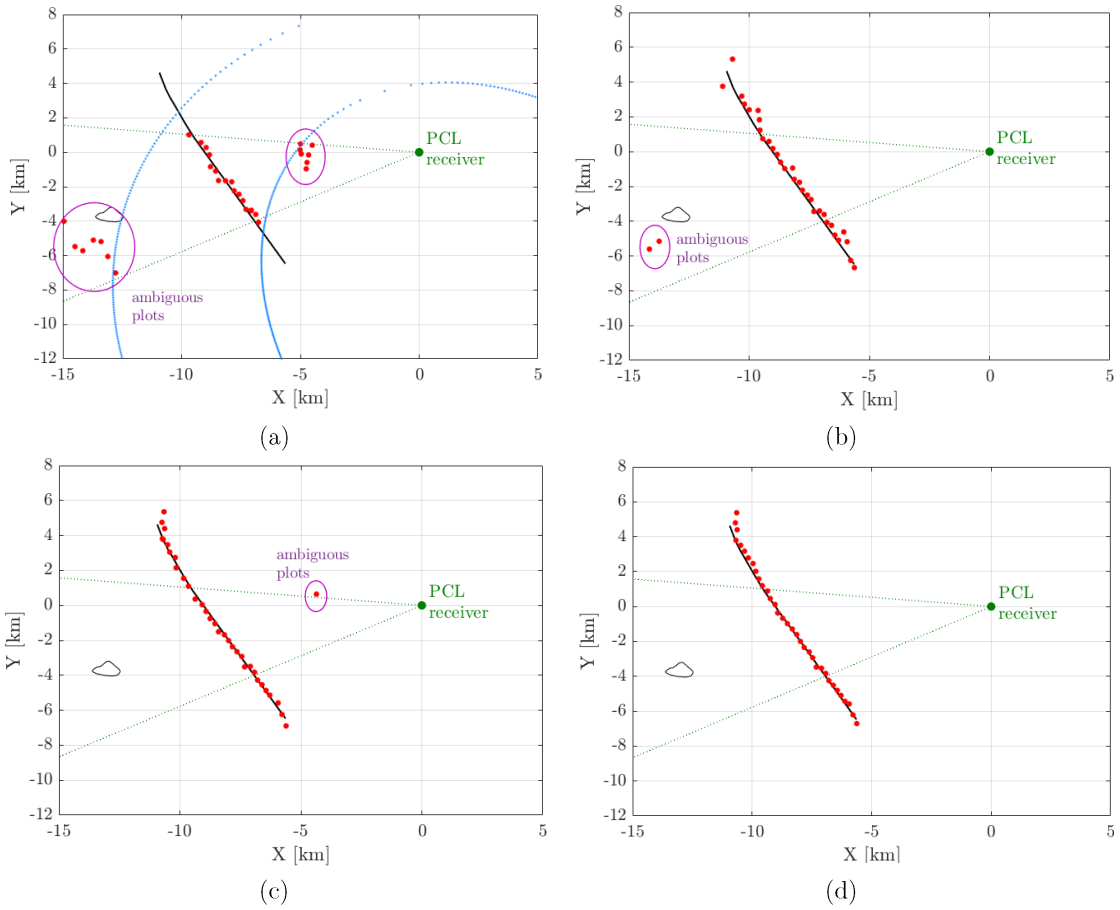

Figure 7.7: Test campaign #1: Localization results for 34 consecutive data files using (a) SF with f_1 and $K = 2$, (b) MF with $K = 2$, (c) SF with f_1 and $K = 3$, (d) MF with $K = 3$.

The localization results for the considered target of opportunity are reported in Figure 7.7 for different combinations of array layouts and employed frequency channels. Specifically, we compare the results on the XY plane, obtained using (a) the best performing single frequency (SF) channel $f_1 = 714$ MHz and two surveillance antennas; (b) the MF approach with two surveillance antennas, (c) the SF channel f_1 and three surveillance antennas; (d) the MF approach with three surveillance antennas.

In all sub-figures, the black line represents the ATC data while red dots are used to plot the PCL detections correctly associated to the considered target in the bistatic range – bistatic velocity plane. Finally, dotted green lines represent the beam width of surveillance array and, when present, the plots that have been correctly associated but are ambiguously localized in the XY plane are highlighted with purple circles. Finally, two iso-bistatic range ellipses are sketched in dashed light blue dots in Figure 7.7(a). A quantitative comparison in terms of number of correct detections and ambiguously localized plots is reported in Table 7.2, for different combinations of employed frequency channels and array layouts.

Table 7.2
Test campaign #1: Target detections and ambiguous plots

	Correct detections		Ambiguous plots	
	K = 2	K = 3	K = 2	K = 3
SF with f_0	26	28	7	2
SF with f_1	30	32	14	1
SF with f_2	26	26	12	2
MF with f_0, f_1, f_2	33	34	2	0

The following considerations are in order:

- When $N = 1$ and $K = 2$ (see Figure 7.7(a)), the target DoA is estimated unambiguously only in a narrow angular sector while the PCL plots located outside this sector are mis-localized (see purple circles). Figure 7.7(a) also shows that the localization errors are exclusively due to ambiguous angle measurements since the ambiguous plots lie on the correct iso - bistatic range ellipses but their estimated DoA show a distance of approx. 39° from the real one, as expected for the ambiguous angular sector.
- The advantage of the MF operation is evident in Figure 7.7(b), where a centralized detection scheme using all the three available channels is adopted [68] while the proposed MF ML approach is considered for DoA estimation. Specifically, the maximization of (7.1) is performed over a wide angular sector equal to [-80°: 0.01: 80°]. As is apparent, the MF solution allows to avoid the ambiguous estimation of the DoA for targets' plots outside the SF angular sector. However, there is a non-zero probability that outliers could occur when two antennas are considered. As illustrated in Table 7.2 two ambiguous localizations are obtained, also highlighted with purple circles.
- Observing Table 7.2 we might notice that a significantly reduced number of ambiguous plots is obtained when exploiting three receiving antennas for all the SF operations. In particular, using f_1, the number of ambiguous plots turns from 14 to just 1.
- When considering three nun-uniformly spaced surveillance antennas and the three available DVB-T channels, the total amount of detected target plots is unambiguously localized in the XY plane.
- Moreover, as expected by the theoretical analysis in Figure 7.5, it is worth mentioning that a further improvement is offered by the proposed strategy in terms of DoA estimation accuracy. In fact, the advantage is evident if we compare the proposed solution (Figure 7.7(d)) with the exploitation of two receiving antennas when the best DVB-T channel is employed.

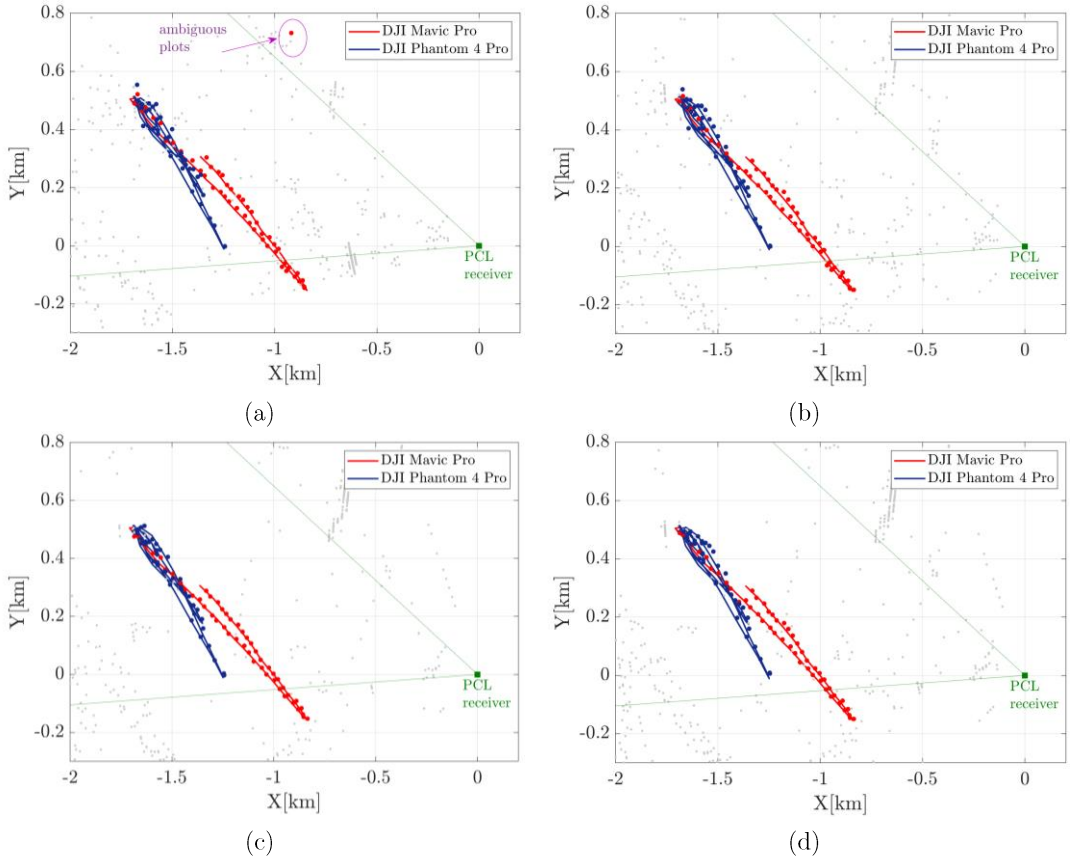

Figure 7.8: Dataset A: Localization results for 50 consecutive data files using (a) SF with f_0 and $K = 2$, (b) MF with $K = 2$, (c) SF with f_0 and $K = 3$, (d) MF with $K = 3$.

7.3.2 Test campaign #2: Drone surveillance

The results reported for the test campaign#2 are relative to the two cooperative target tracks, potentially observed at 50 consecutive data files. All the available data files of each carrier frequency have been separately processed, according to the DVB-T PCL processing scheme reported in Figure 7.1. In particular, the disturbance cancellation stage is performed using the sliding version of the ECA (ECA-S) [21] which allows a good trade-off between disturbance cancellation and the capability to preserve low-velocity target echoes. To this aim, we recall that the batch duration T_B is selected to obtain remarkable cancellation performance while preserving targets moving at the minimum Doppler of interest (notch Doppler extension $\Delta f_n = 1/T_B$). In contrast, T_S is selected in order to move out of the velocity range of interest the undesired structures that arise from the batch processing of the received signals. For this dataset, we used $T_B = 0.2$ s, *i.e.* $\Delta f_n = 5$Hz over a range of 6 km. Finally, the maximum observed velocity is limited at 50 m/s, so that $T_S = 5.2$ ms and $T_S = 3.9$ ms for $f_0 = 570$ MHz and $f_1 = 754$ MHz, respectively. With reference to the target detection stage, we resort to a CA-CFAR with a nominal $Pfa = 10^{-7}$ on the final range-velocity plane, which

results in different *Pfa* on each surveillance channel depending on the employed number of surveillance antennas.

The localization results obtained for the Datasets A and B are reported in Figure 7.8 and Figure 7.9, respectively for different combinations of array layouts and employed frequency channels. Specifically, in both cases we compare the results on the XY plane, obtained using (a) the single frequency (SF) channel $\boldsymbol{f_0}$ and 2 surveillance antennas ($K = 2$); (b) the MF approach with $K = 2$, (c) the SF channel $\boldsymbol{f_0}$ and 3 surveillance antennas ($K = 3$); (d) the MF approach with $K = 3$. In all figures, the raw detections from the PCL system obtained across 50 consecutive data files, projected into the XY plane, are reported in grey dots. Blue and red lines represent the GPS trajectories of the two drones. Red and blue dots are used to plot the PCL detections correctly associated to the DJI Mavic Pro and DJI Phantom 4 Pro GPS, respectively, on the bistatic range – bistatic velocity plane. Finally, dotted green lines represent the beam width of surveillance array and, when present, the plots that have been correctly associated but are ambiguously localized in the XY plane are highlighted with purple circles.

A quantitative comparison in terms of number of correct detections and ambiguously localized plots is reported in Table 7.3 and Table 7.4, respectively, for different combinations of employed frequency channels and array layouts.

By observing Figure 7.8, Figure 7.9, Table 7.3 and Table 7.4, the following considerations are in order:

- When the drones flew at short distance (see Dataset A), the two single DVB-T channels yield comparable detection results. Note that the DJI Mavic Pro has a correct detection rate of 100% over the available 50 scans. In this case, the use of MF strategies does yield any significant improvement with respect to the SF operation. In contrast, from the localization point of view, the MF approach allows to correctly localize all plots in the Cartesian plane (see Table 7.4 and Figure 7.8(b)) even operating with two surveillance antennas.

- When the drones flew at short distance (see Dataset B), the target detection capability varies with the employed single DVB-T channel and the best performing frequency channel varies with the considered target. Therefore, in this case, the MF approach yields a remarkable improvement with respect to the worst operation of each target. Moreover, the exploitation of MF for target localization avoids the ambiguous localization of targets flying outside the unambiguous angular sector provided by the SF solution. However, there is a non-zero probability that outliers occur when two antennas are considered. In fact, in the considered test, two ambiguous plots are obtained as highlighted by the purple circle in Figure 8.5(b).

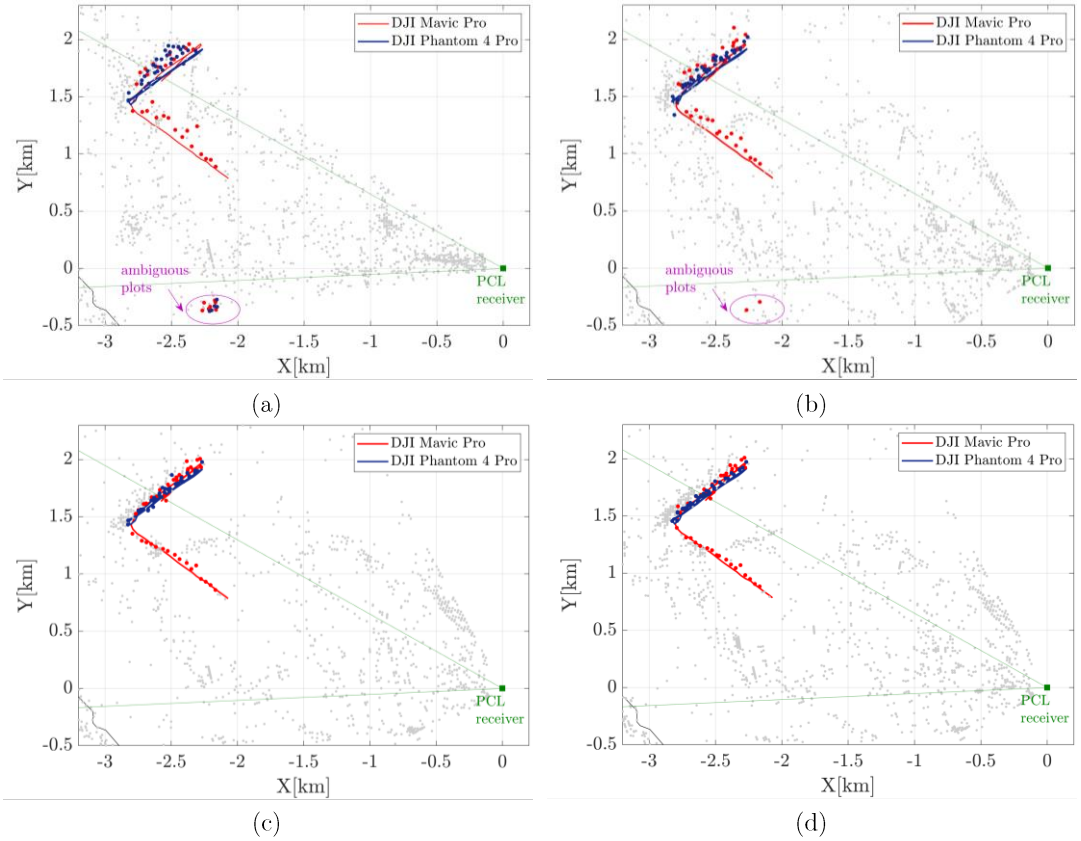

Figure 7.9: Dataset B: Localization results for 50 consecutive data files using (a) SF with f_0 and $K = 2$, (b) MF with $K = 2$, (c) SF with f_0 and $K = 3$, (d) MF with $K = 3$.

- When a non-uniform array configuration is used to increase at the same time both the DoA estimation accuracy and the unambiguous angular sector, the number of ambiguously detected plots is zero (see Table 7.4) . The use of three antennas also allows a more accurate localization. The improvement is evident if comparing Figure 7.8(c) and Figure 7.9(c) with Figure 7.8(a) and Figure 7.9(a), but it is particularly apparent when considering the Dataset B.

- Eventually, a further improvement in terms of localization results might be achieved by jointly exploiting multiple frequency channels and surveillance antennas, see Figure 7.8(d) and Figure 7.9(d). Note that the localization improvement is not substantial against the considered targets since remarkable localization performance was obtained with the two single DVB-T channels.

Table 7.3
Test campaign #2 : Target detections over 50 consecutive datafiles

		DJI Mavic Pro		DJI Phantom 4 Pro	
		$K = 2$	$K = 3$	$K = 2$	$K = 3$
Dataset A	SF with f_0	50	50	35	37
	SF with f_1	50	50	38	36
	MF	50	50	38	37
Dataset B	SF with f_0	39	42	35	36
	SF with f_1	30	32	42	41
	MF	41	43	41	40

Table 7.4
Test campaign #2 : Ambiguous plots over 50 consecutive datafiles

		DJI Mavic Pro		DJI Phantom 4 Pro	
		$K = 2$	$K = 3$	$K = 2$	$K = 3$
Dataset A	SF with f_0	1	0	0	0
	SF with f_1	9	0	0	0
	MF	0	0	0	0
Dataset B	SF with f_0	7	0	5	0
	SF with f_1	11	0	24	0
	MF	2	0	0	0

7.4 Summary

The purpose of this Chapter was to address the problem of the target DoA estimation in PCL system. To relax the typical trade-off between DoA estimation accuracy and unambiguous angular sector, we resorted to a non-uniform arrangement of the surveillance antenna elements and we jointly exploited the signals simultaneously collected at different carrier frequencies. Th experimental validation was carried out against two real data sets collected by the DVB-T based AULOS PCL system from Leonardo S.p.A. for both aircraft and drone surveillance applications. The experimental analysis allowed to illustrate the benefits of the proposed approach. Specifically, we have shown that, although an extensive optimization could not be performed due to physical constraints, we showed that the derived performance characterization can be used in order to select the best performing configuration that allows to: (i) extend the angular sector where the target DoA can be unambiguously estimated (ii) improve the target DoA estimation accuracy.

Chapter 8
Conclusion and future work

As stated in the introduction, the goal of this thesis was to address the main limitations of PCL technology by resorting to the exploitation of the information diversity conveyed by multiple receiving channels. The research performed to reach this goal has led to achievements that have a broad scope of application, not limited to passive radar systems. The main novelties that this research resulted in are reported in this Chapter, followed by some recommendations for future research.

8.1 Results and novelties

The main innovative contributions made by this thesis have been divided in two parts.

In the **first part** of this thesis, we have addressed the problem of exploiting signals collected by differently polarized antennas.

1. *The benefits of exploiting polarization diversity in PCL systems have been demonstrated.* Following the promising results obtained using signals in the FM radio band, suitable strategies that exploit the polarimetric information have been considered and a performance assessment has been carried out against DVB-T based PCL data. We have shown that this information diversity can improve the target detection performance of passive radars, not only by increasing the target contribution but also by counteracting the disturbance sources.
2. *A novel polarimetric adaptive detection scheme has been derived by resorting to a parametric approach.* The problem of target detection in coherent radar systems exploiting polarimetric diversity has been addressed by modelling the disturbance affecting the data as a multi-channel AR process. A complete theoretical characterization of the asymptotic performance of the derived detector is provided, using two different target fluctuation models, namely Swerling 0 and Swerling I. A numerical analysis demonstrated that the proposed detector effectively improves the target detection capability while relaxing the requirements on the training data size and the computational burden with respect to existing solutions.

3. *An appropriate modification to the derived polarimetric model-based adaptive detection scheme is introduced to make it robust to typical spectral model mismatches.* Based on the effectiveness demonstrated against clutter with characteristics exactly matching the adopted parametric model, the performance assessment of the novel target detection scheme has been extended to include the case of disturbance components with diverse spectral characteristics. Consequently, the derived detector has been slightly modified. An extensive numerical analysis showed the effectiveness of the resulting detection approach and its robustness to spectral model mismatches.
4. *The effectiveness of the developed strategies has been demonstrated via an experimental validation.* After an extensive performance assessment against simulated data, an experimental validation has been carried out against two different datasets. First, being the field of application of the derived solution not limited to PCL systems, the effectiveness of the proposed approach has been demonstrated against data collected by a polarimetric active radar system. Then, its benefits have also been demonstrated by processing data collected by a PCL system exploiting FM radio signals.

In the **second part** of this work, we have addressed the problem of target DoA estimation in systems that jointly exploit signals received at multiple carrier frequencies.

5. *We have derived a theory for predicting the performance of the MF ML DoA estimator in the threshold region.* We have provided a reliable performance characterization, in low SNR scenario, of a DoA estimator using a sensor array simultaneously collecting signals emitted by a single source at multiple carrier frequencies. We have separately treated the case of deterministic and stochastic signal model and we have derived approximations of the MSE and probability of outlier in both cases.
6. *Results from extensive MC simulations showed that the derived expressions could accurately describe the sought threshold region performance.* An extensive numerical analysis has been carried out to prove the reliability of the derived theoretical expressions, under both deterministic and stochastic signal model assumptions. Based on the developed tool, the benefits of the multi-carrier approach can be easily characterized and potentially used to address robust design optimization of the sensor array layout.
7. *The benefits of the multi-carrier approach have been demonstrated against real data.* Dedicated experimental campaigns have been carried out with Leonardo S.p.A. using AULOS DVB-T based PCL system with the purpose of demonstrating this advantage against both aircraft and small UAVs. Although an extensive array layout optimization could not be performed due to physical constraints, we showed that the derived performance characterization can be used in order to select the best performing configuration that allows to: (i) extend the angular sector where the target DoA can be unambiguously estimated (ii) improve the estimation accuracy.

8.2 Future Outlook

During this work, the following key points and areas of further research were identified.

- *Extension of the novel polarimetric model-based adaptive detection scheme to include the frequency diversity.* The detection approaches presented in Part I of this thesis only consider the exploitation of a single-frequency channel. However, it has been shown that the target detection performance highly depends on the selected IO and, in particular, it significantly varies with the employed frequency channel. In fact the selection of a given frequency channel among those emitted by a specific IO implies a number of radar parameters must be inherently fixed, such as the carrier frequency and, in turn, the radiating characteristics of the TX. However, Broadcast IOs inherently offer the availability of multiple signals emitted by the same transmitted and simultaneously collected by the PCL receiver at different carrier frequencies. Based on these consideration, as a future activity, we will build upon the results obtained in the first part of this thesis and we will consider the joint exploitation of polarization and frequency diversity. The advantages arising from considering these information diversities jointly have been preliminary demonstrated in the literature, using a multi frequency and multi polarimetric GLRT detector [17]. Following the promising results obtained in the latter paper, and based on the results of Chapter 5 of this thesis, we expect that a further improvement can be obtained if the Mod-Pol-AR-AMF approach is extended to the multi-frequency scenario, in terms of target discrimination capability against interfering sources as well as increased robustness with respect to the time-varying characteristics of the exploited signals of opportunity.
- *Efficient implementation of the derived detection strategies.* The computational burden of the detection schemes developed in this thesis must be carefully evaluated and possibly reduced to enable real-time operations. This is surely the case when multiple frequency channels are jointly considered as it would yield a tremendous enhancement in terms of computational burden.
- *Derivation of a new model-based polarimetric adaptive detection scheme by resorting to a one-stage GLRT approach.* The results obtained in Chapters 2-5 stimulate future investigations along the line of polarimetric model-based detection strategies. Based on the same multichannel parametric model adopted for the disturbance in Chapter 3, a new detection scheme will be derived by following a one-step GLRT, namely by formulating the decision process using all the available data. It is expected that such approach further increases the target detection performance of the multi-polarimetric radar system.

- *Derivation of an optimization criterion to design the receiving system.* In Chapter 6, the capability of predicting the performance of the MF ML DoA estimator in the threshold region has been demonstrated. As pointed out, the derived theoretical characterization is a powerful tool that can be used in order to optimize the receiving system design. As a future activity in this area, an optimization criterion must be formulated and exploited to identify suitable array layouts and carried frequency selection with the aim to control the insurgence of statistical ambiguities on target localization. The preliminary results shown in Chapter 7 suggest that this tool is particularly useful for the design of passive sensors that typically receive weak echoes from low RCS targets, as they usually operate in the threshold SNR region.

The effectiveness of the obtained strategies will be extensively tested and validated via both simulated and real data. In particular, *ad hoc* acquisition campaigns will be carried out using PCL prototypes exploiting different sources of opportunity, such as FM radio, DVB-T, DVB-S. The expected improvement obtained with the strategies proposed in this thesis and the ones that will be foreseen in the near future both in terms of detection and localization capability will further enable the possibility of using PCL sensors in different surveillance scenarios.

Appendices

Appendix A
Derivation of the AR model based polarimetric detector

We maximize the numerator of (3.15) over the unknown target amplitude vector $\boldsymbol{\alpha}$, where the likelihood of $\mathbf{X}_0$ under the H_1 hypothesis is defined in (3.14). The maximization yields:

$$\hat{\boldsymbol{\alpha}} = \underset{\boldsymbol{\alpha}}{\operatorname{argmin}} \{\operatorname{tr}(\mathbf{S}^H\mathbf{P}\mathbf{S}) - 2\Re[\operatorname{tr}(\mathbf{X}_0^H\mathbf{P}\mathbf{S})]\} \tag{A.1}$$

Considering the definitions of matrices $\mathbf{X}_0$ and $\mathbf{S}$ provided in sub-Section 3.2.1, we can further develop the expression above as

$$\hat{\boldsymbol{\alpha}} = \underset{\boldsymbol{\alpha}}{\operatorname{argmin}} \left\{ \sum_{k=0}^{M-Q} \boldsymbol{\alpha}^H \boldsymbol{\Sigma}^H(k)\mathbf{P}\,\boldsymbol{\Sigma}(k)\,\boldsymbol{\alpha} - 2\Re\left[\sum_{k=0}^{M-\mathrm{Q}} \tilde{\mathbf{x}}_0{}^H(k)\mathbf{P}\boldsymbol{\Sigma}(k)\,\boldsymbol{\alpha} \right] \right\} \tag{A.2}$$

where $\boldsymbol{\Sigma}(k) = \tilde{\mathbf{t}}(k) \otimes \mathbf{I}_L$.
By defining $\mathbf{U} = \sum_{k=0}^{M-Q} \boldsymbol{\Sigma}^H(k)\mathbf{P}\,\boldsymbol{\Sigma}(k)$ and $\mathbf{v} = \sum_{k=0}^{M-\mathrm{Q}} \tilde{\mathbf{x}}_0{}^H(k)\mathbf{P}\boldsymbol{\Sigma}(k)$, (A.2) becomes

$$\hat{\boldsymbol{\alpha}} = \underset{\boldsymbol{\alpha}}{\operatorname{argmin}} \{\boldsymbol{\alpha}^H\mathbf{U}\boldsymbol{\alpha} - 2\Re[\mathbf{v}\boldsymbol{\alpha}]\} \tag{A.3}$$

that yields the following ML estimate for the target amplitude vector:

$$\hat{\boldsymbol{\alpha}} = \mathbf{U}^{-1}\mathbf{v}^H \tag{A.4}$$

Eventually, by substituting (A.4) in (3.15) we obtain

$$\frac{\max_{\boldsymbol{\alpha}}\{f_1(\mathbf{X}_0|\,\boldsymbol{\alpha},\mathbf{R},\mathbf{A})\}}{f_0(\mathbf{X}_0|\mathbf{R},\mathbf{A})} = 2\Re[\hat{\boldsymbol{\alpha}}^H\,\mathbf{v}^H] - \hat{\boldsymbol{\alpha}}^H\mathbf{U}\hat{\boldsymbol{\alpha}} = \mathbf{v}\mathbf{U}^{-1}\mathbf{v}^H \underset{H_0}{\overset{H_1}{\gtrless}} \ln(\eta_0) \tag{A.5}$$

which, scaled by a constant factor 2 , is converted in (3.16).

Appendix B
ML Parameter Estimation for Pol-AR-AMF

The joint pdf of the secondary data is given by (3.22). We first look for matrix $\mathbf{A}$ that maximizes or, equivalently, that minimizes $\mathrm{tr}(\overline{\mathbf{X}}^H \mathbf{P}\, \overline{\mathbf{X}})$, where $\mathbf{P} = \mathbf{H}^H \mathbf{R}^{-1} \mathbf{H}$ and $\mathbf{H} = [-\mathbf{A}^H \quad \mathbf{I}_L]$. To this purpose, we define matrix $\widehat{\mathbf{Q}} = \overline{\mathbf{X}}\, \overline{\mathbf{X}}^H$ that is decomposed in blocks as

$$\widehat{\mathbf{Q}} = \begin{bmatrix} \widehat{\mathbf{Q}}_{00} & \widehat{\mathbf{Q}}_{01} \\ \widehat{\mathbf{Q}}_{01}^H & \widehat{\mathbf{Q}}_{11} \end{bmatrix} \tag{B.1}$$

where $\widehat{\mathbf{Q}}_{00}$ and $\widehat{\mathbf{Q}}_{11}$ are square blocks with dimensions $L(Q-1)\times L(Q-1)$ and $L\times L$ respectively, whereas $\widehat{\mathbf{Q}}_{01}$ is a $L(Q-1)\times L$ block.
With this definition, we can write:

$$\begin{aligned} \mathrm{tr}(\overline{\mathbf{X}}^H \mathbf{P}\, \overline{\mathbf{X}}) &= \mathrm{tr}\big(\widehat{\mathbf{Q}}\, \mathbf{H}^H \mathbf{R}^{-1} \mathbf{H}\big) \\ &= \mathrm{tr}\big(\widehat{\mathbf{Q}}_{00} \mathbf{A} \mathbf{R}^{-1} \mathbf{A}^H - \widehat{\mathbf{Q}}_{01} \mathbf{R}^{-1} \mathbf{A}^H - \widehat{\mathbf{Q}}_{01}^H \mathbf{A} \mathbf{R}^{-1} + \widehat{\mathbf{Q}}_{11} \mathbf{R}^{-1}\big) \end{aligned} \tag{B.2}$$

and using well known identities for trace derivatives, we have:

$$\frac{\partial}{\partial \mathbf{A}^*} \{\mathrm{tr}(\overline{\mathbf{X}}^H \mathbf{P}\, \overline{\mathbf{X}})\} = \widehat{\mathbf{Q}}_{00} \mathbf{A} \mathbf{R}^{-1} - \widehat{\mathbf{Q}}_{01} \mathbf{R}^{-1} \tag{B.3}$$

that is equated to zero to obtain the ML estimate of matrix $\mathbf{A}$:

$$\widehat{\mathbf{A}} = \widehat{\mathbf{Q}}_{00}^{-1} \widehat{\mathbf{Q}}_{01} \tag{B.4}$$

Now, by substituting (B.4) in (3.22) we obtain

$$\max_{\mathbf{A}} \{f_0(\overline{\mathbf{X}} |\, \mathbf{R}, \mathbf{A})\} = (\pi^L |\mathbf{R}|)^{-P(M-Q+1)} \exp\big\{-\mathrm{tr}\big(\widehat{\mathbf{H}}\, \widehat{\mathbf{Q}}\, \widehat{\mathbf{H}}^H \mathbf{R}^{-1}\big)\big\} \tag{B.5}$$

that can be then maximized with respect to $\mathbf{R}$ thus yielding:

$$\widehat{\mathbf{R}} = \frac{1}{P(M-Q+1)} \widehat{\mathbf{H}}\, \widehat{\mathbf{Q}}\, \widehat{\mathbf{H}}^H = \frac{1}{P(M-Q+1)} \left(\widehat{\mathbf{Q}}_{11} - \widehat{\mathbf{Q}}_{01}^H \widehat{\mathbf{Q}}_{00}^{-1} \widehat{\mathbf{Q}}_{01} \right) \tag{B.6}$$

where $\widehat{\mathbf{Q}}_{11} - \widehat{\mathbf{Q}}_{01}^H \widehat{\mathbf{Q}}_{00}^{-1} \widehat{\mathbf{Q}}_{01} = \left[\widehat{\mathbf{Q}}^{-1} \right]_{\mathrm{Q,Q}}^{-1}$ is the inverse of the last $L \times L$ block on the main diagonal of $\widehat{\mathbf{Q}}$.

We note that the derived expressions for matrices $\widehat{\mathbf{A}}$ and $\widehat{\mathbf{R}}$ reported in (B.4) and (B.6), respectively, are approximations of the actual ML estimates of the AR parameters, given that the pdf in (3.10) is the approximate (actually conditional) pdf of the data. However, the approximation is quite accurate for large data records, provided that the actual pdf can be well approximated by the conditional pdf [15],[58].

Appendix C
PDF of $\check{\mathbf{z}}_0$ under the H_0 hypothesis

In this Appendix, we look for the pdf of vector $\check{\mathbf{z}}_0$, defined as $\check{\mathbf{z}}_0 = \mathbf{C}^H\mathbf{B}^H\mathbf{x}_0$, under the H_0 hypothesis, provided that matrices $\mathbf{B}$ and $\mathbf{C}$ are known. Based on its definition and (3.10) it is easy to observe that $\check{\mathbf{z}}_0|_{H_0} \sim \mathcal{CN}(\mathbf{0}_{L\times 1}, \mathbf{D}_0)$, denoting $\mathbf{D}_0$ as the disturbance covariance matrix that will be derived in the following .

From (3.17), we write $\check{\mathbf{z}}_0$ as $\check{\mathbf{z}}_0 = \sum_{m=0}^{M-Q} \check{\mathbf{z}}_{0,m}$, namely as the sum of $M - Q - 1$ vectors $\check{\mathbf{z}}_{0,m} = \sqrt{2}\mathbf{W}^{-1/2}\,\mathbf{V}^H(m)\,\tilde{\mathbf{x}}_0(m)$, each being a $L\times 1$ zero-mean complex Gaussian variable with cross-covariance matrix

$$E\{\check{\mathbf{z}}_{0,m}\check{\mathbf{z}}_{0,n}^H\} = 2\,\mathbf{W}^{-\frac{1}{2}}\,\mathbf{V}(m)^H E\{\tilde{\mathbf{x}}_0(m)\tilde{\mathbf{x}}_0{}^H(n)\}\,\mathbf{V}(n)\,\mathbf{W}^{-\frac{1}{2}} \qquad (m,\ n = 0,\ \ldots,\ M-Q) \tag{C.1}$$

where $E\{\tilde{\mathbf{x}}_0(m)\tilde{\mathbf{x}}_0{}^H(n)\}$ is a $QL\times QL$ block of the disturbance covariance matrix $\mathbf{M}$, whose diagonal is coincident with the main diagonal of $\mathbf{M}$ only if $m = n$.

Using the definition of matrices $\mathbf{V}(m) = \mathbf{P}\,\boldsymbol{\Sigma}(m)$ and $\mathbf{P} = \mathbf{H}^H\mathbf{R}^{-1}\mathbf{H}$, (C.1) becomes

$$E\{\check{\mathbf{z}}_{0,m}\check{\mathbf{z}}_{0,n}^H\} = 2\,\mathbf{W}^{-\frac{1}{2}}\,\boldsymbol{\Sigma}(m)^H\mathbf{H}^H\mathbf{R}^{-1}\mathbf{H}\,E\{\tilde{\mathbf{x}}_0(m)\tilde{\mathbf{x}}_0{}^H(n)\}\,\mathbf{H}^H \times \mathbf{R}^{-1}\mathbf{H}\,\boldsymbol{\Sigma}(n)\mathbf{W}^{-\frac{1}{2}} \qquad (m,\ n = 0,\ \ldots,\ M-Q) \tag{C.2}$$

According to the employed multi-channel AR model in (3.9), we write the product $\mathbf{H}E\{\tilde{\mathbf{x}}_0(m)\tilde{\mathbf{x}}_0{}^H(n)\}\mathbf{H}^H$ as

$$E\,\{[\mathbf{H}\,\tilde{\mathbf{x}}_0(m)]\,[\tilde{\mathbf{x}}_0{}^H(n)\,\mathbf{H}^H]\} = E\,\{\mathbf{w}(m\,+\,Q\,-\,1)\mathbf{w}^H(n\,+\,Q\,-\,1)\} = \mathbf{R}\,\delta(m-n) \tag{C.3}$$

denoting $\delta(\cdot)$ as the Dirac delta function.

Finally, by substituting (C.3) into (C.2), we easily obtain

$$E\{\check{\mathbf{z}}_{0,m}\check{\mathbf{z}}_{0,n}^H\} = \begin{cases} 2\mathbf{W}^{-\frac{1}{2}}\,\boldsymbol{\Sigma}^H(m)\,\mathbf{P}\,\boldsymbol{\Sigma}(m)\,\mathbf{W}^{-\frac{1}{2}} & m = n \\ \mathbf{0}_L & m \neq n \end{cases} \tag{C.4}$$

Therefore, the sought covariance matrix $\mathbf{D}_0$ is

$$\mathbf{D}_0 = 2\mathbf{W}^{-\frac{1}{2}}\left[\sum_{m=0}^{M-Q}\boldsymbol{\Sigma}^H(m)\mathbf{P}\,\boldsymbol{\Sigma}(m)\right]\mathbf{W}^{-\frac{1}{2}} = 2\mathbf{I}_L \tag{C.5}$$

Based on (C.5), we can conclude that $\check{\mathbf{z}}_0|_{H_0} \sim \mathcal{CN}(\mathbf{0}_{L\times 1}, 2\mathbf{I}_L)$.

Appendix D
Derivation of the asymptotic Pol-AR-AMF Pd for fluctuating target

In this Appendix, we look for $\text{Prob}\{\|\check{\mathbf{z}}_0\|^2 > \eta\}$, assuming that vector $\check{\mathbf{z}}_0$ is a complex Gaussian random variable with zero-mean vector and covariance matrix $\mathbf{D}_0$, i.e. $\check{\mathbf{z}}_0|_{H_1} \sim \mathcal{CN}(\mathbf{0}_{L\times 1}, \mathbf{D}_0)$. In particular, $\mathbf{D}_0 = 2\mathbf{I}_L + \mathbf{C}^H\mathbf{B}^H(\mathbf{t}\mathbf{t}^H \otimes \mathbf{M}_t)\mathbf{B}\mathbf{C}$, where $\mathbf{M}_t$ is the target amplitudes covariance matrix. We rewrite the test statistic as $T_{Pol-AR-MF} = \mathbf{h}^H\mathbf{D}_0\mathbf{h}$, where $\mathbf{h} = \left(\mathbf{D}_0^{-1/2}\right)^H \check{\mathbf{z}}_0$ is the whitened version of $\check{\mathbf{z}}_0$, i.e. $\mathbf{h} \sim \mathcal{CN}(\mathbf{0}_{L\times 1}, \mathbf{I}_L)$ so that the results in [4] can be directly applied. Let $\gamma_0 \ldots \gamma_{R-1}$ denote the $R \leq L$ distinct non-zero eigenvalues of $\mathbf{D}_0$, each with multiplicity μ_r, $r = 0, \ldots, R-1$.

Without loss of generality, we assume that no eigenvalue of matrix $\mathbf{D}_0$ is equal to zero. To see why this is the case, let us consider the eigenvalues decomposition of matrix $\mathbf{D}_0$, i.e. $\mathbf{D}_0 = \mathbf{K}\boldsymbol{\Lambda}\mathbf{K}^H$ and let us assume that $\boldsymbol{\Lambda}$ is organized so that $\boldsymbol{\Lambda} = \begin{bmatrix} \overline{\overline{\boldsymbol{\Lambda}}} & \mathbf{0}_{R\times(L-R)} \\ \mathbf{0}_{(L-R)\times R} & \mathbf{0}_{(L-R)\times(L-R)} \end{bmatrix}$, where $\overline{\overline{\boldsymbol{\Lambda}}}$ is a $R \times R$ block with the non-zero eigenvalues on its main diagonal. Therefore, the test statistic could be simply reworked as $T_{Pol-AR-MF} = \overline{\overline{\mathbf{h}}}^H\overline{\overline{\boldsymbol{\Lambda}}}\,\overline{\overline{\mathbf{h}}}$, where $\overline{\overline{\mathbf{h}}} = \boldsymbol{\Theta}^H(\mathbf{K}^H\mathbf{h})$, $\boldsymbol{\Theta} = \left[\mathbf{I}_R \;\vdots\; \mathbf{0}_{L\times(L-R)}\right]^H$.

The CDF of $T_{Pol-AR-MF}$ can be written as

$$F_0(t) = \frac{1}{2\pi}\int_{-\infty}^{\infty} \frac{e^{t(j\omega+\beta)}}{|\mathbf{I}_L + (j\omega+\beta)\boldsymbol{\Lambda}|\,(j\omega+\beta)} d\omega \;, \text{for } \beta > 0 \tag{D.1}$$

To evaluate this integral, we first resort to a partial fraction expansion for the fraction that appears in (D.1) obtaining [4]

$$\frac{1}{|\mathbf{I}_L + (j\omega+\beta)\boldsymbol{\Lambda}|\,(j\omega+\beta)} = \sum_{r=0}^{R-1}\sum_{k=0}^{\mu_r-1} \frac{\delta_{k,r}}{\left(\frac{1}{\gamma_r} + (j\omega+\beta)\right)^{k+1}} + \frac{1}{(j\omega+\beta)} \tag{D.2}$$

where the coefficients $\delta_{k,r}$ are given by

$$\delta_{k,r} = \frac{\prod_{j=0}^{R-1} \gamma_j^{-\mu_j}}{\Gamma(\mu_r - k)} \; y_r^{(\mu_r - k - 1)}(s)\Big|_{s=-\frac{1}{\gamma_r}} \qquad (r = 0, \ldots, R-1, \quad k = 0, \ldots, \mu_r - 1) \tag{D.3}$$

with $y_r^{(\mu_r-k-1)}(s)$ is the $(\mu_r - k - 1)$-th derivative of $y_r(s)$, defined as

$$y_r(s) = \prod_{\substack{j=0 \\ j \neq r}}^{R} (\zeta_j + s)^{-\mu_j} \tag{D.4}$$

with $\zeta_r = \frac{1}{\gamma_r}$, $r = 0, \ldots, R-1$, $\zeta_R = 0$ and $\mu_R = 1$.

One can evaluate the coefficient $y_r^{(\mu_r-k-1)}$ in $\delta_{k,r}$ differentiating the logarithm of $y_r(s)$, i.e. $\frac{d}{ds}\log[y_r(s)] = \frac{1}{y_r(s)} y_r^{(1)}(s)$, that yields

$$y_r^{(1)}(s) = -y_r(s) \sum_{\substack{j=0 \\ j \neq r}}^{R} \mu_j (\zeta_j + s)^{-1} \tag{D.5}$$

Subsequently, Leibniz's rule for differentiation of products may be applied. Thus, the required coefficients are obtained using the following recursion formula

$$\begin{aligned} y_r^{(p)}(s)\Big|_{s=-\zeta_r} &= \frac{d^{p-1}}{ds^{p-1}} y_r^{(1)}(s)\Big|_{s=-\zeta_n} \\ &= \sum_{u=0}^{p-1} \sum_{\substack{j=0 \\ j \neq r}}^{r} \mu_j \binom{p-1}{u} \frac{(-1)^{p-u}\Gamma(p-u)}{(\zeta_j - \zeta_r)^{p-u}} y_r^{(u)}(s)\Big|_{s=-\zeta_r}, \text{for } p \geq 1 \\ y_r^{(0)}(s)\Big|_{s=-\zeta_r} &= y_r(-\zeta_r) = \prod_{\substack{j=0 \\ j \neq r}}^{R} (\zeta_j - \zeta_r)^{-\mu_j} \end{aligned} \tag{D.6}$$

By substituting the results in (D.4) into (D.3), the coefficients $\delta_{k,n}$ are obtained and can be used to evaluate the partial fraction expansion in (D.2). Finally, this result can be employed in (D.1) to solve the integral and to obtain, after some calculations

$$F_0(t) = 1 + \sum_{r=0}^{R-1} \sum_{k=0}^{\mu_r - 1} \frac{e^{\left(-\frac{t}{\gamma_r}\right)} t^k}{\Gamma(k+1)} \delta_{k,r} \qquad (t \geq 0) \tag{D.7}$$

From the CDF in (D.7), the derivation of the P_d expression in (3.32) is straightforward

$$P_d = 1 - F_0(\eta) = \sum_{r=0}^{R-1} \sum_{k=0}^{\mu_r - 1} \frac{-e^{\left(-\frac{\eta}{\gamma_r}\right)} \eta^k}{\Gamma(k+1)} \delta_{k,r} \tag{D.8}$$

In the special case of only one eigenvalue ($R = 1$) equal to λ_0 with multiplicity $\mu_0 = L$, the residues in (D.3) can be simplified as

$$\delta_{k,0} = -\gamma_0^{-k} \tag{D.9}$$

from which the P_d in (3.33) is obtained.

In the dual special case when no eigenvalue is repeated, namely when $R = L$ and $\mu_r = 1$, $r = 0, \ldots, R - 1$ the residues in (D.3) can be simplified as

$$\delta_{0,r} = -\gamma_r \prod_{\substack{j=0 \\ j \neq r}}^{L-1} (\gamma_r - \gamma_j)^{-1} \tag{D.10}$$

Using (D.10), we easily obtain the P_d expression in (3.35).

Appendix E
Approximation of the asymptotic Pol-AR-AMF Pd for non-fluctuating target

In this Appendix, we look for $\mathrm{Prob}\{\|\check{\mathbf{z}}_0\|^2 > \eta\}$, where vector $\check{\mathbf{z}}_0$ is a complex Gaussian random variable with mean vector $\boldsymbol{\varsigma}$ and covariance matrix $\mathbf{D}_0$. To this end, we follow the main steps of the procedure reported in [4], with reference to the problem under consideration.

For the results in [50] to be applied, we first write vector $\check{\mathbf{z}}_0$ as $\check{\mathbf{z}}_0 = \boldsymbol{\varsigma} + \boldsymbol{\upsilon}$, where $\boldsymbol{\varsigma} \sim \mathcal{CN}(\mathbf{0}_{L\times 1}, \mathbf{D}_0)$. Then we rewrite the test statistic as $T_{Pol-AR-MF} = (\boldsymbol{\varsigma}_w + \boldsymbol{\upsilon}_w)^H \mathbf{D}_0 (\boldsymbol{\varsigma}_w + \boldsymbol{\upsilon}_w)$, denoting $\boldsymbol{\varsigma}_w = \left(\mathbf{D}_0^{-1/2}\right)^H \boldsymbol{\varsigma}$ as a white complex Gaussian random vector, i.e. $\boldsymbol{\varsigma}_w \sim \mathcal{CN}(\mathbf{0}_{L\times 1}, \mathbf{I}_L)$ and $\boldsymbol{\upsilon}_w = \left(\mathbf{D}_0^{-1/2}\right)^H \boldsymbol{\upsilon}$.

Moreover, let us consider the eigenvalue decomposition of matrix $\mathbf{D}_0$, i.e. $\mathbf{D}_0 = \mathbf{K}\boldsymbol{\Lambda}\mathbf{K}^H$ and let $\gamma_0 \ldots, \gamma_{L-1}$ denote the eigenvalues of $\mathbf{D}_0$. According to this model, we look for the CDF of $T_{Pol-AR-MF}$ which can be written as follows

$$F_0'(t) = \frac{1}{2\pi}\int_{-\infty}^{\infty} \frac{e^{t(j\omega+\beta)}}{(j\omega+\beta)} \frac{e^{-c(\omega)}}{|\mathbf{I}_L + (j\omega+\beta)\boldsymbol{\Lambda}|} d\omega\,, \quad \text{for } \beta > 0 \tag{E.1}$$

with $c(\omega) = \bar{\bar{\boldsymbol{\upsilon}}}^H \left(\mathbf{I}_L + \frac{1}{j\omega+\beta}\boldsymbol{\Lambda}^{-1}\right)^{-1} \bar{\bar{\boldsymbol{\upsilon}}}$, $\bar{\bar{\boldsymbol{\upsilon}}} = \mathbf{K}^H \boldsymbol{\upsilon}_w$.

A closed form solution for the integral in (E.1) cannot be obtained in the general case. Therefore, as in [4], we derive an approximation of the sought P_d expression by resorting to the SP technique [10].

To this end, we define

$$\begin{aligned} f(\omega) = t(j\omega+\beta) - \ln(j\omega+\beta) + \sum_{l=0}^{L-1} |\bar{\bar{v}}_l|^2 \left[\frac{1}{1+(j\omega+\beta)\gamma_l} - 1\right] \\ - \sum_{l=0}^{L-1} \ln[1+(j\omega+\beta)\gamma_l] \end{aligned} \tag{E.2}$$

and, consequently, we write (E.1) as

$$F_0'(t) = \frac{1}{2\pi}\int_{-\infty}^{\infty} e^{f(\omega)}\, d\omega \tag{E.3}$$

To apply the SP technique, we first differentiate $f(\omega)$ and look for the only real solution of $\dot{f}(\omega) = 0$, denoted as $\omega_0 = j(\beta + p_0)$, in the region $p \in (-\infty, 0)$.

$$\dot{f}(\omega) = -\sum_{l=0}^{L-1} \frac{j\gamma_l}{1 + (j\omega + \beta)\gamma_l}\left[1 + \frac{|\bar{v}_l|^2}{1 + (j\omega + \beta)\gamma_l}\right] + jt - \frac{\mathrm{j}}{(j\omega + \beta)} = 0 \tag{E.4}$$

Now we approximate $f(\omega)$ using a second order Taylor expansion around ω_0, yielding

$$F_0'(t) \approx \frac{e^{f(\omega_0)}}{\sqrt{2\pi\left|\ddot{f}(\omega_0)\right|}} \tag{E.5}$$

Therefore, by evaluating (E.2) in ω_0 and $\ddot{f}(\omega_0)$ we obtain

$$\begin{aligned} P_d \approx 1 - \frac{1}{\sqrt{2\pi}}\Bigg| & -\sum_{l=0}^{L-1}\left\{\frac{2|\bar{v}_l|^2\gamma_l{}^2}{[1 + (j\omega_0 + \beta)\gamma_l]^3} + \frac{\gamma_l{}^2}{[1 + (j\omega_0 + \beta)\gamma_l]^2}\right\} \\ & - \frac{1}{(j\omega_0 + \beta)^2}\Bigg|^{-\frac{1}{2}} \exp\Bigg\{\eta(j\omega_0 + \beta) - \ln(j\omega_0 + \beta) \\ & + \sum_{l=0}^{L-1}|\bar{v}_l|^2\left[\frac{1}{1 + (j\omega_0 + \beta)\gamma_l} - 1\right] - \sum_{l=0}^{L-1}\ln[1 + (j\omega_0 + \beta)\gamma_l]\Bigg\} \end{aligned} \tag{E.6}$$

which can be easily converted in (4.8).

Bibliography

[1] Abramovich Y. I. and Johnson B. A., "Threshold performance for conditional and unconditional direction of arrival estimation," *2012 Conference Record of the Forty Sixth Asilomar Conference on Signals, Systems and Computers (ASILOMAR)*, Pacific Grove, CA, 2012, pp. 5-12

[2] Alfano G., De Maio A. and Conte E., "Polarization diversity detection of distributed targets in compound-Gaussian clutter," in *IEEE Transactions on Aerospace and Electronic Systems*, vol. 40, no. 2, pp. 755-765, April 2004.

[3] Alfano G., De Maio A. and Farina A., "Model-based adaptive detection of range-spread targets," in *IEE Proceedings - Radar, Sonar and Navigation*, vol. 151, no. 1, pp. 2-10, 14 Feb. 2004.

[4] Al-Naffouri T. Y. , Moinuddin M., Ajeeb N., Hassibi B. and Moustakas A. L., "On the Distribution of Indefinite Quadratic Forms in Gaussian Random Variables," in *IEEE Transactions on Communications*, vol. 64, no. 1, pp. 153-165, Jan. 2016.

[5] Ariza A. P. G. and Thomä R. S., "Polarimetric ultrawideband MIMO radar for security check points: Detecting and classifying suspects carrying wires," *2012 6th European Conference on Antennas and Propagation (EUCAP)*, Prague, 2012, pp. 1733-1736.

[6] Athley F., "Threshold region performance of maximum likelihood direction of arrival estimators," in *IEEE Transactions on Signal Processing*, vol. 53, no. 4, pp. 1359-1373, Apr. 2005

[7] Baker C. J., Griffiths H. D. and I. Papoutsis, "Passive coherent location radar systems. Part 2: waveform properties," in *IEE Proceedings - Radar, Sonar and Navigation*, vol. 152, no. 3, pp. 160-168, 3 June 2005.

[8] Barankin E. W., "Locally best unbiased estimates," The Annals of Mathematical Statistics, vol. 20, pp. 477–501, 1949

[9] Belfiori F., Monni S., Van Rossum W., et al.: 'Antenna array characterisation and signal processing for an FM radio-based passive coherent location radar system', *IET Radar, Sonar & Navigation*, 2012, 6 (8), pp.687-696.

[10] Bender C. M. and Orszag S. A., Advanced Mathematical Methods for Scientists and Engineers, New York, NY, USA, McGraw-Hill, 1978

[11] Blachman N. M., "Position Determination from Radio Bearings," in *IEEE Transactions on Aerospace and Electronic Systems*, vol. AES-5, pp. 558-560, 1969

[12] Boerner W. and Yamaguchi Y., "A state-of-the-art review in radar polarimetry and its applications in remote sensing," in *IEEE Aerospace and Electronic Systems Magazine*, vol. 5, no. 6, pp. 3-6, June 1990.

[13] BouDaher E., Jia Y., Ahmad F. and Amin M. G., "Multi-Frequency Co-Prime Arrays for High-Resolution Direction-of-Arrival Estimation," in *IEEE Transactions on Signal Processing*, vol. 63, no. 14, pp. 3797-3808, July 2015

[14] Bowyer D. E., Rajasekaran P. K. and Gebhart W. W., "Adaptive Clutter Filtering Using Autogressive Spectral Estimation," in *IEEE Transactions on Aerospace and Electronic Systems*, vol. AES-15, no. 4, pp. 538-546, July 1979.

[15] Box G. and Jenkins G., Time Series Analysis: Time Series Analysis, Forecasting and Control, Holden-Day Inc, 1970.

[16] Colone F. and Lombardo P., "Exploiting polarimetric diversity in FM-based PCL", *Proc. IEEE International Radar Conference 2014*, Lille, France, October 2014, pp. 1-6.

[17] Colone F. and Lombardo P., "Non-coherent adaptive detection in passive radar exploiting polarimetric and frequency diversity," in *IET Radar, Sonar & Navigation*, vol. 10, no. 1, pp. 15-23, 1 2016.

[18] Colone F. and Lombardo P., "Polarimetric passive coherent location," in *IEEE Transactions on Aerospace and Electronic Systems*, vol. 51, no. 2, pp. 1079-1097, April 2015.

[19] Colone F., Bongioanni C. and Lombardo P., "Multifrequency integration in FM radio-based passive bistatic radar. Part I: Target detection", *IEEE Aerospace and Electronic Systems Magazine*, 2013, 28 (4), pp. 28-39.

[20] Colone F., Bongioanni C. and Lombardo P., "Multifrequency integration in FM radio-based passive bistatic radar. Part II: Direction of arrival estimation", *IEEE Aerospace and Electronic Systems Magazine*, 2013, 28 (4), pp. 40-47.

[21] Colone F., Langellotti, D. and Lombardo, P., "DVB-T signal ambiguity function control for passive radars", *IEEE Transactions on Aerospace and Electronic Systems*, 2014, 50, (1), pp. 329-347.

[22] Colone F., O'Hagan D.W., Lombardo P. and Baker C.J., "A multistage processing algorithm for disturbance removal and target detection in passive bistatic radar", *IEEE Transactions on Aerospace and Electronic Systems*, 45 (2), Apr. 2009.

[23] Colone, F., Palmarini, C., Martelli, T., et al., "Sliding extensive cancellation algorithm for disturbance removal in passive radar", *IEEE Transactions on Aerospace and Electronic Systems*, 2016, 52, (3), pp. 1309-1326

[24] Conti M., Moscardini C. and Capria A., "Dual-polarization DVB-T passive radar: Experimental results," *2016 IEEE Radar Conference (RadarConf)*, Philadelphia, PA, 2016, pp. 1-5.

[25] Coutts S. D., "Passive localization of moving emitters using out-of-plane multipath," in *IEEE Transactions on Aerospace and Electronic Systems*, vol. 36, no. 2, pp. 584-595, April 2000.

[26] De Maio A. and Ricci G., "A polarimetric adaptive matched filter", *Signal Processing*, vol. 81, no. 12, pp. 2583-2589, Dec. 2001.

[27] De Maio A., Farina A. and Foglia G., "Target fluctuation models and their application to radar performance prediction," in *IEE Proceedings - Radar, Sonar and Navigation*, vol. 151, no. 5, pp. 261-269, 10 Oct. 2004.

[28] Del-Rey-Maestre N., Jarabo-Amores M.P., Mata-Moya D., et al., "Statistical analysis of UHF bistatic radar clutter in coastal scenarios', *2015 European Radar Conference (EuRAD)*, Paris, 2015, pp. 253-256.

[29] Del-Rey-Maestre N., Mata-Moya D., Jarabo-Amores M.P., et al., "MLP-based approximation to the Neyman Pearson detector in a terrestrial passive bistatic radar scenario', *IEEE EUROCON 2015 - International Conference on Computer as a Tool (EUROCON)*, Salamanca, 2015, pp. 1-6

[30] Drosopoulos A., "Description of the OHGR database., "Defence Research Establishment, Ottawa, Tech. Rep. 94-14, Dec. 1994.

[31] Farina A., Gini F., Greco M. V. and Verrazzani L., "High resolution sea clutter data: statistical analysis of recorded live data," in *IEE Proceedings - Radar, Sonar and Navigation*, vol. 144, no. 3, pp. 121-130, June 1997.

[32] Gao Y., Li H. and Himed B., "Adaptive Subspace Tests for Multichannel Signal Detection in Auto-Regressive Disturbance," in *IEEE Transactions on Signal Processing*, vol. 66, no. 21, pp. 5577-5587, 1 Nov.1, 2018.

[33] Gershman A. B., Stoica P., Pesavento M. and Larsson E. G., "Stochastic Cramer-Rao bound for direction estimation in unknown noise fields," in *IEE Proceedings - Radar, Sonar and Navigation*, vol. 149, no. 1, pp. 2-8, Feb 2002.

[34] Gini F., Greco M., Diani M. and Verrazzani L., "Performance analysis of two adaptive radar detectors against non-Gaussian real sea clutter data," in *IEEE Transactions on Aerospace and Electronic Systems*, vol. 36, no. 4, pp. 1429-1439, Oct. 2000.

[35] Giuli D., "Polarization diversity in radars," in *Proceedings of the IEEE*, vol. 74, no. 2, pp. 245-269, Feb. 1986.

[36] Goddard J. W. F. and Cherry S. M., "The ability of dual-polarization radar (copolar linear) to predict rainfall rate and microwave attenuation," in *Radio Science*, vol. 19, no. 01, pp. 201-208, Jan.-Feb. 1984.

[37] Gogineni S. and Nehorai A., "Polarimetric MIMO Radar With Distributed Antennas for Target Detection," in *IEEE Transactions on Signal Processing*, vol. 58, no. 3, pp. 1689-1697, March 2010.

[38] Greco M., Bordoni F. and Gini F., "X-band sea-clutter nonstationarity: influence of long waves," in *IEEE Journal of Oceanic Engineering*, vol. 29, no. 2, pp. 269-283, April 2004.

[39] Greco M., Gini F. and Rangaswamy M., "Statistical analysis of measured polarimetric clutter data at different range resolutions," in *IEE Proceedings - Radar, Sonar and Navigation*, vol. 153, no. 6, pp. 473-481, December 2006.

[40] Griffiths H. D. and Baker C. J., "Passive coherent location radar systems. Part 1: performance prediction," in *IEE Proceedings - Radar, Sonar and Navigation*, vol. 152, no. 3, pp. 153-159, 3 June 2005.

[41] Griffiths H. D. and Baker C. J., Introduction to Passive Radar, Norwood, MA, USA: Artech, Mar. 2017.

[42] Griffiths H. D. and Long N.R., "Television-based bistatic radar," in *IEE Proceedings F - Communications, Radar and Signal Processing*, vol. 133, no. 7, pp. 649-657, 1986.

[43] Griffiths H. D., "Passive and bistatic radar", in Melvin W.L., Scheer J.A. (eds.) *Principles of Modern Radar : Radar Applications* (SciTech Publishing, Inc., 2014).

[44] Hao C., Gazor S., Orlando D., Foglia G. and Yang J., "Parametric space–time detection and range estimation of a small target," in *IET Radar, Sonar & Navigation*, vol. 9, no. 2, pp. 221-231, 2 2015.

[45] Harville D. A., Matrix Algebra From a Statistician's Perspective, New York, NY, USA, Springer, 1997.

[46] Haykin S. and Steinhardt A., Adaptive radar detection and estimation, New York : Wiley, 1992.

[47] Haykin S., C. Krasnor, Nohara T. J., Currie B. W. and Hamburger D., "A coherent dual-polarized radar for studying the ocean environment," in *IEEE Transactions on Geoscience and Remote Sensing*, vol. 29, no. 1, pp. 189-191, Jan. 1991.

[48] Haykin S., Currie B. W. and Kesler S. B., "Maximum-entropy spectral analysis of radar clutter," in *Proceedings of the IEEE*, vol. 70, no. 9, pp. 953-962, Sept. 1982.

[49] Heckenbach J., Kuschel H., Schell J., et al., "Passive radar based control of wind turbin collision warning for air traffic PARASOL', *Proceedings of International Radar Symposium 2015*, Dresden, Germany, June 2015, pp. 36-41.

[50] Howland P. E., "Target tracking using television-based bistatic radar," in *IEE Proceedings - Radar, Sonar and Navigation,* vol. 146, no. 3, pp. 166-174, June 1999.

[51] Howland P. E., Maksimiuk D. and Reitsma G., "FM radio based bistatic radar," in *IEE Proceedings - Radar, Sonar and Navigation*, vol. 152, no. 3, pp. 107-115, 3 June 2005.

[52] Hung H. and Kaveh M., "On the statistical sufficiency of the coherently averaged covariance matrix for the estimation of the parameters of wideband sources," *ICASSP '87. IEEE International Conference on Acoustics, Speech, and Signal Processing*, 1987, pp. 33-36.

[53] Hurtado M. and Nehorai A., "Polarimetric Detection of Targets in Heavy Inhomogeneous Clutter," in *IEEE Transactions on Signal Processing*, vol. 56, no. 4, pp. 1349-1361, April 2008.

[54] Hytti H., Takalo R., and Ihalainen H., "Tutorial on multivariate autoregressive modelling," Journal of clinical monitoring and computing, 20(2):101–108, 2006.

[55] Islam, T., Rico-Ramirez M.A. , Han D. , and Srivastava P.K. , "Artificial intelligence techniques for clutter identification with polarimetric radar signatures". *Atmospheric Research*, vol. 109–110, pp. 95–113 2012.

[56] Jian Li, Liu G., Jiang N. and Stoica P., "Moving target feature extraction for airborne high-range resolution phased-array radar," in *IEEE Transactions on Signal Processing*, vol. 49, no. 2, pp. 277-289, Feb. 2001.

[57] Kay S. M. and Nagesha V., "Maximum likelihood estimation of signals in autoregressive noise," in *IEEE Transactions on Signal Processing*, vol. 42, no. 1, pp. 88-101, Jan. 1994.

[58] Kay S. M., Fundamentals of Statistical Signal Processing: Detection Theory, vol. II. Englewood Cliffs, NJ, USA: Prentice-Hall, 1993.

[59] Kay S. M., Modern Spectral Estimation, Theory and Application. Englewood Cliffs, NJ: Prentice Hall, 1988.

[60] Kelly E.J., "An adaptive detection algorithm', *IEEE Transactions on Aerospace and Electronic Systems*, 1986, 22 (1), pp. 115-127.

[61] Kim B. K., Kang H.and Park S., "Experimental Analysis of Small Drone Polarimetry Based on Micro-Doppler Signature," in *IEEE Geoscience and Remote Sensing Letters*, vol. 14, no. 10, pp. 1670-1674, Oct. 2017.

[62] Klemm R., Applications of space-time adaptive processing, The Institu-tion of Electrical Engineers, 2004.

[63] Krasnov O. A. and Yarovoy A. G., "Polarimetric micro-Doppler characterization of wind turbines," *2016 10th European Conference on Antennas and Propagation (EuCAP)*, Davos, 2016, pp. 1-5.

[64] Krim H. and Viberg M., "Two decades of array signal processing research: the parametric approach," in *IEEE Signal Processing Magazine*, vol. 13, no. 4, pp. 67-94, July 1996.

[65] Liu H., Zhou S., Su H. and Yu Y., "Detection performance of spatial-frequency diversity MIMO radar," in *IEEE Transactions on Aerospace and Electronic Systems*, vol. 50, no. 4, pp. 3137-3155, October 2014.

[66] Lombardo P. and Colone F., " Advanced processing methods for passive bistatic radar', in Melvin, W. L., and Scheer, J. A. (Eds.): 'Principles of Modern Radar: Advanced Radar Techniques', Raleigh, NC: SciTech Publishing, 2012, pp. 739–821.

[67] Lombardo P., Pastina D. and Bucciarelli T., "Adaptive polarimetric target detection with coherent radar. II. Detection against non-Gaussian background," in *IEEE Transactions on Aerospace and Electronic Systems*, vol. 37, no. 4, pp. 1207-1220, Oct. 2001.

[68] Martelli T., Colone F., Tilli E. and Di Lallo A., "Multi-Frequency Target Detection Techniques for DVB-T Based Passive Radar Sensors", *Sensors*, vol. 16, pp. 1594, 2016.

[69] Martelli, T., Cardinali, R., Colone, F., "Detection performance assessment of the FM-based AULOS® Passive Radar for air surveillance applications", *19th International Radar Symposium (IRS)*, Bonn, June 2018, pp. 1-10.

[70] Martelli, T., Colone, F. and Cardinali, R., "DVB-T based Passive Radar for simultaneous counter drone operations and civil air traffic surveillance", *IET Radar, Sonar & Navigation*, in print.

[71] Martorella M., Palmer J., Berizzi F., Haywood B. and Bates B., "Polarimetric ISAR autofocusing," in *IET Signal Processing*, vol. 2, no. 3, pp. 312-324, September 2008.

[72] Marzano F. S., Botta G. and Montopoli M., "Iterative Bayesian Retrieval of Hydrometeor Content From X-Band Polarimetric Weather Radar," in *IEEE Transactions on Geoscience and Remote Sensing*, vol. 48, no. 8, pp. 3059-3074, Aug. 2010.

[73] Metford P., Haykin S. and Taylor D., "An innovations approach to discrete-time detection theory (Corresp.)," in *IEEE Transactions on Information Theory*, vol. 28, no. 2, pp. 376-380, March 1982.

[74] Michels J. H., Varshney P. and Weiner D., "Multichannel signal detection involving temporal and cross-channel correlation," in *IEEE Transactions on Aerospace and Electronic Systems*, vol. 31, no. 3, pp. 866-880, July 1995.

[75] Novak L. M. and Burl M. C., "Optimal speckle reduction in polarimetric SAR imagery," in *IEEE Transactions on Aerospace and Electronic Systems*, vol. 26, no. 2, pp. 293-305, March 1990.

[76] Novak L. M., Sechtin M. B. and Cardullo M. J., "Studies of target detection algorithms that use polarimetric radar data," in *IEEE Transactions on Aerospace and Electronic Systems*, vol. 25, no. 2, pp. 150-165, March 1989.

[77] Olsen K.E. and Woodbridge, K., "FM based passive bistatic radar target range improvement", *Proceedings of 2009 International Radar Sysmposium*, Hamburg, Germany, September 2009.

[78] Olsen K.E., Woodbridge K. and Andersen I.A., "FM based passive bistatic radar target range improvement: Part II", *Proceedings of 2010 International Radar Sysmposium*, Vilnius, Lithuania, June 2010.

[79] Ottersten B., Viberg M., Stoica P. and Nehorai A., "Exact and large sample maximum likelihood techniques for parameter estimation and detection in array processing," in *Radar Array Processing*, Haykin S., J. Litva, and T. J. Shepherd, Eds. Berlin, Germany: Springer-Verlag, 1993, ch. 4, pp. 99–151.

[80] Pallotta L. and Orlando D., "Polarimetric Covariance Eigenvalues Classification in SAR Images," in *IEEE Geoscience and Remote Sensing Letters*, vol. 16, no. 5, pp. 746-750, May 2019.

[81] Palmer J., Harms H., Searle S., et al., "DVB-T passive radar signal processing', *IEEE Transactions on Signal Processing*, 2013, 61 (8), pp. 2116-2126.

[82] Park H. R., Li J. and Wang H., "Polarization-space-time domain generalized likelihood ratio detection of radar targets", *Signal Processing*, vol. 41, pp. 153-164, 1995.

[83] Pastina D., Lombardo P. and Bucciarelli T., "Adaptive polarimetric target detection with coherent radar. I. Detection against Gaussian background," in *IEEE Transactions on Aerospace and Electronic Systems*, vol. 37, no. 4, pp. 1194-1206, Oct. 2001.

[84] Pastina D., Lombardo P., Farina A. and Daddi P., "Super-resolution of polarimetric SAR images of ship targets", *Signal Processing*, vol. 83, no. 8, pp. 1737-1748, 2003.

[85] Pasupathy S. and Alford W. J., "Range and Bearing Estimation in Passive Sonar," in *IEEE Transactions on Aerospace and Electronic Systems*, vol. AES-16, no. 2, pp. 244-249, March 1980.

[86] Pinsky M., Figueras i Ventura J., Otto T., Sterkin A., Khain A. and Russchenberg H. W. J., "Application of a Simple Adaptive Estimator for an Atmospheric Doppler Radar," in *IEEE Transactions on Geoscience and Remote Sensing*, vol. 49, no. 1, pp. 115-127, Jan. 2011.

[87] Proakis J. G., Digital Communications, 4th Edition, McGraw-Hill, New York, 2001.

[88] Richmond C. D., "Mean-squared error and threshold SNR prediction of maximum-likelihood signal parameter estimation with estimated colored noise covariances," in *IEEE Transactions on Information Theory*, vol. 52, no. 5, pp. 2146–2164, May 2006.

[89] Rife D. C. and Boorstyn R. R., "Single-tone parameter estimation from discrete-time observations," in *IEEE Transactions on Information Theory*, vol. 20, no. 5, pp. 591-598, Sep 1974.

[90] Roman J. R., Rangaswamy M., Davis D. W., Zhang Q., Himed B. and Michels J. H., "Parametric adaptive matched filter for airborne radar applications," in *IEEE Transactions on Aerospace and Electronic Systems*, vol. 36, no. 2, pp. 677-692, April 2000.

[91] Roy R. and Kailath T., "ESPRIT-estimation of signal parameters via rotational invariance techniques," in *IEEE Transactions on Acoustics, Speech and Signal Processing*, vol. 37, no. 7, pp. 984–995, Jul. 1989.

[92] Rytel-Andrianik R. et al., "Simple X-band polarimetric micro-Doppler analyses of ground moving targets," *2015 Signal Processing Symposium (SPSympo)*, Debe, 2015, pp. 1-4.

[93] Schmidt R. O., "Multiple emitter location and signal parameter estimation," in *IEEE Transactions on Antennas and Propagation*, vol. AP-34, no. 3, pp. 276–280, Mar. 1986.

[94] Schwark C. and Cristallini D., "Advanced multipath clutter cancellation in OFDM-based passive radar systems', *2016 IEEE Radar Conference (RadarConf16)*, Philadelphia, PA, USA, May 2016, pp. 1-5.

[95] Searle S., Howard,S. and Palmer,J., "Remodulation of DVB-T signals for use in passive bistatic radar', *Proceedings of 44th Asilomar Conference on Signals, Systems and Computers,* Pacific Grove, CA, USA, Nov. 2010, pp. 1112-1116.

[96] Searle S., Palmer J., Davis L., et al., "Evaluation of the ambiguity function for passive radar with OFDM transmissions', *2014 IEEE Radar Conference (RadarConf14),* Cincinnati, OH, USA, May 2014, pp. 1040-1045.

[97] Sheikhi A., Nayebi M. M. and Aref M. R., "Adaptive detection algorithm for radar signals in autoregressive interference," in *IEE Proceedings - Radar, Sonar and Navigation*, vol. 145, no. 5, pp. 309-314, Oct. 1998.

[98] Shuai X., Kong L. and Yang J., "AR-model-based adaptive detection of range-spread targets in compound Gaussian clutter", *Signal Processing*, vol. 91, pp. 750-758, Aug. 2011.

[99] Shynk J. J., Probability Random Variables and Random Processes: Theory and Signal Processing Applications, New York, NY, USA:Wiley, 2012.

[100] Simon M. K. and Alouini M.-S., "On the difference of two chi-square variates with application to outage probability computation," in *IEEE Transaction on Communications*, vol. 49, no.11, pp. 1946-1954, Nov. 2001

[101] Skolnik M. I., "Resolution of angular ambiguities in radar array antennas with widely-spaced elements and grating lobes," in *IRE Transactions on Antennas and Propagation*, vol. AP-10, pp. 351-352, May 1962.

[102] Sohn K. J., Li H. and Himed B., "Parametric GLRT for Multichannel Adaptive Signal Detection," in *IEEE Transactions on Signal Processing*, vol. 55, no. 11, pp. 5351-5360, Nov. 2007.

[103] Son I. and Yazici B., "Passive polarimetrie multistatic radar for ground moving target," *2016 IEEE Radar Conference (RadarConf),* Philadelphia, PA, 2016, pp. 1-6.

[104] Special Issue on Passive Radar Systems (Guest Editor: Howland P. E.), *IEE Proceedings on Radar, Sonar and Navigation*, 2005, 153 (3), pp. 105-223.

[105] Special Issue on Passive Radar, Part I & II (Guest Editors: Farina A., Kuschel H.), *IEEE Aerospace and Electronic Systems Magazine*, 2012, 27 (10-11).

[106] Stansfield R. G., "Statistical Theory of D.F. Fixing", *Journal of the Institution of Electrical Engineers - Part III-A: Radiocommunication*, vol. 94, pp. 762-770, 1947.

[107] Stoica P. and Nehorai A., "MUSIC, maximum likelihood, and Cramer-Rao bound," in *IEEE Transactions on Acoustics, Speech and Signal Processing*, vol. 37, pp. 720-741, May 1989.

[108] Stoica P. and Nehorai A., "Performance study of conditional and unconditional direction-of-arrival estimation," in *IEEE Transactions on Acoustics, Speech, and Signal Processing*, vol. 38, no. 10, pp. 1783-1795, Oct 1990.

[109] Swerling P., "Probability of detection for fluctuating targets," in *IRE Transactions on Information Theory*, vol. 6, no. 2, pp. 269-308, April 1960.

[110] Swindlehurst A. L. and Stoica P., "Maximum likelihood methods in radar array signal processing," in *Proceedings of the IEEE*, vol. 86, no. 2, pp. 421-441, Feb. 1998.

[111] Tahmoush D. and Silvious J., "Radar Measurement of Human Polarimetric Micro-Doppler", *Hindawi Journal of Electrical and Computer Engineering*, vol. 2013.

[112] Thomas P. and Haykin S., "Stochastic modelling of radar returns," in *IEE Proceedings F - Communications, Radar and Signal Processing*, vol. 133, no. 5, pp. 476-481, August 1986.

[113] Torrieri D. J., "Statistical Theory of Passive Location Systems," in *IEEE Transactions on Aerospace and Electronic Systems,* vol. AES-20, no. 2, pp. 183-198, March 1984.

[114] Ulrich M. and Yang B., "Multi-carrier MIMO radar: A concept of sparse array for improved DOA estimation," *2016 IEEE Radar Conference (RadarConf16),* Philadelphia, PA, 2016, pp. 1-5.

[115] Van Trees H. L. and Bell K.L. , Bayesian Bounds for Parameter Estimation and Nonlinear Filtering/Tracking, Wiley, New York (2007).

[116] Van Trees H. L., Detection, Estimation and Modulation Theory, Part I, Detection, Estimation, and Linear Modulation Theory, New York, NY, USA, Wiley, 1968.

[117] Van Trees H. L., Detection, Estimation and Modulation Theory, Part IV, Optimum Array Processing, New York, NY, USA, Wiley, 2002.

[118] Villano M., Colone F. and Lombardo P., "Antenna Array for Passive Radar: Configuration Design and Adaptive Approaches to Disturbance Cancellation', *International Journal of Antennas and Propagation*, 2013.

[119] Wang W. Q., "Frequency Diverse Array Antenna: New Opportunities," in *IEEE Antennas and Propagation Magazine*, vol. 57, no. 2, pp. 145-152, April 2015.

[120] Willis N.J. and Griffiths H.D. (eds.) *Advances in Bistatic Radar*. (SciTech Publishing, Raileigh, NC, 2007).

[121] You J., Wan X., Fu Y. and Fang G., "Experimental study of polarisation technique on multi-FM-based passive radar," in *IET Radar, Sonar & Navigation*, vol. 9, no. 7, pp. 763-771, 8 2015.

[122] Zebker H. A. and Van Zyl J. J., "Imaging radar polarimetry: a review," in *Proceedings of the IEEE*, vol. 79, no. 11, pp. 1583-1606, Nov. 1991.

[123] Zemmari, R., Broetje, M., Battistello, G., et al., "GSM passive coherent location system: performance prediction and measurement evaluation" *IET Radar, Sonar & Navigation*, 2014, 8 (2), pp. 94-105.

[124] Ziv J. and Zakai M., "Some lower bounds on signal parameter estimation," in *IEEE Transactions on Information Theory*, vol. 15, no. 3, pp. 386-391, May 1969.